

UNIFIED MICROSCOPY AND SPECTROSCOPY FOR
NANOSCALE CHEMICAL IMAGING

by

Vyacheslav N. Romanov

MS, University of Pittsburgh, 2001

Submitted to the Graduate Faculty of
Arts and Sciences in partial fulfillment
of the requirements for the degree of
Doctor of Philosophy

University of Pittsburgh

2005

UNIVERSITY OF PITTSBURGH

ARTS AND SCIENCES

This dissertation was presented

by

Vyacheslav N. Romanov

It was defended on

July 18, 2005

and approved by

David H. Waldeck, Professor and Chair, Department of Chemistry

Shigeru Amemiya, Assistant Professor, Department of Chemistry

Jean R. Blachere, Associate Professor Emeritus, Department of Materials Science and Engineering

Dissertation Director: Gilbert C. Walker, Professor, Department of Chemistry

UNIFIED MICROSCOPY AND SPECTROSCOPY FOR NANOSCALE CHEMICAL IMAGING

Vyacheslav N. Romanov, PhD

University of Pittsburgh, 2005

Chemical imaging with nanometer scale resolution requires integration of the microscopic and spectroscopic analyses within a new conceptual framework that takes into account quantum size effects and evanescent electromagnetic fields. This work has focused on nanometer scale effects of changes in reflectance spectra of materials near resonances. Two types of resonances were considered.

A surface plasmon resonance of metallic nanometer-sized particles reflecting UV/Visible light was studied in application to silver diffusion and cluster growth in glass matrix. The resonance is a result of energy and momentum being transferred from incident photons into surface plasmons, and is sensitive to the refractive index of the host medium and the particle size. A combination of the Mie theory, with quantum size corrections and simulations of ion-exchange diffusion was utilized to interpret the findings of microscopic and spectroscopic experimental studies.

A single vibrational mode of di-iron nonacarbonyl was used as a reference in developing high resolution chemical imaging. A near field equivalent of the Lorentzian shape has been discovered, both experimentally and theoretically, to have an oscillatory pattern in the frequency domain.

TABLE OF CONTENTS

Acknowledgments.....	x
Chapter I: Introduction.....	1
Chapter II: Silver Bleed Through Effect	3
Statement of Problem	4
Purpose of Study	4
Description of Terms.....	6
Chapter III: Experimental Conditions of Silver Diffusion Study.....	7
Technological Constraints of Problem	7
Fundamental Challenges of Problem	9
Chapter IV: Numerical Models and Research Methods: Silver Bleedthrough.....	11
Selection of Theoretical Models.....	12
Selection of Instrumentation and Techniques.....	16
Collection of Data.....	18
Analysis of Data	18
Chapter V: Results and Discussion for Silver Bleed Through	20
Significance of Findings	26
Chapter VI: Review of Near Field Infrared Microscopy.....	27
Chapter VII: Characterization of di-iron nonacarbonyl vibrational dispersion	30
Molecular and Crystal Structure	30
Collection and Analysis of Infrared Spectra	32
Summary of New Findings	38
Chapter VIII: Experimental Setup for ANSIM Microscopy.....	40
CO ₂ /CO Laser Emission.....	41
Near Field Optical Setup	44
Chapter IX: Collection of Near Field Data.....	46

Chapter X: Theoretical Models and Analysis of the Near Field Data	57
Chapter XI: Summary	80
Bibliography	82
Appendix A: Chemical Diffusion.....	90
Appendix B: Reference Data	93
Appendix C: Mie Scattering	94
Appendix D: Microanalysis	101
Appendix E: Visual Basic 6.0 code	104
Appendix F: Infrared Transmittance of Di-iron Nonacarbonyl.....	105
Appendix G: Matlab 5.0 and Matlab 7.0 codes	115
Appendix H: Numerical Electromagnetic Code simulations	116

LIST OF TABLES

<i>Number</i>	<i>Page</i>
<i>Table 1. Experimental Techniques.....</i>	<i>1</i>
<i>Table 2. Color Variations with Particle Size.....</i>	<i>10</i>
<i>Table 3. The chromaticity and the reflection peak height, ΔR with silver colloid size.....</i>	<i>10</i>
<i>Table 4. Color vs. Time and Firing Temperature.....</i>	<i>10</i>
<i>Table 5. $\nu(\text{CO})$ region assignment correlation for $\text{Fe}_2(\text{CO})_9$.....</i>	<i>31</i>
<i>Table 6. Summary of Vibrational Oscillator Strengths.....</i>	<i>38</i>
<i>Table 7. Vibrational Oscillator Strengths.....</i>	<i>74</i>

LIST OF FIGURES

<i>Number</i>	<i>Page</i>
1. Discoloration Mechanism	5
2. Substrate Stick Response.....	8
3. Enamel Stick Response.....	8
4. Typical Heating Curves.....	8
5. Time-Temperature Effects.....	11
6. Electron Probe Microanalysis.....	17
7. X-ray Photoemission Spectroscopy.....	17
8. Auger Electron Spectroscopy.....	17
9. Reflectance Spectra Summary	20
10. Mie Scattering (MATLAB)	21
11. SEM image of Ag-Pd particles	23
12. SEM microprobe	24
13. Ion-Exchange Diffusion Model.....	25
14. Results of SEM Analysis.....	25
15. Infrared Diffraction.....	28
16. Mapping of Absorbing Doublet.....	29
17. Decomposition Effects.....	32
18. Dielectric function of iron carbonyl at low wavenumbers.....	34
19. CsCl blank pellet extinction	35
20. Background subtracted absorption at low concentrations.....	35
21. Total absorption at high concentrations.....	36
22. Surface reflectance of iron carbonyl (air interface).....	36
23. $\text{Fe}_2(\text{CO})_9$ in CsCl: $f_v \ll 1$ transmittance vs. $f_v=1/3$ extinction	37
24. Basis of apertureless near-field scanning infrared microscopy.....	40
25. Beam expansion of the CO_2/CO laser.....	41
26. High vacuum manifold	42
27. CO laser spectra (Edinburgh Instruments as a reference)	43
28. Spectral changes and vibro-rotational transitions	44

29. Schematic representation of the ANSIM setup	45
30. ANSIM apparatus with homodyning option.....	46
31. z-dependence of the first and second harmonic near-field signal	47
32. Typical peak and baseline near-field signals.....	48
33. z-plots above, near, and away from absorbing particles.....	49
34. Illustration of the low signal-to-noise ratio of a second harmonic.....	49
35. Near-field signal vs. displacement of the partial reflector	50
36. z-dependence of the homodyned first harmonic near-field signal	52
37. Multi-particle edge effect (the second harmonic detection)	53
38. Broadband CO laser modes beating diagram.....	54
39. Absorption, scattering and topographic artifacts.....	55
40. Multi-wavelength IR Signal spatial decay vs. focal position	55
41. Typical signal at different amplitudes.....	56
42. The origin of the second harmonic signal.....	60
43. Near field contrast of silicon film deposited on gold surface.....	60
44. Polarizability model for a coated tip.....	61
45. Near field resonance shifts depending on the oscillator strength.....	62
46. Spatial resolution of the near field image	64
47. Thin particle rotation and shift artifacts	64
48. Second harmonic ANSIM signal of $\text{Fe}_2(\text{CO})_9$ on gold surface	65
49. Simulated of $\text{Fe}_2(\text{CO})_9$ vs. gold contrast (CDM)	66
50. First harmonic auto-homodyned signal.....	67
51. Near-field phase shift (CDM)	68
52. Contrast reversal due to phase shift (enhanced image)	69
53. Broadband second harmonic auto-homodyned near-field image	70
54. Temporal changes and artifacts in broadband ANSIM image.....	71
55. Geometrical model for NEC simulations	72
56. Comparison of theoretical models and experimental results.....	73
57. NEC simulations of the angular distribution	73
58. Typical NEC2 simulated near-field spectra	76
59. Transient modes contribution to near-field response ($\epsilon_\infty=2.1$)	77

60. Cantilever deflection model	77
61. NEC2 simulated response for $\epsilon_\infty=2.0$	78
62. NEC2 simulated response for $\epsilon_\infty=2.2$	78
63. NEC2 simulated response for $\epsilon_\infty=2.1$	79
64. Static image dipole model fit of experimental data (ϵ_∞ variations)	80

ACKNOWLEDGMENTS

The author wishes to express sincere appreciation to the Research Director, Professor of Chemistry Gilbert Walker and Dr. Joseph Ryan for their valuable advising and the University of Pittsburgh Chemistry Department Chair, Professor David Waldeck for his assistance in preparation of this manuscript. A very important contribution to this project is the collaboration with research groups of the Engineering Department at the University of Pittsburgh and particularly with Professor Jean Blachere. Thanks also to **dmc**² analytical laboratory for their valuable input. Support from ONR (N0001-96-1-0735 and N00014-02-1-0327), NSF (Phys-0103048, CHE-9816820, and CHE-0404579), and ARO (W911NF-04-100191) is gratefully acknowledged.

Chapter 1

Introduction

Chemical imaging of morphologies involves the collection of both structural and spectral properties of the objects. It can be done by combining a variety of surface science techniques (Table 1). Spectroscopy plays a vital role in identifying chemical and biological species.

Table 1. Chemical imaging by conventional surface science techniques.

Arrangement of atoms	Elemental composition	Electronic or Vibronic structure	Dynamic nano-structure	Adsorbed particles, sticking coefficients		Surface Science Techniques
x	x		?		STEM	scanning/transmission electron microscopy
x			?	x	AFM	scanning force microscopy
	x	x		x	AES	Auger electron spectroscopy
	x	x		x	XPS	X-ray photoemission spectroscopy
	x	x			NMR	nuclear magnetic resonance
		x	?		UV/VIS IR	optical spectroscopy

Conventional analysis of the experimental data relies heavily on known macroscopic properties of the investigated materials. However, for sub-micron-sized objects, one should take into account that quantum mechanical corrections play a more important role. Beside the obvious size-related effects such as light diffraction, quantization shows itself in the transition from molecular to bulk-like properties of the solids.¹

Since the goal of chemical imaging is to identify the species by their spectroscopic “fingerprints”, it is very important to know how their spectra change due to the size effects. This work is focused primarily on the resonance phenomena. The first type of resonance that is considered is the extrinsic cluster size effect due to collective electronic or lattice excitations (Mie resonance). A surface plasmon-polariton resonance of metallic nanometer-sized particles that are reflecting UV/Visible light is studied in application to silver diffusion and cluster growth in a glass matrix (Chapters 2-5).

Near-field microscopy has already demonstrated the spatial resolution beyond the diffraction limit.^{2,3} Recently, a frequency dependent contrast on a scale of about 100 nm was reported for forward scattered detection.⁴ Here the demonstration of the near-field “fingerprint” of a single vibrational mode of a carbonyl group was accomplished with 10 nm resolution for backscattered detection (Chapters 6-10). Enhanced apertureless near-field microscopy was used for nanometer scale chemical imaging of di-iron nonacarbonyl polycrystalline flakes on a gold surface.⁵

Chapter 2

SILVER BLEED THROUGH EFFECT

Preface

This project has been initiated in response to ever increasing challenges that glass scientists face in today's automotive business. Glass-ceramic enamel coatings around the outer periphery of automotive glass provide UV protection to the adhesive holding the glass to the vehicle frame. The black enamel coatings also provide a decorative function by hiding adhesive layer unevenness and enhancing the appearance of the glass. Enamels are screen printed on cut sheets of soda-lime-silica float glass, dried, and sintered (vitrified) during the forming and heat strengthening of the substrate. "Deep bend" forming processes require the highest performance anti-stick enamels.

For rear window glass (back lites), the dried enamel is typically overprinted with silver paste heater bands and bus bars before sintering. Routine processing requirements for color development, opacity, voids, firing conditions, silver migration, and effects on glass strength become a real challenge in face of pending legislation that bans or limits the use of leaded frit. New research is needed to develop lead-free enamels that perform comparably as leaded products. Enamels with zinc and bismuth borosilicate frits have been determined to approach the performance of lead.⁶ Bismuth borosilicate frits have superior chemical durability in comparison to zinc borosilicate frits.⁷

Manufacturing of the complex shaped windows requires the glass to be 'press formed' in between two matching mold surfaces. The mold faces have to be lined with ceramic or stainless steel fiber cloth to protect the glass surface. Several approaches are used to develop enamels that do not stick to the mold lining: (1) the molten state of the enamel is carefully controlled by adjusting its composition to suit the time-temperature conditions of the press-forming operation, (2) metal rich (e.g., 10-15% of Fe) compositions are used where the oxidation of metal hardens the enamel to restrict flow and resist sticking, (3) the enamel composition can be carefully formulated so that the glassy portion of the enamel crystallizes just prior to the press-form operation and prevents wetting of the lining.⁸

The aesthetic function of these blacks includes hiding conductive silver defogger bands and bus bars. Various studies have demonstrated that heat-activated transport of Ag^+ cations into the glass substrate (*silver bleed-through*) causes discoloration. There are patents available that claim improvements in stopping silver bleed-through by the addition, before paste formation, of silicon, boron, carbon, lead, silver, sulfur and/or sulfides.⁹

Statement of Problem

This case is concerned with the study of chemistries related to the silver bleed-through problem in crystallizing automotive black enamels.

Known patented methods of hiding silver bands have not proven entirely satisfactory for different reasons: cost considerations (silver), the need for special operating conditions for highly reducing agents (silicon, boron), low acid resistance (lithium) or environmental concerns (lead). Metal additives may cause additional gas evolution during the firing process.

On the other hand, frits based on zinc borosilicate with sulfur have relatively low durability. Attempts to improve anti-bleed-through properties of bismuth borosilicate frits using a similar approach have had little success because of bismuth reduction by sulfur. This negatively affects both the crystallization kinetics and the effectiveness of sulfur in reducing Ag^+ cations.

Purpose of Study

Up to the mid 1970s the bulk solid and the planar surface were the favorite topics of materials science. Now, nanostructured metal has largely taken their position. Inclusions of metallic nanocrystals affect the optical and electronic properties of amorphous materials. Alkali ion mobility and inter-diffusion of Ag or Au into glass film also change the dielectric properties of a material. The rich variety of colors exhibited by nanoscopic metals has been behind their use in fine arts, photographic development and industrial metal coloring processes. In most recent years, attention has focused on the application of such small particles in surface-enhanced spectroscopy, photo catalysis, nonlinear optics and selective solar materials.¹⁰⁻¹³ Two important areas of interest are glass staining for decoration and “silver bleed-through” in automotive industry.

The connection between the absorption band of colloidal metal particles and band structure in metals such as silver and gold was an incentive for many studies^{14, 15} on size dependent optical properties of metal particles, and spectroscopic analysis of metal clusters in vacuum was facilitated by advances in molecular beam techniques.^{16, 17}

The mechanism of silver bleed-through as shown in Figure 1 is quite complex, especially in conjunction with partial crystallization of the frit. It involves both physical wicking of silver paste and ionic activity. The role of the solvent can be critical. The kinetics of the ion exchange and crystallization are still not quite well understood and subject to different interpretations.^{18, 19}

The purpose of this case study is to gain a better understanding of ionic activity mechanisms and the kinetics of reactive glass-ceramic enamels through the development of effective experimental techniques and building verifiable theoretical models. The results can be applied to the development of higher aesthetic value automotive enamels based on bismuth borosilicate and other crystallizing lead-free frits.

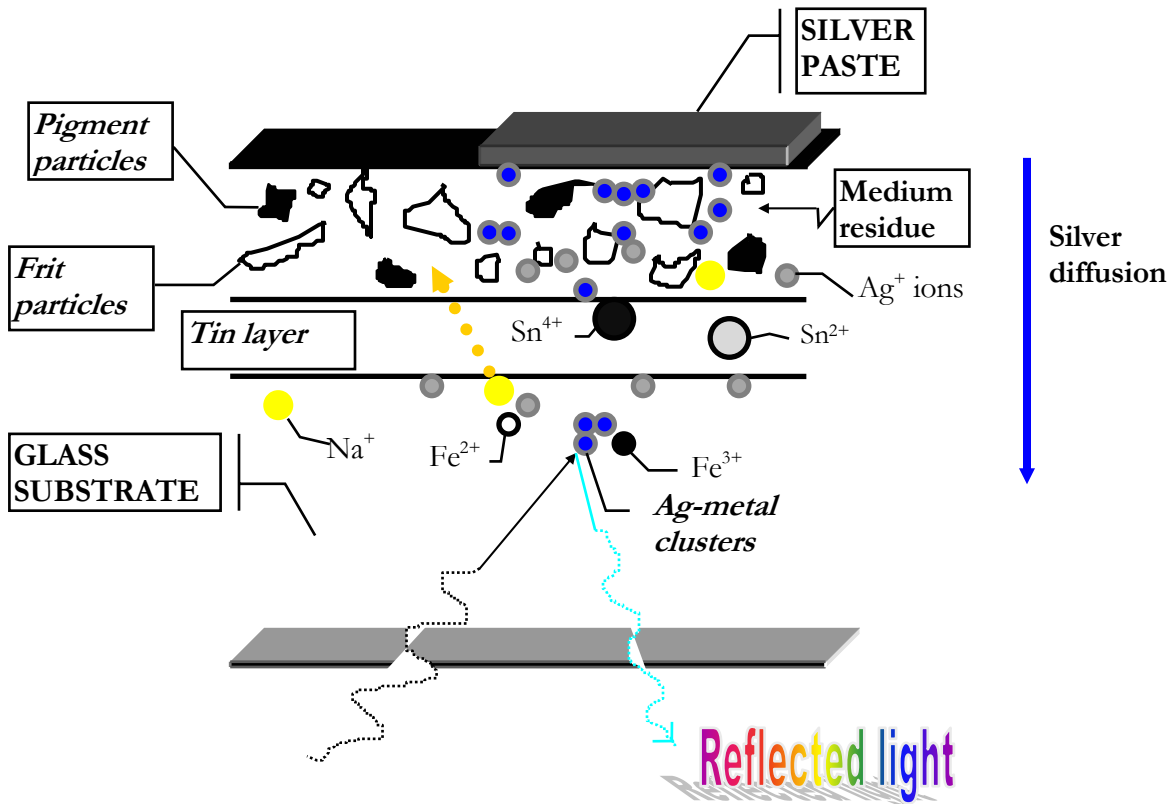


Figure 1. Discoloration Mechanism

Description of Terms

Typical enamel composition is a mixture of powder and medium in a ratio of (3.5 to 5) : 1 by weight. The powder consists of 25-30% of pigments (e.g., copper chromite spinel, CuCr_2O_4) with sub-micron particle size and frit particles (ca. 4 μm). Usually, frit contains 2-3% sodium. Silver paste is based on 50-80% of Ag, 2-4% frit for better registration on glass enamel surface, and the vehicle (solvent). The conventional carrying vehicle or medium is composed of oil (for controllable transfer through the screen), resins for better 'green' strength, and other modifiers (e.g., for high loading medium with compact packing of solids). It is important for the vehicle to provide good particle suspension, good rheological properties, storage stability, and to burn off completely upon firing of the enamel. The other alternative is UV curable (polymerizable) medium. The standard substrate is PPG Solex soda-lime-silica ($\text{Na}_2\text{O}\cdot 2\text{CaO}\cdot 6\text{SiO}_2$) float glass with enamel printed over the tin side.²⁰ Commercial glass may have 0.5-1.5% of Fe_2O_3 and other polyvalent metal oxides²¹ used for refining of the melt. Silver paste wicking through dried enamel with Ag^+ cation migration during the firing cycle and ion exchange of Ag^+ with Na^+ under the glass substrate surface, followed by reduction of Ag^+ into Ag^0 is referred to as the 'silver bleed-through problem'. Colloidal silver particles in the substrate cause discoloration of black enamel.

Sintering of enamels is achieved by heat treatment for about 3-5 minutes above the glass transition temperature (550°C to 705°C) to form the vitreous phase. To inhibit molten glass flow and sticking to the press bend lining at above softening temperature, metal additives that form a hardening oxide network are used in leaded frits. A similar effect is observed in lead-free reactive systems, which change their physical properties during glass formation. Assisted formation of microcrystalline phases inhibits the molten glass flow.

EXPERIMENTAL CONDITIONS OF SILVER DIFFUSION STUDY

Theoretical model parameters of mass transport and kinetics in glass-ceramic materials, particle size and concentration profiles (TEM, SEM, Variable Temperature XRD), as well as optical properties (UV/VIS spectroscopy, computations) of silver nanoparticles in glass need to be analyzed.

Technological Constraints of Problem

Glass-ceramic enamel compositions for automotive applications include frits for vitrification after firing, mixed with coloring and opacifying crystalline pigments and minor fraction additives. Chemical compositions of the glass frit fluxes generally are within the PbO-B₂O₃-SiO₂, ZnO-B₂O₃-SiO₂, or Bi₂O₃-B₂O₃-SiO₂ systems. The choice of oxides determines the properties of the glass frits, for example their softening point, thermal expansion coefficient and resistance to bases and acids. In general, colorless glass frits contain oxides selected from:

SiO₂, Al₂O₃, TiO₂, ZnO, MgO, Li₂O, B₂O₃, Bi₂O₃, SnO₂, MoO₃, CaO, Na₂O, La₂O₃, ZrO₂, MnO, BaO, K₂O, V₂O₅

Other oxides may also be present:

P₂O₅, Cr₂O₃, Fe₂O₃, CuO, NiO, CoO, Sb₂O₃, WO₃, CeO₂

It has been shown that frits based on borosilicates are preferred over other lead-free frits. These are well-known glass-forming compositions. They typically contain silicon dioxide (15-40% by weight), boron trioxide (5-25% by weight), and zinc and/or bismuth oxide (30 to 65%).

The addition of reducing agents should be done with caution as some agents (e.g., MnS, FeS, Cu₂S, CdS, and PbS) color the vitreous mass. In addition, the introduction of these sulfides in large quantities can cause liquid-phase separation within the molten mass. The kinetics of redox reactions should be tailored to the crystallization rates in reactive systems, which is a major factor influencing the sticking behavior of frits (See Figure 2 and Figure 3).²² In turn the crystallization kinetics and hence the entire frit composition have to be tailored to suit manufacturing heating rates (Figure 4).

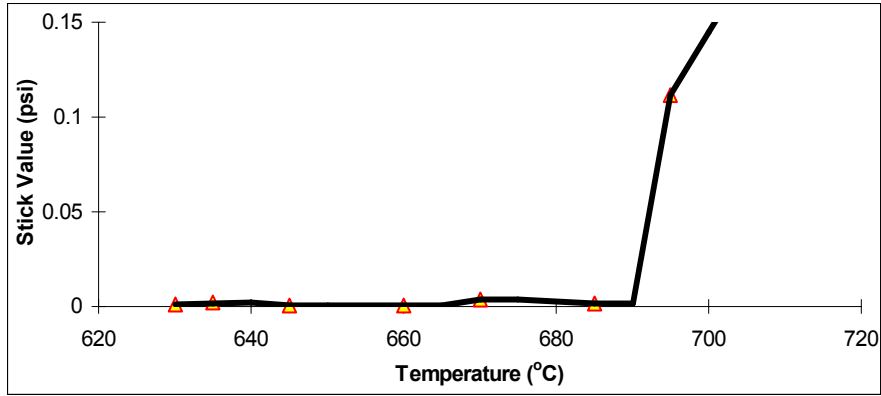


Figure 2. Substrate Stick Response

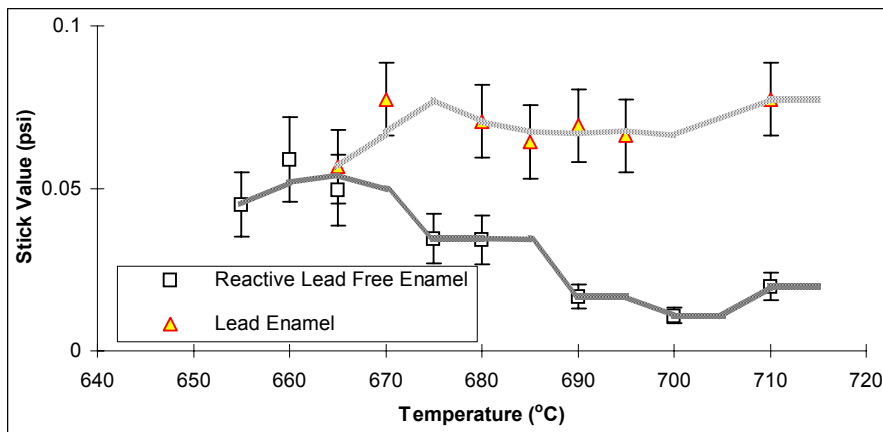


Figure 3. Enamel Stick Response: the force required to pull the press-pad off the surface depends on the reactivity of the enamel

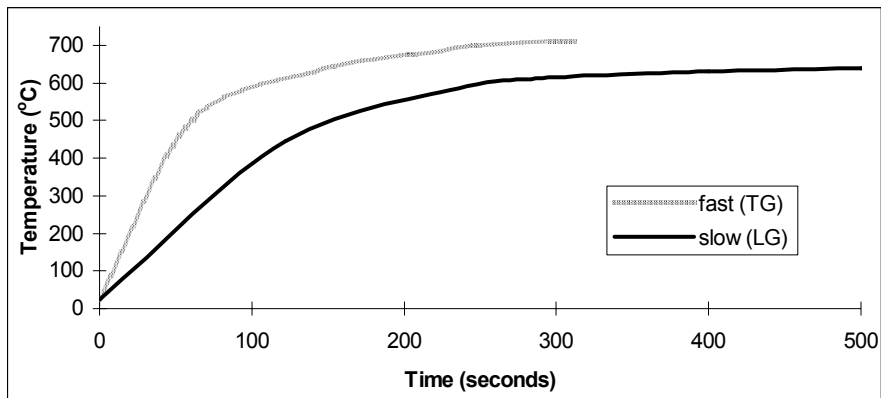


Figure 4. Typical Heating Curves for Laminated (LG) and Tempered (TG) Automotive Glass Forming⁷

Since the manufacturing heat rates are the pre-determined factors, the choice of the reactive glass system depends primarily on adhesive properties of enamel. The lower the force of adhesion between the press-pad (covered by the stainless steel cloth) and the enamel surface at the firing temperatures (Figure 3), the better are the esthetic properties of the automotive glass that is supposed to match a specially designed shape after the press-bending.

The addition of pigments raises the enamel temperature ca. 10°C because of extra heat absorption. Pigments generally increase the packing density due to smaller particle size and provide extra barriers to silver bleed-through. Yet, for research purposes, it is expected to be useful to experiment with pure frit without pigments in order to facilitate quantitative elemental microanalysis.

Fundamental Challenges of Problem

A theoretical model describing the silver bleed-through mechanism will be built. The main issues related to the problem are

- Kinetics of crystallization in reactive automotive enamels during firing
- Physics and chemistry of silver in enamel; the role of pigments and the vehicle/solvent during drying and firing
- Surface kinetics of silver, tin, oxygen; as well as iron and other polyvalent elements in glass substrate
- Selectivity of reducing agents toward different ions; the role of glass frit matrix on the activities of the species
- Ion exchange and formation of colloidal particles of silver metal inside the surface of soda-lime-silica glass substrate
- Discoloration as a function of silver cluster formation

Among other problems, incorporation of redox reactions into crystallization kinetics theory is the biggest challenge. Activity of reducing agents depends on their blending into frit structure.⁹

Analysis of the surface kinetics should include both balancing of reduction/oxidation activities of the catalysts and analysis of agglomeration/dissociation processes at firing temperatures.²⁰

The goal of this project was to find and apply a reliable experimental technique to accurately quantify all factors responsible for silver bleed-through: the mass transport (ion migration), the depth of ion's interdiffusion into substrate, and the formation of silver colloidal particles (See Table 2 and Table 3).

At all stages, the oxidation state of reagents needs to be determined and the role of different species in glass substrate (Table 4) has to be verified.

Table 2. Color Variations with Particle Size²³

Particle Size	Transmitted Light	Reflected Light
10 -- 20 nm	Yellow	Blue
25 -- 30 nm	Red	Green
35 -- 45 nm	Reddish-purple	Yellowish-green
50 -- 60 nm	Bluish-purple	Yellowish-green
70 -- 80 nm	Blue	Brown
120 -- 130 nm	Green	Brown

Table 3. The chromaticity and the reflection peak height, ΔR (relative to the incident light intensity) changes with the increase in silver colloid size²¹

Fe₂O₃ content in substrate (wt. %)	Ag colloid size (nm) measured by XRD	Color	ΔR (%)
0.53	6.5	Brown	0.14
0.65	8.5	Bluish-brown	0.42
1.4	15	Blue	1.67

Table 4. Color vs. Time and Firing Temperature²¹

Fe₂O₃ content in substrate (wt. %)	Firing conditions: Temperature (°C)	Firing conditions: Time (minutes)	Color
0.53	690	4	Brown
1.4	690	4	Blue
0.65	670	4	Brown
0.65	690	4	Bluish-brown
0.65	700	4	Bluish-brown
0.65	700	6	Blue

NUMERICAL MODELS AND RESEARCH METHODS: SILVER BLEEDTHROUGH

It has been shown that sticking properties (Figure 5) and discoloration (Table 3) depend on both temperature and heating rate. The competition between different processes can significantly change the rates of ion migration and the kinetics of various redox reactions because of the physical changes in their environments. To be able to understand and predict the pathways of such changes during the glass formation, one needs to develop techniques for collecting essential information about the presence and distribution of active species in dynamic equilibrium. The ultimate goal is to collect the complete information about mobility and redox activity of the species depending on the physical properties of the environment, and their roles in affecting the rates of nucleation and crystal growth.

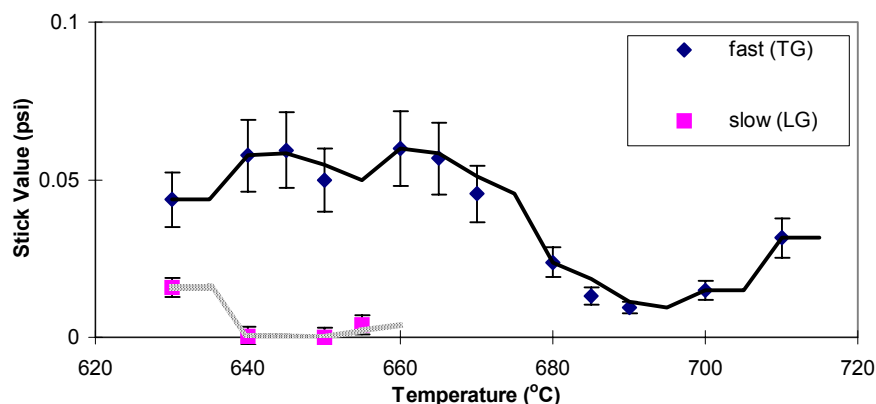


Figure 5. Lead-free Reactive System Stick Response after 2.2 psi Pressing as a Function of Temperature and Heating Rate

The instrumentation required for this task should have sufficient resolution for depth profile analysis of micro- and colloidal crystals distribution as well as give information about the distribution of species in different oxidation states. Additionally, we have to determine the high-temperature redox activity of the species depending on their incorporation in glass matrix, temperature, and other properties of the

environment. Spectroscopic studies are needed to analyze any correlation between silver cluster formation in a substrate and the effect of discoloration. Theoretical models should be verifiable and useful in predicting bleed-through effects in reactive systems and designing bleed-through-resistant systems. The basic theoretical and experimental tools described below will form a framework for the collection, analysis and interpretation of experimental data and for building a more comprehensive theoretical model.

Selection of Theoretical Models

a. Mass transport kinetics and atomic arrangements

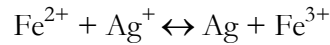
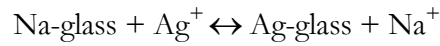
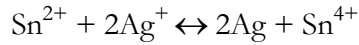
Diffusion of reactive species through glass-ceramic enamel can be affected by the particle's packing density (the role of medium), sticking coefficients, and glass transformation. The rates of redox reactions depend not only on the temperature and medium properties but also on the physical state of active species, such as incorporation into the glass frit matrix. In addition, it was observed²¹ that the amount of Sn (characteristic to the float glass process) penetrating into the glass substrate depends not only on alkali but also on Fe content.

As already discussed, properties of glasses are strongly dependent on their thermal histories with regard to both structure and annealing state. This has been proven to be true also for ionic transport. There is evidence that transport properties in soda-lime glass near transformation range depend on the content of OH groups.²⁴ The Si-O network of the glass may be regarded stable during ion-exchange (cementation exchange) processes. For the conditions that

- the mobilities of both cations in the melt are high compared with those in the glass and
- phase-boundary reactions between melt and glass are very fast,

the interdiffusion of the ions in the glass is the rate-determining factor. The interdiffusion coefficient, \check{D} , describing this binary diffusion process, may depend on concentration (Appendix A).

A numerical simulation of silver diffusion in multilayer glass structure in the presence of electrical fields created by sodium inter-diffusion was done by using the following chemical model of ion exchange (Appendix B):



Crystallization processes are of fundamental scientific and technological significance for the field of glass science since they are intimately linked with the problem of glass formability. In order to describe nonequilibrium processes of quasi-open crystallization systems, characterized by continuous flow of heat and matter, one uses thermodynamic macroscopic quantities²⁵⁻³⁴ and the elementary processes of attachment of individual building units to and from the crystallization front (interface).

Interface kinetics is influenced by heat transport, mass transport of building units, and growth kinetics.³⁵ The central question to be solved using the kinetic approach is the entering mechanism of the fluid atoms at the crystal interface. Several different models have been used to describe the interface kinetics: lattice models (including dislocations, impurities, and surface reconstruction)³⁶ and molecular dynamics.³³

Classical models consider growth laws derived for different atomic configurations of the crystal face: atomically rough face (half-crystal or *kink* positions) and atomically smooth face (singular and vicinal).³⁷⁻³⁹ Molecular dynamics (MD) considers the dynamics of individual atoms and therefore has certain advantages for microscopic interpretation. Considerable progress in MD has been made through the availability of powerful computers.

The lattice models do not take into account exchange potential between the atoms, vacancies and fluid inclusions in the crystal and more importantly provide no real time dynamic information. On the other hand, the MD Lennard-Jones approach is a rigorous statistical treatment of the fluid and the crystalline state. Both traditional and modern approaches to modeling crystallization can serve as powerful tools in the data analysis and interpretation, for both silver nanocrystals and partial crystallization of enamel.

b. Electronic and optical properties of metal nanoparticles

Structure on a “nanoscale” means particle dimensions of 1-100 nm. Molecular clusters are beyond the scope of this analysis. Clusters (synonymously, nanoparticles) as defined here are aggregates of atoms in the order of 100 to 10^7 atoms each. These scales lie in the “mesoscopic range” where correlation lengths or mean free paths of the bulk are larger than the particle size. A general description of optical properties of nanosized metals is not available because of the wide variability of topological patterns. These materials in the bulk state are classified as metals with a high density of electronic states near the Fermi-level. As clusters, they do not necessarily exhibit metallic properties.

The classic electrodynamic description of the extinction (due to optical absorption and elastic scattering) of the metallic sphere was first developed by Mie with the assumption that the optical polarizability of the whole cluster is sufficiently described by one uniform quantity $\epsilon(\omega, \dots)$ extrapolated from solid state models. In order to keep the Maxwellian boundary conditions applicable, $\epsilon(\omega, \dots)$ has to be properly modified by quantum theoretical extension terms to include cluster-size and interface effects.

Mie’s theory is based on a spherical mode expansion method.⁴⁰ These modes have, for the case of metallic clusters, later been interpreted as being due to surface plasmon polaritons (plasmons coupled to a macroscopic electromagnetic field) and eddy current modes. Besides these collective excitations of the conduction electrons, single electron-hole excitations (similar to interband transitions) occur in real clusters. In these modes, the cylindrical symmetry of the field is combined with the spherical symmetry of the cluster.

The more or less sharp resonances, the Mie plasmon polaritons, are caused by the fact that collective oscillations of the conduction electrons are excited by the electromagnetic wave. Their dipole and higher multipole moments are due to surface charging, which is extremely effective for spherical shapes. The material-specific differences of the resonances are mainly due to the band structure effects and material-specific excitation-relaxation processes of conduction electrons.

While Mie gave expressions for the scattering constant S , absorption constant A , and extinction constant E (the sum of the above) of a macroscopic system of clusters (with a filling factor $f = 10^{-6}$ for

normalization) embedded in nonabsorbent matrix, now it is common to derive the corresponding single-cluster cross-sections.

If the nanoparticles are sufficiently small ($2R \ll \lambda$; "quasi-static regime"), the dipolar plasmon absorption losses determine the total extinction. This holds for Ag and Au particles in the visible light resonance region only if $2R < 10$ nm. Although extinction of the dipolar mode always predominates, the importance of higher multipoles for A and S increases with particle size due to appreciable phase shifts. If the higher multipolar modes are excited, the dipolar scattering can no longer be neglected, and the quasi-static approximation is surpassed.

Clusters have a very high fraction of surface atoms, which accentuates the importance of the surface effects, e.g. in catalysis. The cluster interface with surrounding medium (matrix) also gives rise to new properties compared to the atomic and solid states. Classification of clusters according to the number N of atoms per cluster therefore reflects the role of the surface atoms. Large clusters have $500 \leq N \leq 10^7$ ($3.3 \text{ nm} \leq 2R_{Na} \leq 100 \text{ nm}$ with assumption of bulk interatomic distances; $0.5 \leq N_s/N_v \leq 0.9$). For very small clusters ($2 < N \leq 20$), the distinction between surface and interior atoms is not possible. N_s/N_v is still about 20% for clusters with 3000 atoms and true bulk conditions with $N_s/N_v \ll 1$ are reached only for $N \geq 10^5$.

There are two major cluster-size effects: intrinsic effects concerning specific changes in volume and surface material properties and extrinsic effects, the size dependent responses to external fields and forces irrespective of the intrinsic effects. Experiments on intrinsic effects particularly focus on the question of how electronic and structural cluster properties such as ionization potential, binding energy, chemical reactivity, crystallographic structure, melting temperature, or optical properties vary as a function of particle size and geometry. For the spacing of electron energy levels, this is known as the quantum size effect. In case of metal clusters, one is interested in how metallic behavior develops with cluster size. This is probably correlated with size dependent structural phase transitions in the clusters.¹ Lattice contraction effects are particularly important for very small clusters (e.g., atomic distances in Ag_2 and Au_2 are 0.21 nm and 0.253 nm, respectively versus corresponding next neighbor distances of 0.325 nm in bulk material). Examples of extrinsic cluster size effects are the collective electronic or lattice excitations (Mie resonances).

Intimately related to optical excitation are photo-dissociation processes (fragmentation or even evaporation of the cluster). Photo-fragmentation and optical absorption are assumed to be strongly correlated (beam-depletion spectroscopy).

Very small clusters have been successfully treated by molecular quantum-chemical ab initio methods. An extension of all-electron calculations to small clusters ($20 < N \leq 500$) seems possible, at least for elements with low atomic number. For large clusters, solid-state physics techniques have been applied. Potential box, jellium, and other models with simplifying assumptions have been applied to small cluster sizes. Strong changes have been observed for different physical properties in various size regimes ranging from a few to 10^6 atoms indicating convergence towards the solid state. There are indications that a molecular-to-solid state transition of the electronic and geometric properties takes place in narrow size regions.

Electrical and optical properties of the clusters strongly depend on shape and environmental effects. For densely packed clusters, topological effects (and their influence on cluster-cluster interactions) need to be considered. Particle-particle and particle-matrix interactions complicate the interpretation of optical spectra.

Preliminary experimental data and a preliminary theoretical analysis of silver diffusion and optical properties of silver clusters in glass substrate are given in appendices A and B.

Selection of Instrumentation and Techniques

The transformation of physical properties of reactive enamels can be investigated by using standard techniques such as TG/DTA and/or DSC, and Variable Temperature XRD; in special cases also by etching and optical methods such as stress birefringence,^{41, 42} the "schlieren" method, and scattered light (laser) tomography⁴³ may be used. TEM will be useful for studying crystallization across the thickness of enamel.

Chemical diffusion processes in glasses have been measured by numerous methods. Most of these are based on a chemical analysis of diffusing species: wet chemical analysis, X-ray fluorescence analysis, radiochemical analysis and more recently, electron probe microanalysis (EPMA) method (Figure 6). XRD and TEM again are useful for studying silver colloids.²¹ Colorimetric methods will be applied to evaluate the final effect of discoloration in reflected light, caused by ion exchange.

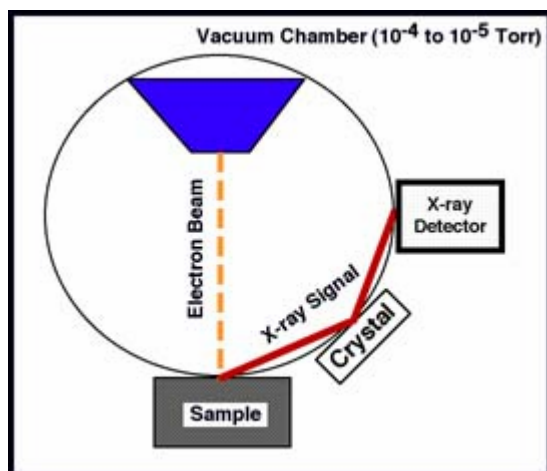


Figure 6. Electron Probe Microanalysis (EPMA)

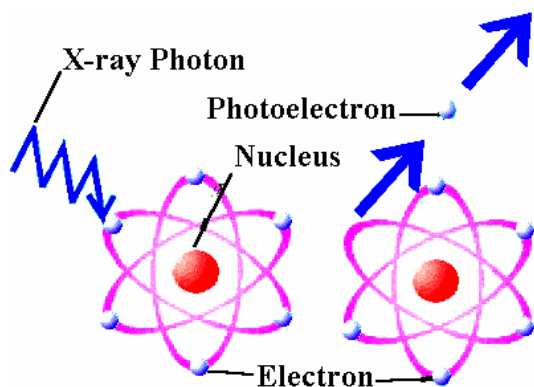


Figure 7. X-Ray Photoemission Spectroscopy

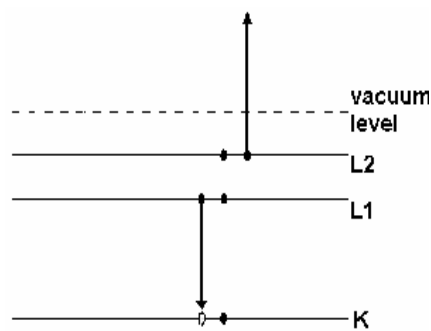


Figure 8. Auger Electron Spectroscopy

A significant challenge is to track dynamic changes in transport of reactive species at high temperature typical of glass processing. Various surface science techniques are available that can be used in combination to obtain information about what mechanisms are rate determining at different stages of the studied process. XPS (Figure 7), AES (Figure 8) and NMR techniques can provide information about oxidation states of reactive species. The proposed approach to these problems is a combination of measurements of the species kinetics in model experiments and computer simulations based on tested theoretical models. The most important of them and most useful are UV/VIS spectroscopy and microprobe analyses.

Collection of Data

The data most essential to our understanding of the bleed-through mechanism are the spectrum of reflected and transmitted light, the size and spatial distribution of silver colloidal particles (as well as their morphology) in a substrate, concentration of silver (both metal and cations) across the coating as a function of time and temperature, the rates of the redox reactions depending on the local environment of reactive species and the temperature. For crystallizing enamel, one needs to know both softening point and glass transition temperature. Packing density, low shear glass frit viscosity as a function of temperature, concentration profile of tin, iron and other polyvalent elements in glass substrate, along with information about their oxidation states have to be determined in order to build a complete model of silver bleed-through.

The composition of enamel should be carefully designed for each experiment in order to minimize the number of interfering factors, especially at the initial stages of the research. Although *in situ* measurement of dynamic parameters is very problematic because of the high temperatures of glass formation, indirect information about them can be collected by varying the firing time of the trials. Careful sample preparation is the key to the successful experiment because uncontrolled trace element variations can affect nucleation and crystal growth, thus changing the physical environment for silver transport and chemistry. Variations of alkali ion concentrations in a substrate may affect the ion exchange and silver transport and eventually bismuth chemistry⁴⁴ and bismuth borosilicate frit crystallization.

Analysis of Data

In order to build the basis for a quantitative description of crystallization and bleed-through phenomena, we need to extensively employ theoretical models and use a combination of several different techniques for cross-calibration.^{45,46}

The size of microcrystals can be evaluated from XRD peak profiles by using Scherrer's equation⁴⁷ and TEM. The major crystal growth models⁴⁸⁻⁷² can be useful as discussed above to interpret crystallization kinetics data. The N-particles system is modeled using Newtonian equations of motion (energy balance)³⁴ as

$$m_i \cdot \frac{d^2}{dt^2} r_i = -\frac{\partial}{\partial r_i} U(r_1 \dots r_N) - \frac{\partial}{\partial r_i} W(r_1 \dots r_N) + F_i(r_i, t) \quad (1)$$

where $W(r_1 \dots r_N)$ is the external contribution to the potential energy (boundaries), $F_i(r_i, t)$ represents the additional forces acting on the i -th particle and the function $U(r_1 \dots r_N)$ is parametrically (ϵ is the energy and σ is the size scale parameter respectively) determined by the Lennard-Jones potential as

$$\sum_{i < j} U(r_{ij}) = \sum_{i < j} 4\epsilon [(\sigma/r_{ij})^{12} - (\sigma/r_{ij})^6] \quad (2)$$

The most critical part of the analysis is extracting from experimental data the information about the presence of chemically active species and the rates of reactions.⁷³ Activities of reactive species depending on temperature and degree of association with neighboring atoms (chemical bonding)^{74, 75} critically affect shifts of redox reaction equilibrium.

RESULTS AND DISCUSSION FOR SILVER BLEED THROUGH

The samples of 20 μm thick automotive black enamel (borosilicate frit with copper chromium pigment) with silver paste overprint were fired at 593°C to 704°C (1100°F to 1300°F) for 4-6 minutes. The results for reflectance spectra (specular excluded) of the areas under silver are compared to standards (STD) and summarized in Figure 9. After 6 minutes at 649°C (1200°F), the staining effect is observed which corresponds to absorption by small silver particles. At 704°C (1300°F), the height of a resonance peak at 440 nm is increasing with time, which is usually attributed to increased number of 10-15 nm size particles.

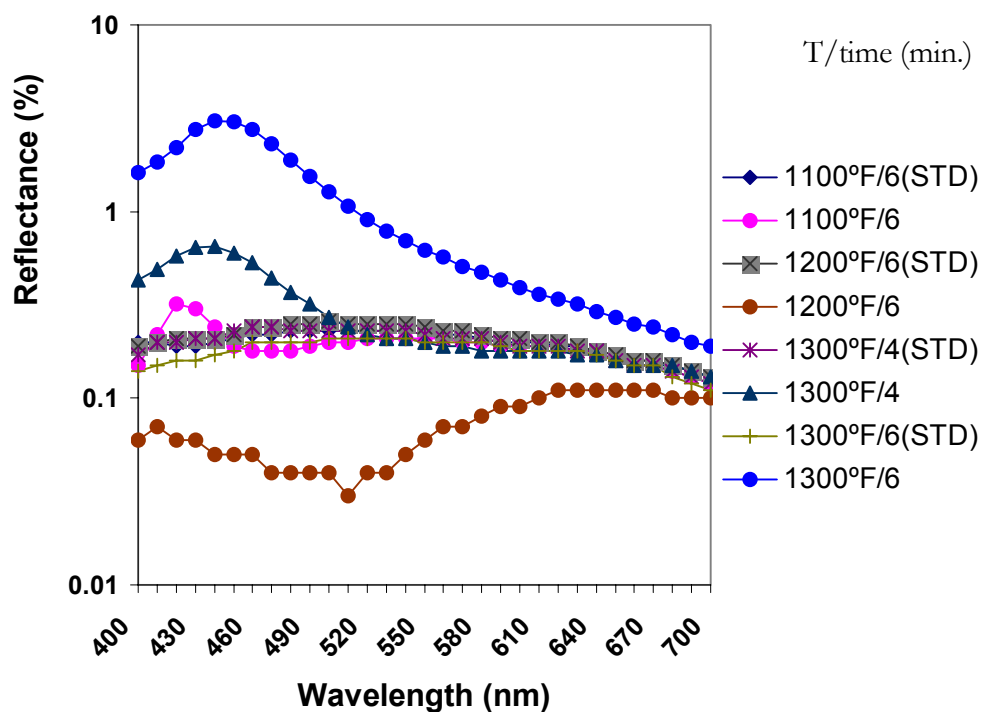


Figure 9. Summary of reflectance spectra (small area, specular excluded) after silver bleed-through compared to standard blacks (STD).

Recent findings of correlation between colorimetric data and silver colloid size, polyvalent elements concentration in substrate, firing time and temperature ⁷ as well as correlation between sticking coefficients and heating rates, temperature, and DSC/TA data ²¹ provide a good background. On the other hand, there are unconfirmed indications in favor of different theoretical models describing mass transport (wicking) and ionic activity of silver. The role of tin and oxygen is also not clear. In order to identify the key factors, the current research emphasizes the quantitative analysis of the data and building computer simulation models.

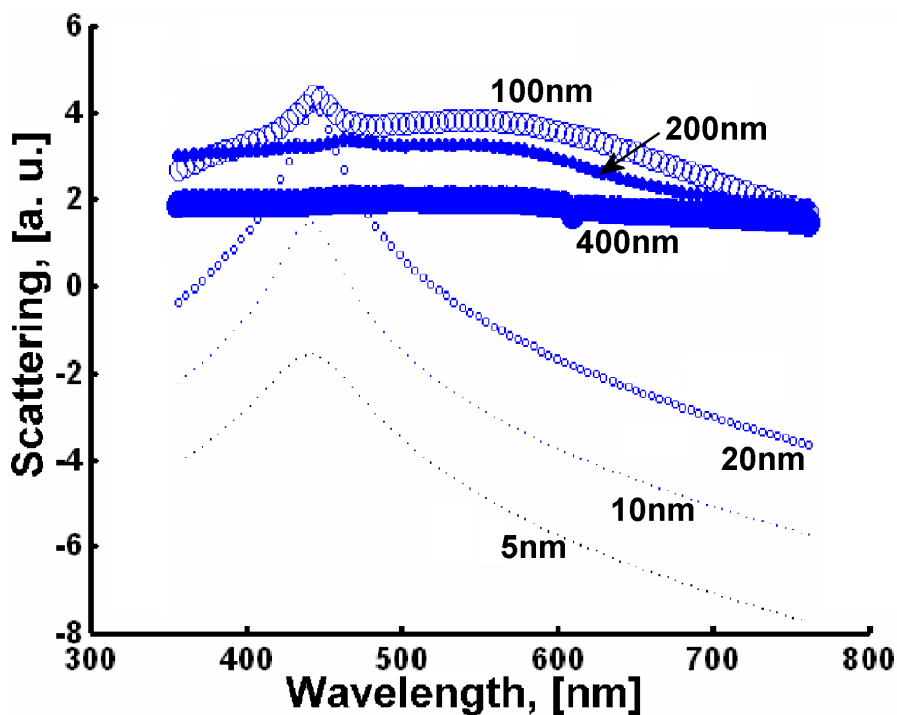


Figure 10. Relative changes in the light scattering cross-section on silver clusters in glass (logarithmic scale), depending on the diameter of the silver particle.

MATLAB computations based on Mie theory (Appendix C) showed that scattering peaks in "blue" light region correspond to silver colloids of 15-20 nm size embedded in matrix with refractive index of ~ 1.7 (Figure 10), different from 1.51 for soda-lime-silica glass. Such changes in refractive index are in agreement with those reported elsewhere (Appendix A). For complete analysis, one needs to take into consideration dipolar absorption and cluster-cluster interaction. ⁷⁶ The simplistic model used for these calculations may not fully reflect the interaction at the colloid-matrix interface. Specifically, adsorbing species could change the interior electron density distribution as well as relaxation frequency. ⁷⁷⁻⁷⁹

Diffuse reflectance spectra should differ from the spectrum of the incident light, depending on the total extinction cross-section of the object, which includes both scattering and absorption. The experimentally observed changes in the reflectance spectra (Figure 9) as the firing temperature increased from 593°C to 704°C can be explained by the competition between the rate of silver diffusion across the enamel and the rate of neutral silver crystallization in the substrate.⁸⁰ A small peak at 430 nm observed for the temperature 593°C already indicates a substantial presence of silver particles with sizes above 10 nm. At the same time, the 593/6 reflectance plot at the wavelengths above 450 nm is slightly below the standard, which can be related to growing absorption by the particles of smaller sizes. At 649°C, the absorption became so strong that it overshadowed the scattering by the growing number of large particles. This trend has then reversed itself, yielding the bright blue discoloration at even higher temperatures. However, it is also possible that, under certain conditions, the 10-20 nm size particles are thermodynamically unstable due to competition between the association mechanisms and the external forces at the boundaries of the particle. This may result in bimodal particle size distribution, with very small particles “bleaching” the reflectance at the shorter wavelengths and the larger crystals, whose association energy forces are strong enough for continued growth, contributing to reflectance at the longer wavelengths. Experimental evidence of the yellow discoloration of glass enamels caused by formation of silver clusters was reported elsewhere.⁸¹⁻⁸³

Preliminary results of SEM microanalysis have been obtained on samples sputter-coated with 2-3 nm Pd film (to reduce charging). Experimental profiles of silver concentration showed an anomaly that cannot be explained by the simple model of neutral particles diffusion: low concentration deeper into enamel but substantial presence of silver inside the glass substrate. A similar pattern was observed for distribution of clusters of nanoparticles. The results for trials fired at 704°C (6 minutes) were inconclusive. However, distinct images of about 50 nm size spheres were observed for 649°C trials. The inclusion particles distribution was concentrated mostly in the glass substrate near the interface and became gradually more scarce deeper into the glass (Figure 11). The low energy (5 keV) electron beam focused on one of the particles gave a relatively higher intensity of radiation characteristic of palladium (Figure 12), due to the coating. This might also be an indication of a "telegraphing" effect of enlarged Ag-Pd clusters.⁸⁴ Impinging Pd atoms are trapped in the surface potential and may either be inelastically scattered or stick (after surface diffusion) to growing Ag-Pd clusters.⁸⁵ TEM microanalysis (Appendix D) of the non-coated samples showed the particles of the regular sizes, between 10 nm and 20 nm, concentrated in the areas of higher silver concentration.

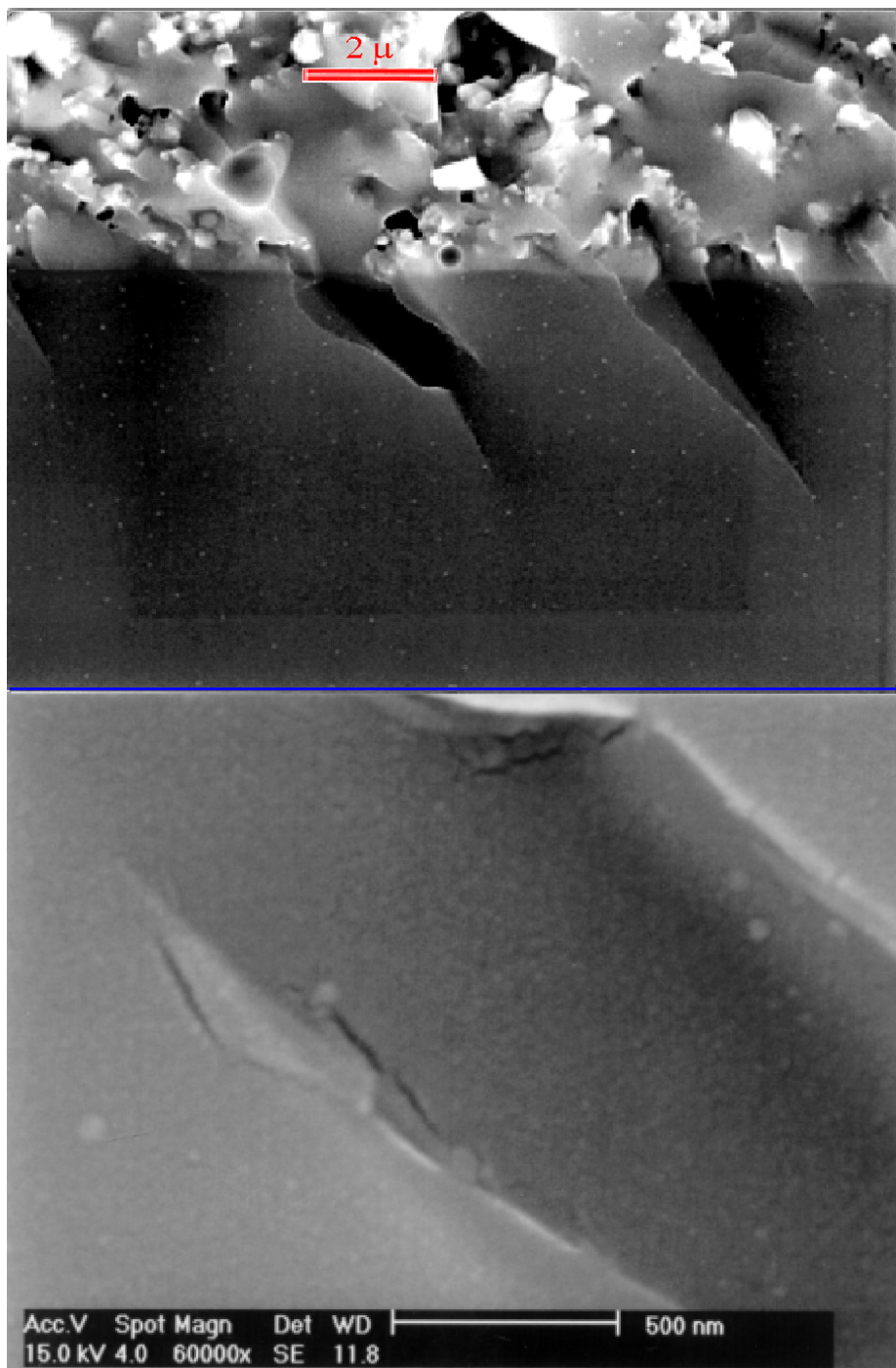


Figure 11. SEM photo of silver clusters coated with palladium: low (top) and high (bottom) resolution.

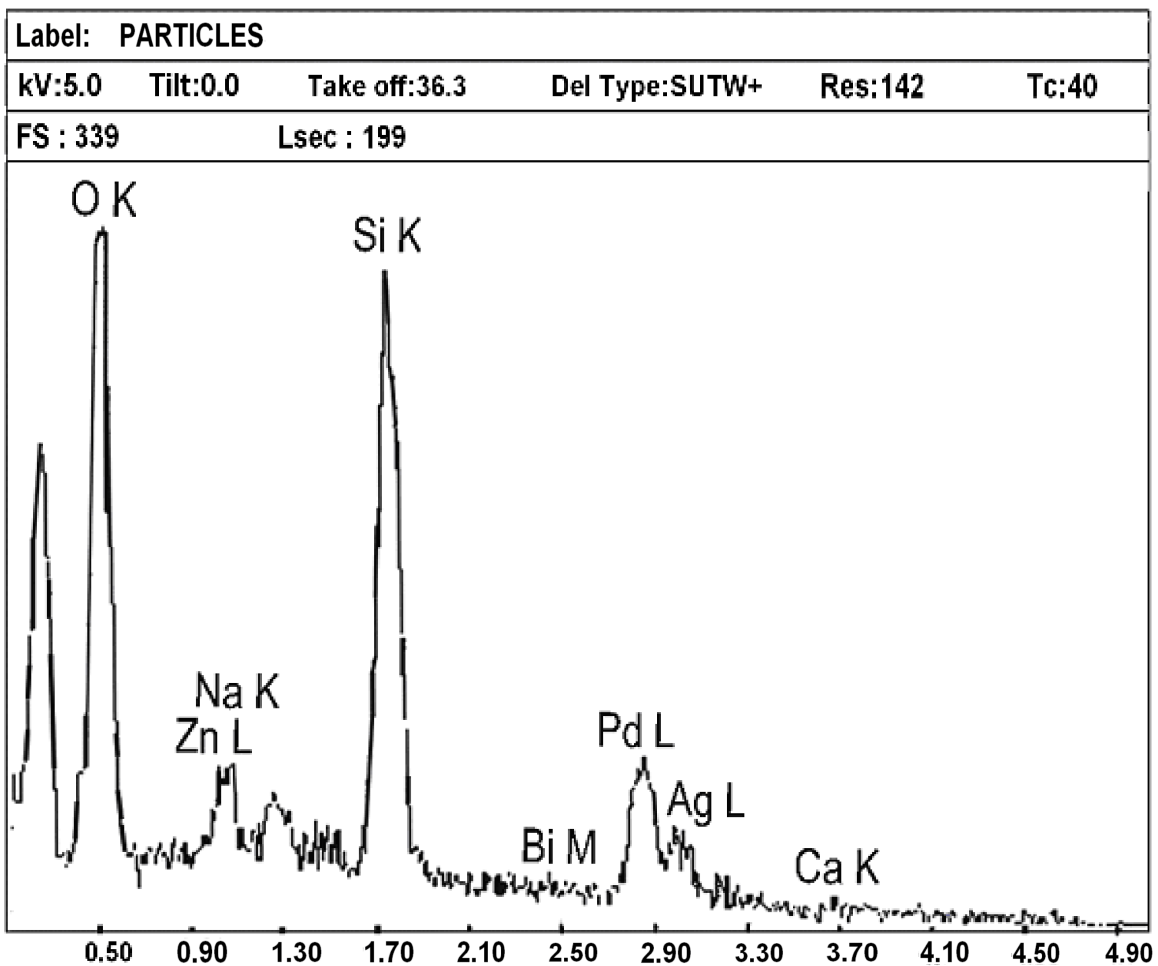


Figure 12. SEM microprobe of the area containing silver cluster area.

The results of Visual Basic 6.0 simulation (see Figure 13)⁸⁰ suggest that after a certain point in time the silver concentration profile has an anomalous maximum just inside the glass substrate. That is exactly what was observed experimentally (Figures 11, 14). The Ag L line intensity (see Figure 12), normalized by the Si K line, changes across the glass interfaces in agreement with this theoretical model. Another important observation is that, after the critical point, the initial sharp rise in the rate of increase of the amount of silver in the substrate is followed by a gradual decay, which is reflected in the time dependence of the silver reduction rate (bottom plot in Figure 13). This is in line with the temperature dependence of the experimental reflectance spectra (Figure 9) showing the competition between dipolar absorption (dominant at 649°C but not at 593°C or 704°C) and scattering.

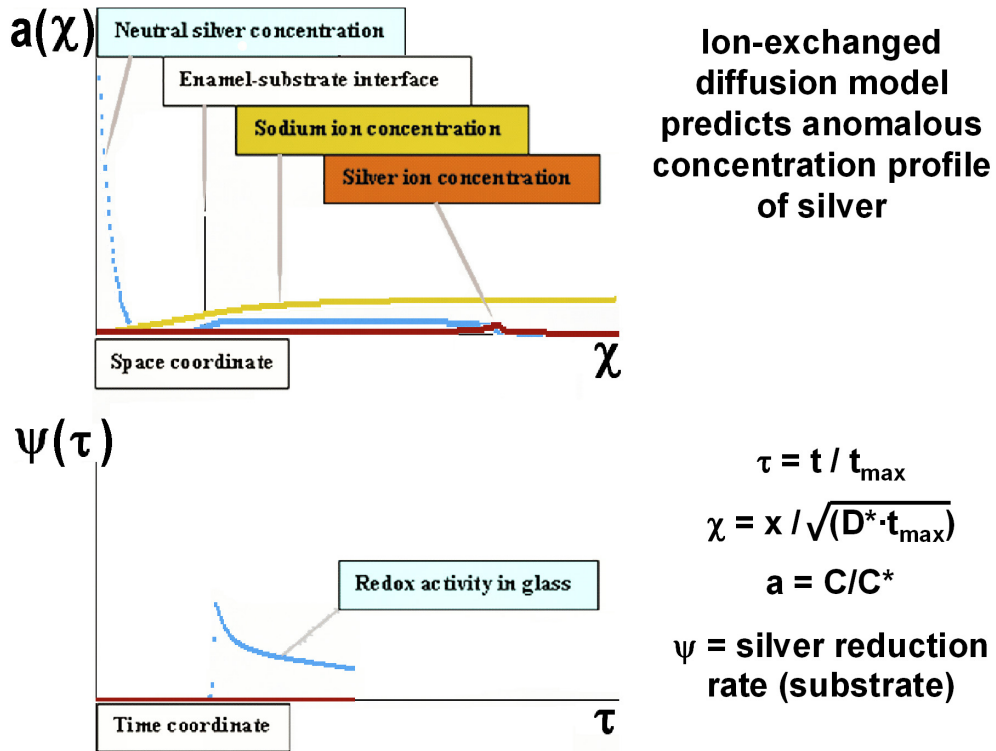


Figure 13. Ion-exchange diffusion model simulations (Appendix E). Inverse gradient of silver concentration is predicted at the glass-enamel interface.

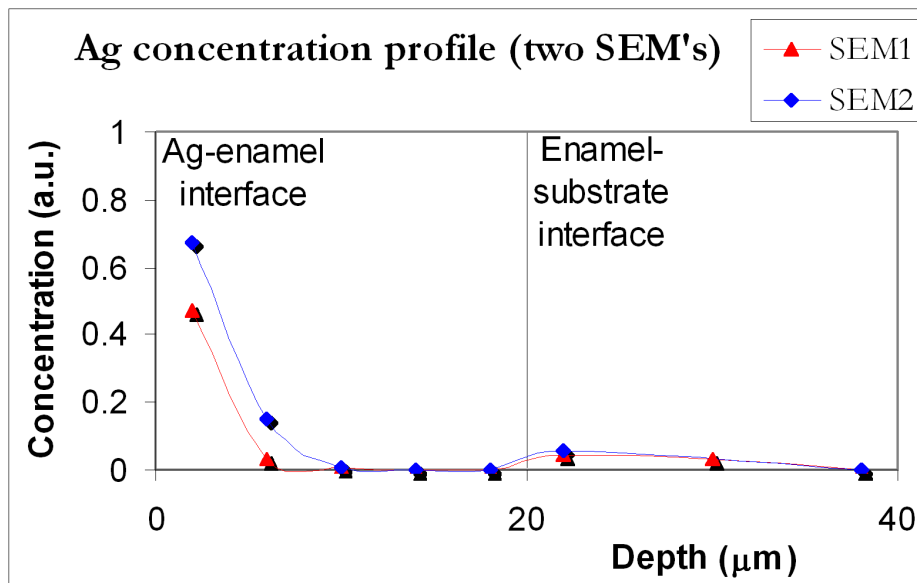


Figure 14. Results of SEM analyses.

SEM analysis with two different microscopes (as shown below in Figure 14) showed that the silver concentration is highest in the areas where the clusters of Ag-Pd particles have been observed with an SEM1 microscope (Figure 11). The measurements on SEM2 (20 kV electron beam) were conducted on the side of the sample not coated with palladium.

These data are in a good agreement with each other and in line with the chemical diffusion models described above. The 20kV data are slightly higher due to stronger effect of increased electron energy on excitation of Ag L compared to the Si K reference line (normalized to the weight percentage of Si in a test region). Both concentration profiles indicate that the silver concentration is highest in the regions where Ag clusters have been observed with SEM1 (see Figure 11) in the sample fired at 649°C (1200°F) for six minutes.

The data indicate a good correlation with selected theoretical models. Additional corrections can be done to account for various modifications of the cluster interface (e.g., electron spill-out,⁸⁶ especially for colloids with uneven number of Ag atoms could lead to the observed "red" shift).

Significance of Findings

Quantitative or semi-quantitative description of silver bleed-through crystallizing glass-ceramic enamels is an important contribution to the understanding of glass chemistry and physical properties. It will provide tools that are more efficient for development of new frit systems, which is currently relying on a labor intensive 'trial-and-error' approach with primary stress on analytical work rather than sophisticated materials design. The following findings are of great interest not only for automotive enamel designers. Electronic applications of glass, strengthening of glass, staining of glass, improving chemical surface properties of glass or removal of radioactive waste by incorporation in glass are directly related to ionic transport.

REVIEW OF NEAR FIELD INFRARED MICROSCOPY

Infrared spectroscopy is widely used to measure the concentrations of specific chemical groups by detecting the vibrational resonance absorption. The line shape of such “fingerprint” resonances can yield information about conformations and intermolecular interactions. However, it is practically not possible to focus infrared radiation into a spot much smaller than ten or even twenty micrometers.

Near-field optical microscopy provides us with superior resolving capability of optical and spectroscopic imaging/sensing by “confining” photons within a region much smaller than their wavelength. This resolution improvement is very attractive if it can be associated with spectroscopy. This chapter overviews near-field infrared microscopy and spectroscopy for chemical analysis and imaging of materials at the nanometer scale. After brief introduction to near-field optics, key elements for realization of near-field IR microscopy are described. Chapters 8-10 discuss several experimental results of near-field IR spectroscopy using several kinds of IR sources.

Vibrational spectroscopy is a widely used and sensitive technique for detection and characterization of molecules. Biochemical information on real-life systems only comes from analysis of biomolecules in their physiological environment, i.e. as components of cells, tissues, and biological fluids. Such information is not easy to obtain with conventional mid-infrared (5 - 12 μm) spectroscopic techniques since diffraction limits the spatial resolution to no better than half of the wavelength. This low resolution prevents IR microscopy and spectroscopy of single sub-cellular features routinely observable with conventional visible light microscopes.

A number of books and review articles covering important topics in near-field scanning optical microscopy have been published by leading researchers in the field. Near-field microscopy has rapidly evolved from a novel technique to a powerful instrument for the study of materials science and biological systems. Scanning near-field optical microscopy (SNOM) makes it routinely possible to overcome the fundamental diffraction limit of standard (far-field) microscopy. Recently, aperture-based infrared SNOM performed in the spectroscopic mode, using the Vanderbilt University free

electron laser, started delivering spatially-resolved information on the distribution of chemical species and on other laterally-fluctuating properties.¹⁰¹ This approach achieves chemical selectivity by detecting specific vibrational modes with high lateral resolution. The approach was successfully tested in the case of diamond films and of AlGaAs-GaAs quantum wires. High resolution well beyond the diffraction limit of far-field microscopy was tested, in particular, by studying microcircuits. These practical examples show the great potential of this new technique both in materials science and in life sciences.

To understand the near field behavior of the diffracted infrared light, Dazzi et al. have developed a model (utilizing the R-matrix propagation algorithm based on the differential theory of grating) for an homogeneous layer in which a buried localized absorbing region is enclosed, the latter is characterized by two narrow absorption bands, similar to those of the polymer that was previously studied experimentally.^{102, 103} They showed that the shape of the diffracted electric field is similar to the shape of the absorbing region only when the size of this region is larger than the wavelength (Figure 15). When it is smaller, one has to discuss the concept of lateral resolution in such

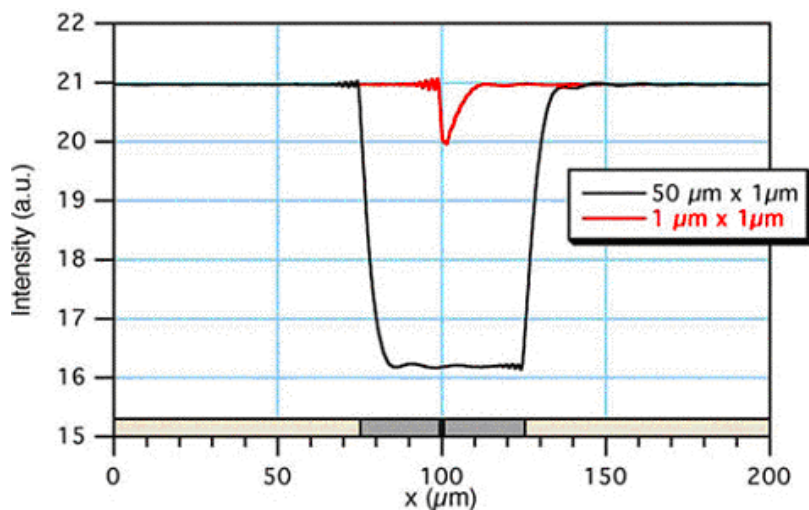


Figure 15. Intensity distribution of the diffracted electric field at 10 nm from the surface for the absorbing region sizes smaller (red) and larger (black) than the wavelength of 5 μm .¹⁰¹

microscopy and the main parameters limiting this resolution. The resolving power is usually used as a characteristic of an optical instrument but in this case they show that this parameter is closely related to the absorbing region's size and shape. Their spectral analysis reveals that the absorption bands are not only localized above the absorbing region but can be detected away from the source as well. The bands

may also be shifted by several wavenumbers in some cases. This shift seems to be created only by the dispersion of the real part of the refractive index induced by the bands of absorption, rather than by the imaginary part. Interestingly, it appears that the profile results in the linear sum of the real and imaginary part of the refractive index. Then, the diffracted electric field of a small (smaller than the wavelength) absorbing region exhibits a large spreading (Figure 16). The conclusion was that

constant wavelength mappings were practically impossible, at least in that configuration, although spectroscopic studies may bring valuable information about local properties of the sample. The advantage over the far field is that the spectroscopic contrast was not diluted over an area much larger than the absorbing region. One must be careful, however, of possible overlaps of spectra of the neighboring regions. Also, in order to get a correct spectrum of a sample it is necessary to collect the electric field much closer to the surface ($< \lambda/10$) than the near field extension ($\sim \lambda$). The overall conclusion of their theoretical results is that the use of near-field microscope is not straightforward and has to be done in a rigorous and cautious way to get relevant data. Different near-field configurations may lead to somewhat different conclusions. A solution to improve the resolution could be to illuminate the sample with a wide angular aperture in order to destroy the spatial coherence giving rise to the above mentioned diffraction patterns or to generate the evanescent field inside the sample, such as in the SNOM configuration.

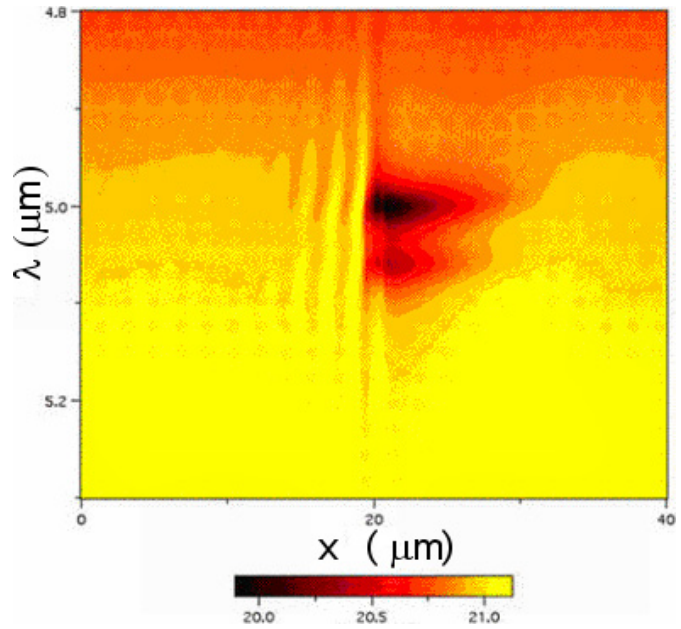


Figure 16. Linear mapping of an absorbing doublet in $1\mu\text{m} \times 1\mu\text{m}$ region centered at the abscissa of $20\mu\text{m}$. It exhibits wings extending spatially over several microns.¹⁰¹

Aperture-based SNOM suffers from low efficiency due to attenuation and absorption of light passing through a small metal-coated aperture. By using apertureless SNOM, where the light is scattered by a metallic needle, the resolution of the system can be substantially improved to around 20 nm, reports F. Keilmann.¹⁰⁴ Previously, Knoll, B. & Keilmann, F. demonstrated the resolution of about 100 nm.⁴

CHARACTERIZATION OF DI-IRON NONACARBONYL VIBRATIONAL DISPERSION

Tri- μ -carbonyl(hexacarbonyl)di-iron(0), $\text{Fe}_2(\text{CO})_9$, has been previously investigated for its interesting photochemistry (Figure 17).^{105, 106} This molecule can be used as a model for spectral properties of much larger organometallic systems. The importance of understanding the vibrational properties of CO bound to the heme iron was underscored by the recent discovery of very large electrochromic band shift, which arises from local electrostatic interactions that play a significant role in protein folding and assembly.¹⁰⁷ A near-field equivalent of a single vibrational mode (bridging carbonyl stretching band) of di-iron nonacarbonyl will be a good reference in developing high resolution chemical imaging.

Molecular and Crystal Structure***a. Factor group analysis***

The crystal structure of $\text{Fe}_2(\text{CO})_9$ is described by the space group $P6_{3/m} (C_{6h}^2)$, with two molecules per unit cell located at C_{3h} sites.^{108, 109} The molecular symmetry is D_{3h} and the vibrational representations of an isolated molecule of this symmetry are Γ_{vib} , $\Gamma_{\text{v}(\text{CO})_t}$, $\Gamma_{\text{v}(\text{CO})_b}$, $\Gamma_{\delta(\text{FeCO})}$, $\Gamma_{\text{v}(\text{Fe-C})}$, and $\Gamma_{\text{v}(\text{C-Fe-C})}$.¹¹⁰ The symmetry correlation of the $\text{v}(\text{CO})$ vibrational mode assignment¹¹¹ is summarized in Table 5. According to the selection rules of vibrational spectroscopy, the IR-/Raman-active E' modes of the D_{3h} molecular symmetry have two counterparts in the C_{6h} factor-group symmetry of the $\text{Fe}_2(\text{CO})_9$ crystal: E_{1u} (IR) and E_{2g} (Raman); $A''_2 (D_{3h})$ and the corresponding $A_u (C_{6h}^2)$ are infrared-unique modes, while $A'_1 (D_{3h})$, $E'' (D_{3h})$ and $A_g (C_{6h}^2)$, $E_{1g} (C_{6h}^2)$ respectively are Raman-unique modes.¹¹⁰

Despite several attempts to completely assign the vibrational frequencies for $\text{Fe}_2(\text{CO})_9$, with the first one dating back to 1974,¹¹² no quantitative frequency dependence of its dielectric function has been reported so far. The most complete analysis has been done by Jang et al.:¹¹³ they summarized the

earlier experimental data and proposed tentative band assignments to close the gap between theoretical (Dunning's standard double- ζ contraction¹¹⁴ of Huzinaga's primitive sets¹¹⁵ plus polarization) and experimental results.

Table 5. $\nu(\text{CO})$ region assignment correlation for $\text{Fe}_2(\text{CO})_9$.

Vibro-modes	Molecule, D_{3h}		Solid, $P6_3/m$	
	ν assignment ¹⁰⁷	Irreducible representation	Site, C_{3h}	Crystal, C_{6h}^2
$\nu(\text{CO})_t$	ν_1	A'_1	A'	A_g
				B_u
	ν_{11}	E'	E'	E_{2g}
				E_{1u}
	ν_{23}	A''_2	A''	B_g
				A_u
ν_{29}	E''	E''	E_{1g}	
			E_{2u}	
$\nu(\text{CO})_b$	ν_2	A'_1	A'	A_g
				B_u
	ν_{12}	E'	E'	E_{2g}
				E_{1u}

b. Isomerization

$\text{Fe}_2(\text{CO})_9$ complex is known to undergo thermal decomposition at room temperature and/or under the focused infrared laser beam with average power > 150 mW.¹¹⁰ Primary decomposition products have been identified as $\text{Fe}_2(\text{CO})_8$ isomers.¹⁰⁵ The reaction in a solid matrix is reversible as long as there is sufficient amount of carbon monoxide present in the matrix. Poliakoff and Turner¹⁰⁵ deduced that the first decomposition product has a C_{2v} structure, with two bridging carbonyl groups and a double-bond between the iron atoms (Figure 17). It is possible that the loss of a terminal CO group is the

initial reaction with the C_s fragment quickly rearranging into the C_{2v} structure as C_s cannot satisfy the 'eighteen electron rule'. This structure results in lower intensity and more than 25 cm^{-1} decrease in the frequency of the bridging carbonyl band.¹⁰⁵ The subsequent isomerization reaction results in the formation of an unbridged $\text{Fe}_2(\text{CO})_8$ that is manifested by complete absence of the bridging band.

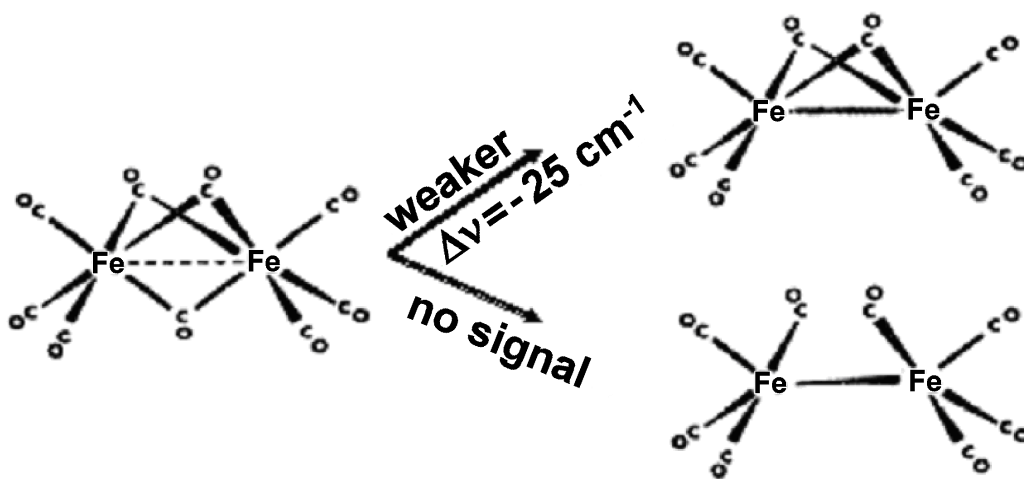


Figure 17. Decomposition effects.

Collection and Analysis of Infrared Spectra

Solid flakes of $\text{Fe}_2(\text{CO})_9$ (Aldrich, 99.5% pure) were ground with agate mortar and pestle into powder with the particle sizes of 50 to 200 nm and then mixed with CsCl (Sigma-Aldrich, 99.999% pure) fine powder (sub-micron particle sizes) at the ratios ranging from 0.5% to 30% wt. KBr was also used to verify the results. The mixture (100 mg) was pressed for 25 minutes at 40 N·m (30 ft·lb) into less than 0.5 mm thick pellets. IR transmission spectra were collected by the AVATAR 360 FT-IR E.S.P. spectrometer, with 0.5 cm^{-1} resolution (two data points per division) within spectral range of 400 to 4000 cm^{-1} (See Appendix F).

Absorption and reflection have been separated by collecting transmission spectra of the powders with varying low volume fractions f_v of $\text{Fe}_2(\text{CO})_9$. Thus, the imaginary part of refractive index, k can be determined as a function of wavenumber:

$$\alpha = \frac{4\pi}{c} \cdot k \cdot \nu, \quad (3)$$

where α is an absorption coefficient, ν is the wavenumber, and c is the speed of light.

A knowledge of the dielectric functions of the sample and the cantilever tip as a function of frequency permits a prediction of the near-field spectrum. Di-iron nonacarbonyl presents certain problems for direct Kramers-Kronig analysis of its spectra, which requires integration over the entire frequency range and measurement of the real part of refractive index away from the resonances. Instead, we used the best-fit combinations of Lorentzian oscillators to describe the experimental data:

$$\varepsilon(\nu) = \varepsilon_{\infty} + \sum_j \frac{S_j \nu_j^2}{\nu_j^2 - \nu^2 - i\nu\gamma_j}; \quad (4)$$

here ν_j is the center frequency, γ_j is the line width, and S_j is the oscillator strength.

The dielectric function of iron carbonyl at the low (relative to molecular vibrations) frequencies can be estimated from experimental data for effective macroscopic properties of iron carbonyl loaded silicon rubber.¹¹⁶ Angelescu et al. proved that such systems can be successfully analyzed by using the Bruggeman's formula:¹¹⁷

$$(1 - \eta) \cdot \frac{\varepsilon_1 - \varepsilon}{\varepsilon_1 + 2\varepsilon} + \eta \cdot \frac{\varepsilon_2 - \varepsilon}{\varepsilon_2 + 2\varepsilon} = 0 \quad (\varepsilon_1 = 3.2 + 0.25i), \quad (5)$$

where η is a fill factor of the medium 1.

A Matlab 5.0 iteration procedure was used to find the real and imaginary parts of dielectric constants for the core material and inclusions. Analysis of the resulting spectrum (see Figure 18) suggests that relatively high values of the real part of dielectric constant of iron carbonyl do not extend far from the microwave and have no significant contribution in the infrared region. The solution of the Bruggeman's formula for the core is $3.2+0.25i$, which is a quite reasonable value for silicon rubber.

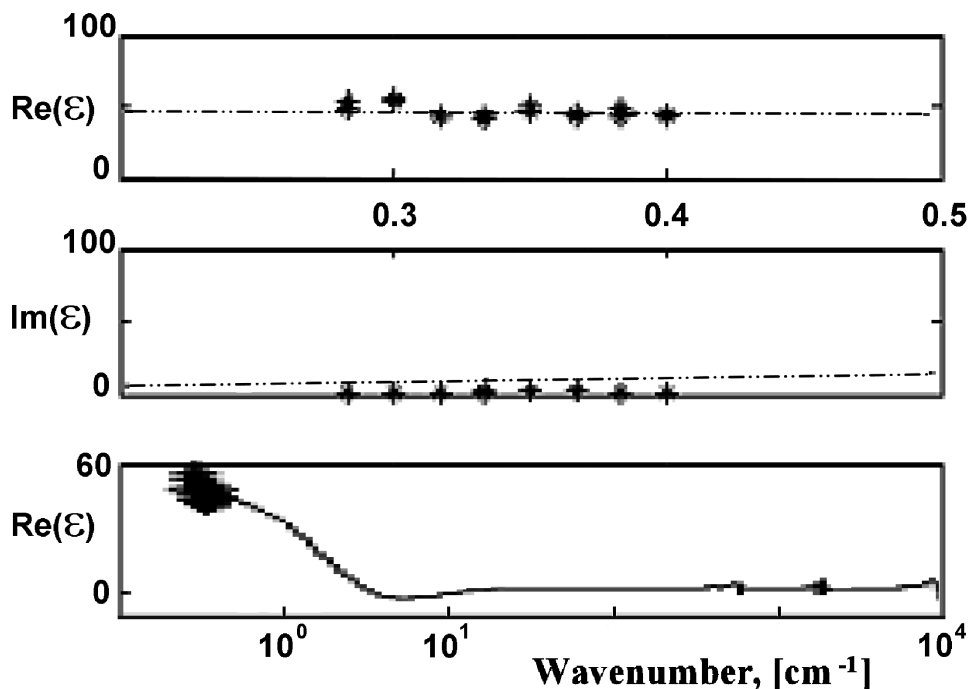


Figure 18. Dielectric function (real and imaginary) of iron carbonyl at low wavenumbers.

The parametric fitting of the $\text{Fe}_2(\text{CO})_9$ transmittance and reflectance spectra collected by Adams and Taylor¹¹¹ yields the high frequency part of dielectric function, ϵ_∞ in the range between 1.1 and 3.0 depending on interpretation of non-resonant background. An impurities peak (marked 'x' in the article's figure) near the bridging band can be interpreted by surface contamination with acyl halides, and the very strong side bands can be fitted by the hydrogen-bonding band and by a non-specific broad band centered at around 2450 cm^{-1} (See Appendix F). A much lower intensity 2450 cm^{-1} band and a similar band at 3750 cm^{-1} are observed in our transmittance and high-concentration extinction spectra (Figure 19). We attribute it to trace contamination introduced during the carbonyl extraction and purification process. It turns out though that we observed significant side-band distortion of the spectra (Figure 20) only for the pellets made of insufficiently fine (fine here means 100 to 200 nm) CsCl particles. Additional grinding eliminated the artifacts and allowed us to collect easily interpretable spectra (Figure 21).

By running tests at various concentrations of the analyte and by using different matrix materials (KBr, CsCl, CsI) it was possible to identify the peaks belonging to iron carbonyl correctly. Near the percolation (analyte particles grouping into small reflecting islands) threshold, we observed anomalous

reflection features, especially near the bridging band (Figure 22), which can be best fitted by a dielectric function with $\epsilon_\infty \approx 1.8 \div 1.9$.

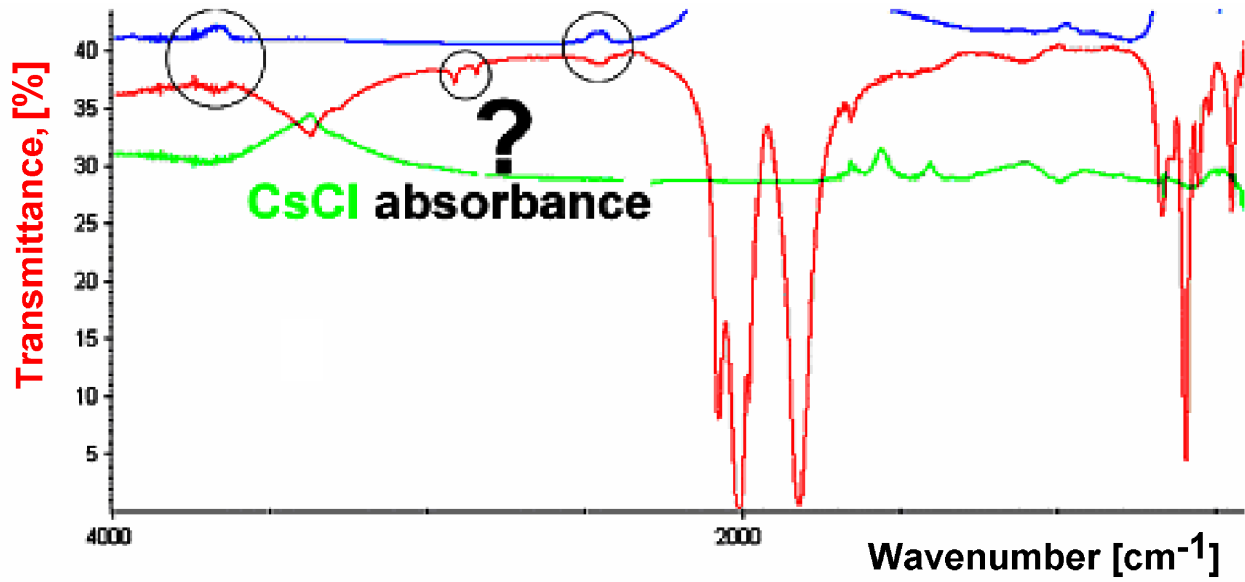


Figure 19. $\text{Fe}_2(\text{CO})_9$ in CsCl: $f_v \ll 1$ transmittance (red) compared to $f_v = 1/3$ extinction (a. u.) (blue) and CsCl absorbance (green).

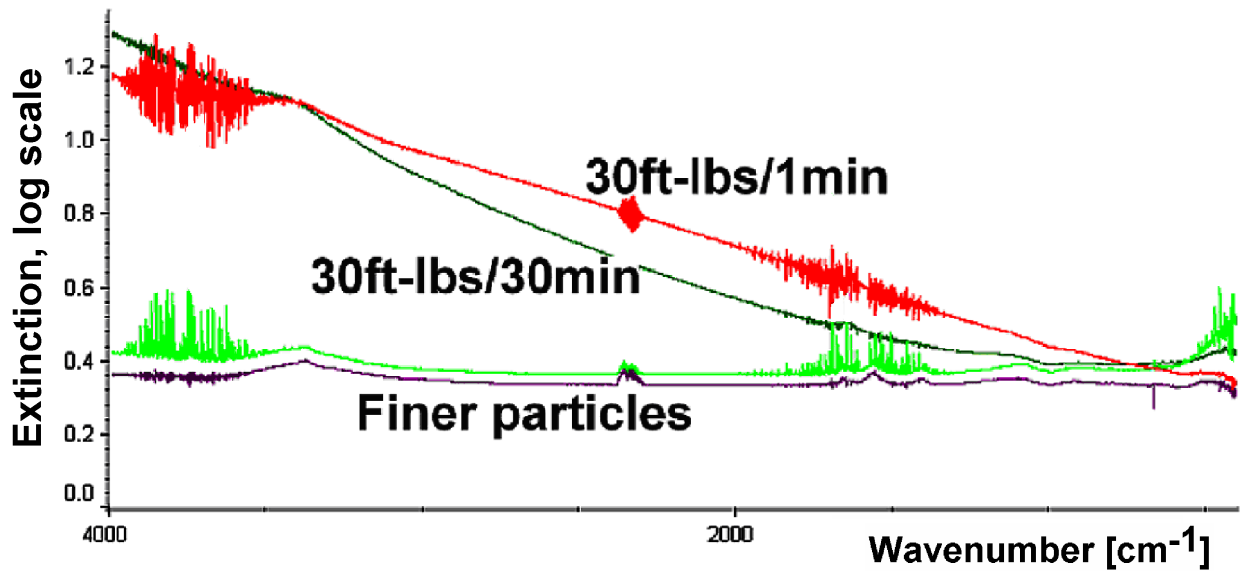


Figure 20. CsCl blank pellet (300 mg) extinction.

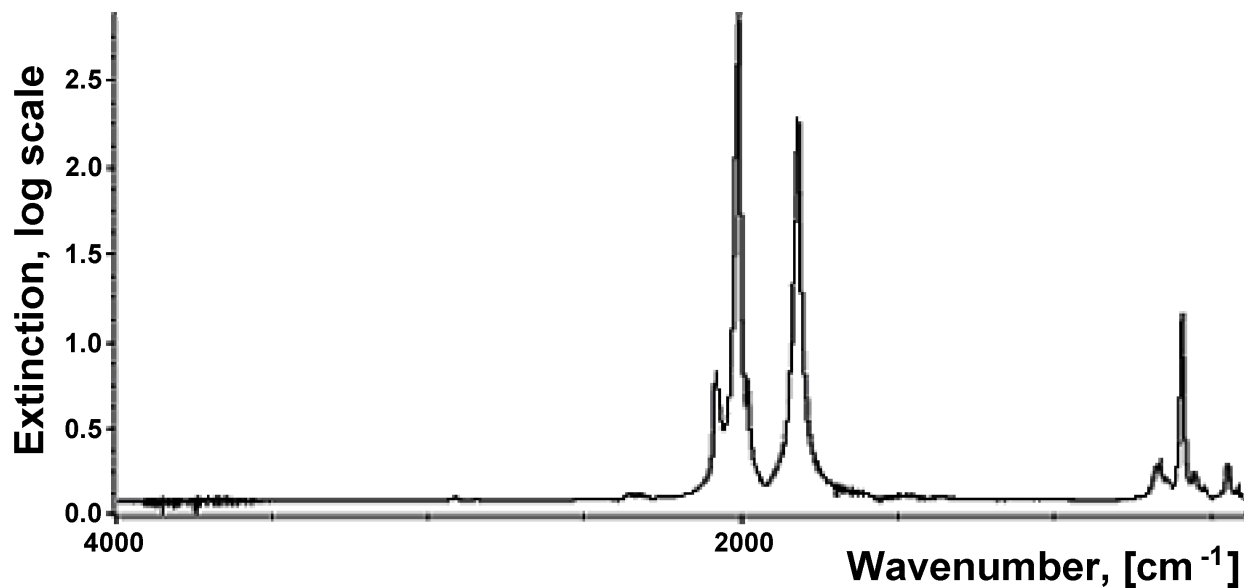


Figure 21. Background subtracted absorption coefficient at low concentrations.

Surface reflectance simulations for $\epsilon_\infty = 1, 1.2,$ and 3 do not match the observed pattern (Figure 23) but the multiple in-pellet reflections model does (Figure 22), though the experimental broadening is much bigger. The dielectric constant of CsCl was taken to lie between 1.3 and 1.7 for estimates of the corresponding error.

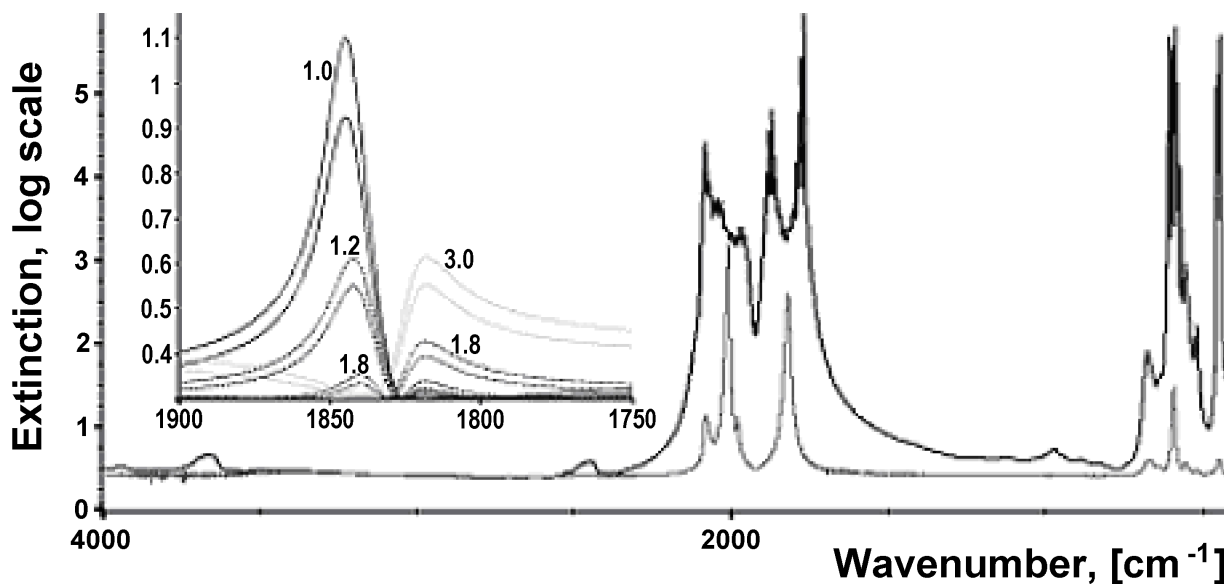


Figure 22. Total absorption at high concentrations (near percolation) in CsCl pellets; the insert: Simulated reflectance for different ϵ_∞ (high and low determined by CsCl refractive index).

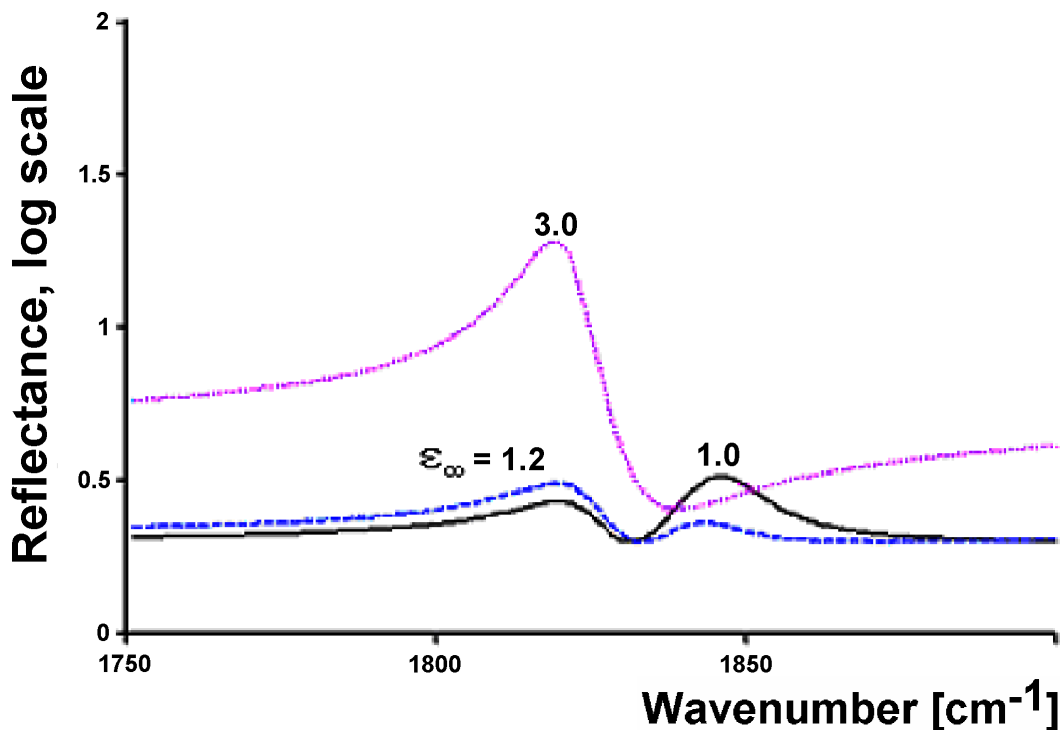


Figure 23. Surface reflectance of iron carbonyl (air interface) for $\epsilon_\infty = 1, 1.2, \text{ and } 3$.

This approach allows us to make assignment of resonant frequencies (all within 2 cm^{-1} of Adams and Taylor C_{6h}^2 assignments) ¹¹¹ and absolute oscillator strengths of vibrational transitions. Table 6 compares the fit of experimental data to the theoretical predictions by Jang et al. ¹¹³ The infrared intensities in km/mol have been converted to oscillator strengths:

$$I_j = \frac{\pi^2 S_j \nu_j^2}{100 n_r K}, \quad (6)$$

where n_r is the real part of refractive index and K is the molar concentration.

The E_{2g} (C_{6h}^2) and E_{1u} (C_{6h}^2) lines around 2015 cm^{-1} are compared to the E' (D_{3h}) line. Fitting of this band in the Adams and Taylor transmittance spectra ¹¹¹ is complicated by apparent unidentified band present at around 2030 cm^{-1} , while the spectra obtained after hard pressing of fine particles into CsCl matrix resulted in the Raman-unique E_{2g} (C_{6h}^2) band ¹¹⁰ being observed as a shoulder in the IR spectrum at 2012 cm^{-1} . The Lorentzian fit of this doublet to the experimental inhomogeneously

broadened line is poor. Alternatively, it can be (less accurately) described as a single line at 2015 cm^{-1} , with $S_j = 0.026$ and $\gamma_j = 27 \text{ cm}^{-1}$.

Table 6. Summary of vibrational oscillator strengths: t=terminal, b=bridging; *=depends on orientation; R**=this work.

Vibro-modes	Wavenumber, cm^{-1}		Oscillator Strength, S		
	R**	A&T ¹¹⁰	R**	Jang et al ¹¹²	A&T fit
$\nu(\text{Fe-C})_t$	422	422	weak	0	–
$\nu(\text{Fe-C})_t$ or $\delta(\text{FeCO})_t$	453	454	0.026	0.005	–
$\delta(\text{FeCO})_t$	525	525	weak	0	–
$\delta(\text{FeCO})_b$	561	560	weak	0	–
$\delta(\text{FeCO})_t$	598	600	0.117	0.141	0.03
$\delta(\text{FeCO})_t$	675	672	0.025	0.396	–
$\nu(\text{CO})_b$	1826	1826	0.046	0.065	0.04
$\nu(\text{CO})_t$	1986	1988	weak	0	Raman
$\nu(\text{CO})_t$	2012	2014	0.026	E' (D_{3h}): 0.103	Raman
$\nu(\text{CO})_t$	2018	2018	<0.06*		0.05*
$\nu(\text{CO})_t$	2086	2085	0.005	0.143	0.04

Comparison of the Adams and Taylor transmittance and reflectance spectra shows that the 2018 cm^{-1} band's average S_j value is approximately 1/3 of the oscillator strength in a direction normal to (0001) plane.¹¹¹ This ratio was used to estimate the maximum for the oscillator strength derived from the infrared transmittance spectra.

Summary of New Findings

The above experimental work improved on the results reported by Adams and Taylor,¹¹¹ by eliminating artifacts from the transmission spectrum and by studying samples with iron carbonyl concentrations from very low to very high. This research let us build a parametric model for dispersion of the dielectric function in the $\nu(\text{CO})$ region. In addition, the Bruggeman analysis was applied to

recent experimental data of nondestructive testing of iron carbonyl composites to evaluate the low frequency contributions.

A complete quantitative description of the $\text{Fe}_2(\text{CO})_9$ vibrational spectrum has been deduced from IR transmittance and reflectance data for a wide range of sample concentrations in CsCl and KBr. The resulting frequency dependence of the dielectric function satisfies the Kramers-Kronig condition. The experimental oscillator strengths are quite similar to the ones obtained from the theoretical infrared intensities, except for the terminal mode ν_{24} (A_2''). Observed central frequencies are in much better agreement with the experimental data reported by Adams and Taylor than with the results of theoretical computations, partly because the theory does not account for intermolecular coupling.

The main difference between the simulated molecular spectrum and the observed experimental spectra of the solid flakes is a splitting of a single terminal carbonyl vibrational mode ν_{12} (E') into two overlapping bands, E_{2g} (C_{6h}^2) and E_{1u} (C_{6h}^2). Surprisingly, the Raman-unique E_{2g} (C_{6h}^2) band was observed as a shoulder in the IR spectrum of $\text{Fe}_2(\text{CO})_9$ in CsCl matrix.

EXPERIMENTAL SETUP FOR ANSIM MICROSCOPY

Apertureless nearfield scanning infrared microscopy is based on original idea by Wessel¹¹⁸ and related IR work by Kawata^{119, 120} and Boccara.^{121, 122} It probes surface enhanced nonlinear optical processes. It can reveal sub-wavelength details because it uses a sharp probe to disturb evanescent fields near the light scattering objects rather than beam focusing. The perturbation of the local electromagnetic fields in turn induces detectable changes in the far field signal. The size of tip determines microscope's spatial resolution.

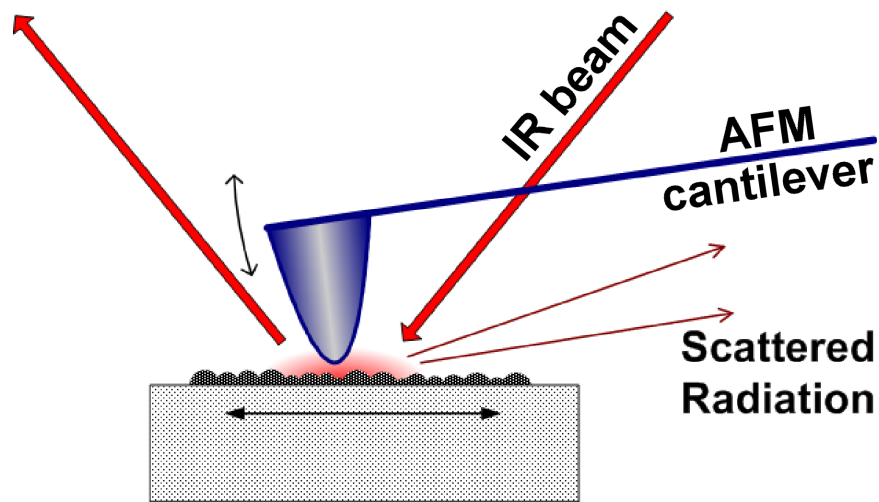


Figure 24. Basis of apertureless near-field scanning infrared microscopy.

An apparatus built in Professor Walker's laboratory at the University of Pittsburgh is based on a commercial atomic force microscope (MultiMode AFM, Digital Instruments, Inc., Santa Barbara, CA) equipped with a JV type piezo scanner, a phase detection Extender Module and Nanoscope IIIa controller, and a CO₂/CO laser source. The cantilever tip oscillates in the tapping mode (normal to the surface of the sample) and the back-scattered light is collected at harmonics of the frequency of the cantilever oscillation.

CO₂/CO Laser Emission

The experiments can be conducted with the laser power as low as 50 mW. As the power falls dramatically at the low wavenumbers, it is essential to use the high grade (5.0) gas mixture and occasionally refresh it by evacuating the tube down to the pressures of about 10^{-7} Torr or below. The vacuum manifold should have a liquid nitrogen trap preventing oil from going into the tube. Cooling the tube below -10°C significantly increases the output power, especially for the low wavenumbers. It allows us to make meaningful measurements at the wavenumbers as low as 1750 cm^{-1} and possibly 1650 cm^{-1} . The calibration of the grating drive is done by recording the peak power values in the entire range and comparing it to the literature data. CO laser emission lines are typically separated by 4 cm^{-1} , which limits to some extent the spectral resolution of the method. This can be a significant drawback in identifying the sharp resonance lines.

a. CO₂/CO rebuilt laser

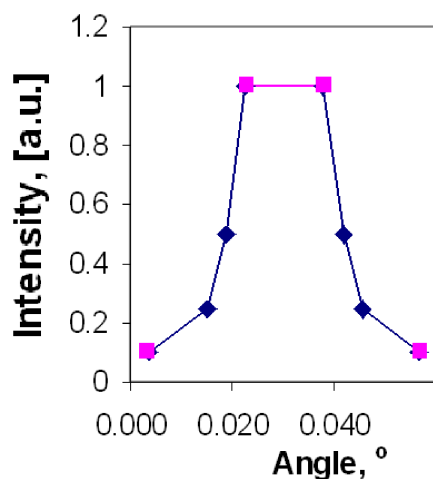


Figure 25. Horizontal (blue) and vertical (magenta) beam expansion of the CO₂/CO laser.

For the first part of the near-field studies, we used a CO laser with the CO₂ tube rebuilt by the original manufacturer Laser Engineering (A Division of PLC Medical Systems) and the BRC-30-25-STD Voltronics' power supply. An output coupler was replaced with a ZnSe Brewster window, external to the cavity optics. The laser beam is expanding within 0.01° (Figure 25), both horizontally (blue line) and vertically (magenta), and can be considered as a parallel beam in simulations. The linearity of the grating drive has also been verified versus the angles of the beam's horizontal and vertical rotation.

b. Commercial laser system

The second part of the near-field work was performed with CO tunable laser from Edinburgh Instruments. The quartz discharge tube of the laser is terminated by stainless steel flanges with copper

gasket vacuum seals providing high vacuum integrity for extended period sealed-off operation. We used a vacuum manifold for refreshing the gas mixture in the tube, which was rebuilt at the University of Pittsburgh (Figure 26). The system was evacuated down to $4\text{-}5\cdot 10^{-8}$ Torr and baked at 150°C for 24 hours prior to refill. Refill pressure was 28 Torr according to the readout of MKS (capacitance-type membrane) gauge. The manufacturer specified CO gas mixture used to replenish the system was as follows: 7% CO (99.95% grade, $\text{H}_2\text{O} < 25$ vpm), 18% N_2 (99.999%), and the balance He (99.999%).

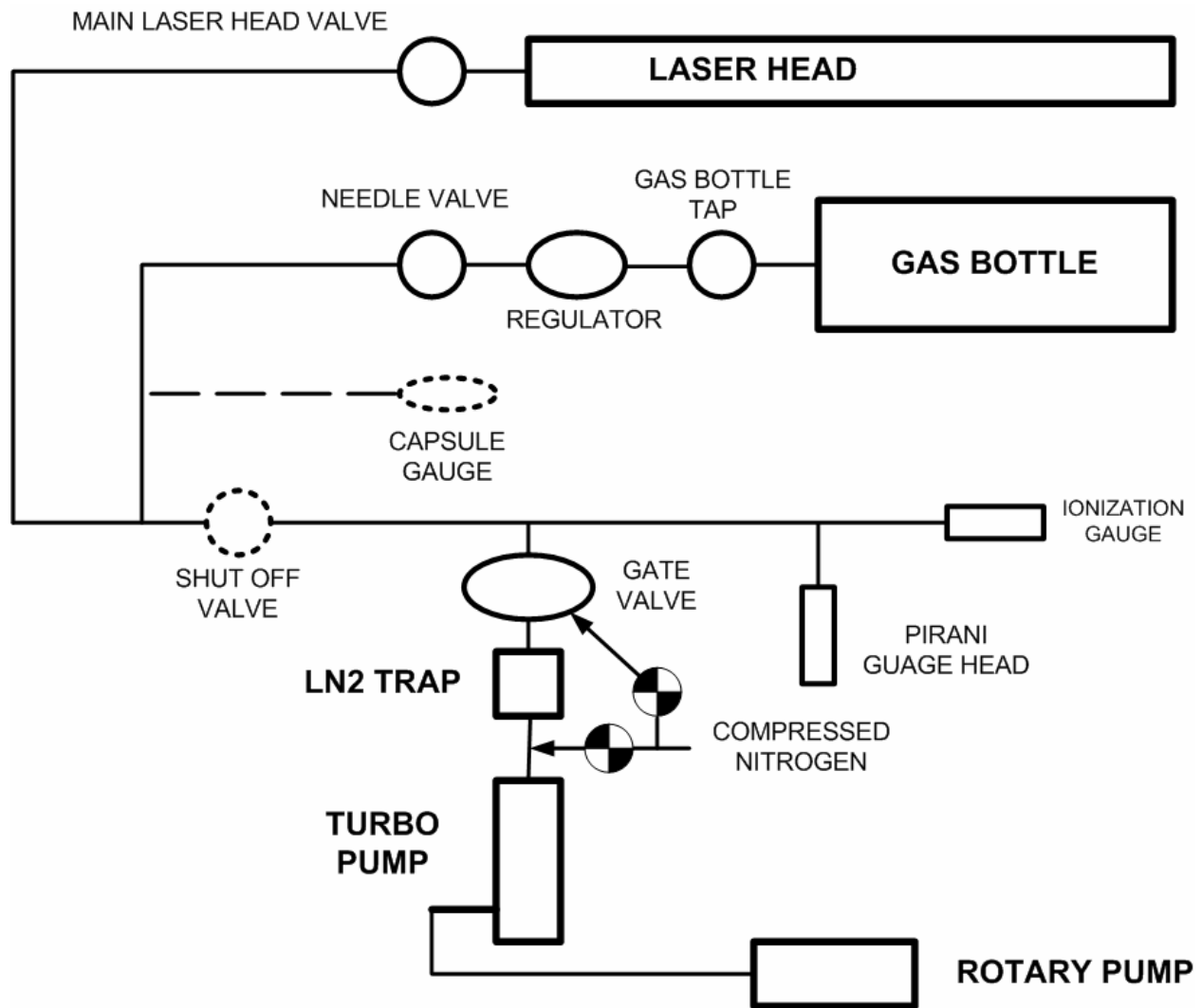


Figure 26. High vacuum manifold.

The optical elements of the laser are stably mounted within granite end blocks spaced by a four rod invar frame. The high efficiency grating is held on an intra-vacuum gimbal pivoted mount with line selection achieved via a manual differential micrometer control. The factory calibration was used to identify the emission lines by the readings of the micrometer.

Comparison of the spectra recorded for the home-built laser and the reference spectrum of the Edinburgh Instruments showed that the pattern of the observed lines depends on the pressure, temperature, and impurities content (Figure 27).

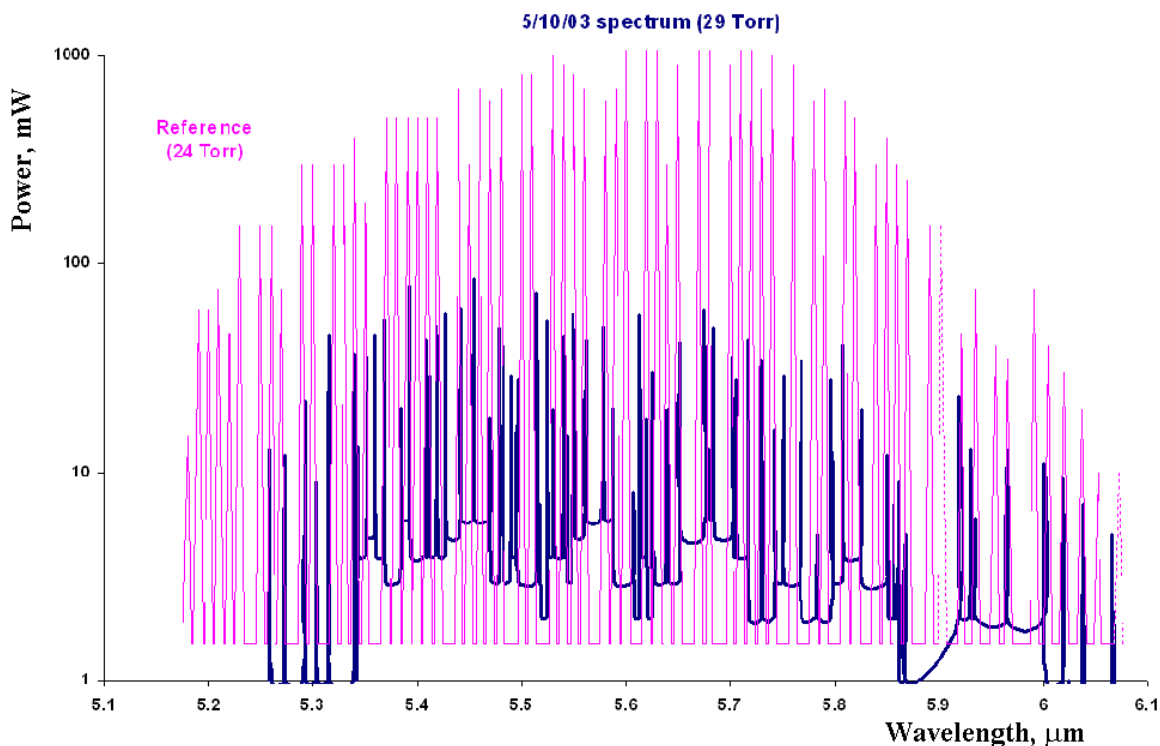


Figure 27. Comparison of two CO lasers (Edinburgh Instruments data are used as a reference). The lasing spectra can differ depending on pressure and impurities content.

The lines can change intensity or even shift over time (Figure 28). Exact vibrational-rotational identification of the emission lines is complicated by the fact that frequencies of some emission lines with different rotational excitation can overlap for transitions between two or more pairs of vibrational levels. Typical line separation is about 4.2 cm^{-1} due to promotion to the next rotational level.

Consistently, the highest intensity lines were 1834.6 cm^{-1} for 10 to 9 transition (19^{th} excited rotational level), 1855.5 cm^{-1} for 9 to 8 transition (20^{th} rotational level), and 1813.8 cm^{-1} for 11 to 10 transition (18^{th} rotational level).

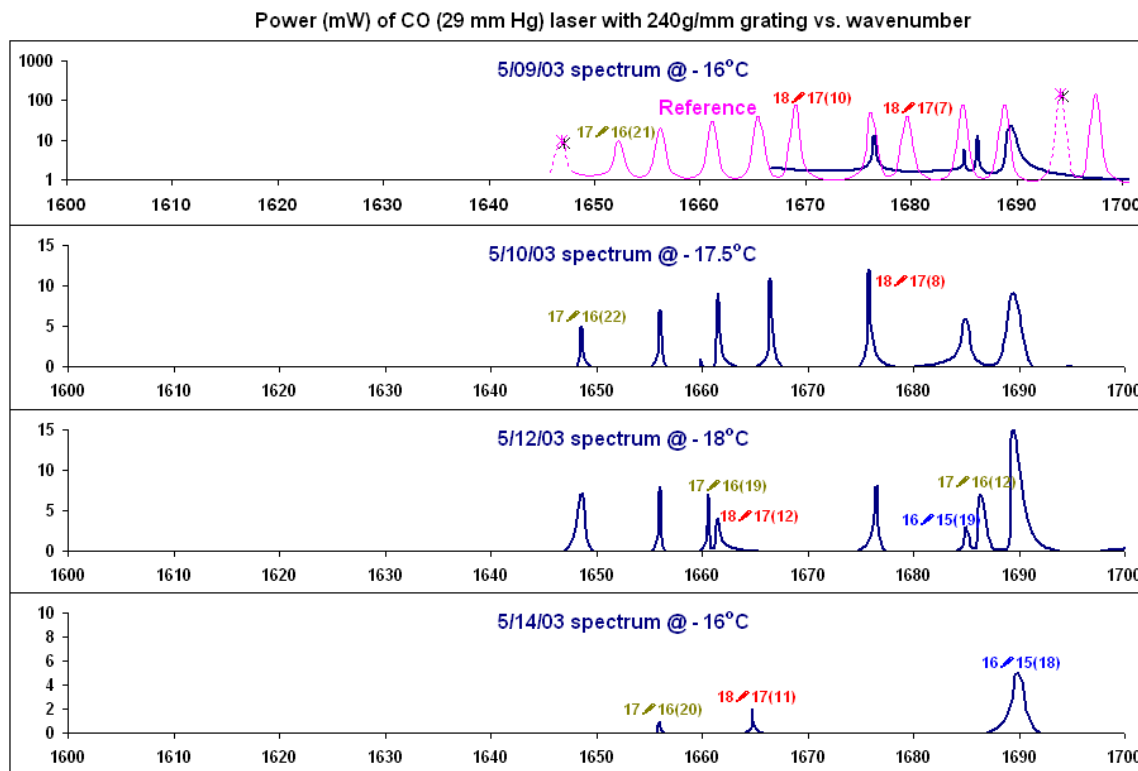


Figure 28. Comparison of two CO lasers. The lasing spectra can change over time, after several days since the last gas replenishment. Corresponding vibrational transitions (and excited rotational levels) were identified by the best fit to the vibro-rotational grid of CO molecule.

Near Field Optical Setup

The infrared light emitted by the carbon monoxide laser was focused by a parabolic mirror onto the end of the platinum-coated silicon nitride cantilever, which is perpendicular to the long axis of the probe (Figure 29). We used *p*-polarized laser beam with $75^\circ \pm 5^\circ$ angles of incidence. The beam stop in a center of the laser beam is designed to minimize the interference from the background scattering.

The sample's position is modulated by the microscope's piezo scanner. Mikromash (Estonia) silicon nitride cantilevers, coated with 25 nm layer of platinum, were used as a probe. Manufacturer specifications for a typical probe are length $130\ \mu\text{m}$, width $35\ \mu\text{m}$, resonance frequency 150 kHz, and

the tip's radius of curvature 35 nm. The cantilever oscillation is amplified by the microscope's optical lever and the resultant photodiode deflection signal is processed by the controller. The AFM software registers the amplitude signal, typically 70-300 nm.

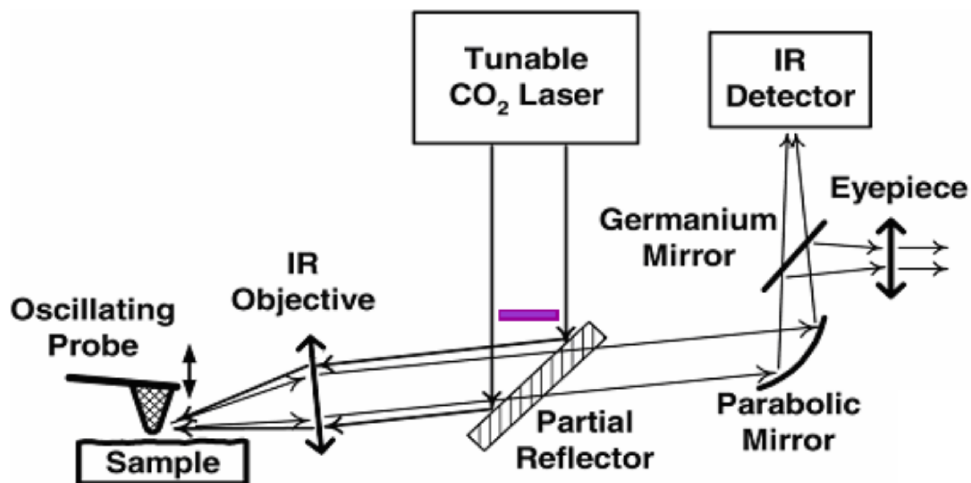


Figure 29. Schematic representation of the apertureless near-field infrared microscope.

Imaging of the sample's surface in intermittent-contact (tapping) mode was performed simultaneously with detection of the scattered infrared signal. The collected scattered light was focused onto a MCT detector (Graseby Infrared, Orlando, FL). The electrical signal from the detector was amplified by a lock-in amplifier, SR844 (Stanford Research Systems, Sunnyvale, CA) at the frequency of the cantilever oscillation and then processed by computer, simultaneously with AFM data. The dc component of the detected signal was observed on the oscilloscope.

COLLECTION OF NEAR FIELD DATA

Introduction

Apertureless near field scanning IR microscopy has been developed for nanometer scale chemical imaging.¹²³ To obtain the signal contrast, an IR laser is tuned to the wavelengths that are characteristic of the stretching vibrations of the investigated organic molecules.¹²⁴ The focus of this study is the bridging carbonyl vibrational resonance of di-iron nonacarbonyl. Tri- μ -carbonyl(hexacarbonyl)di-iron(0), $\text{Fe}_2(\text{CO})_9$, has been previously investigated for its interesting photochemistry.^{105, 106} This molecule can be used as a model for spectral properties of much larger organometallic systems. The importance of understanding the vibrational properties of CO bound to the heme iron was underscored by the recently discovered large electrochromic band shift due to local electrostatic interactions that play a significant role in protein folding and assembly.¹⁰⁷

Experimental Procedure

Figure 30 shows the optical scheme of the ANSIM instrument.

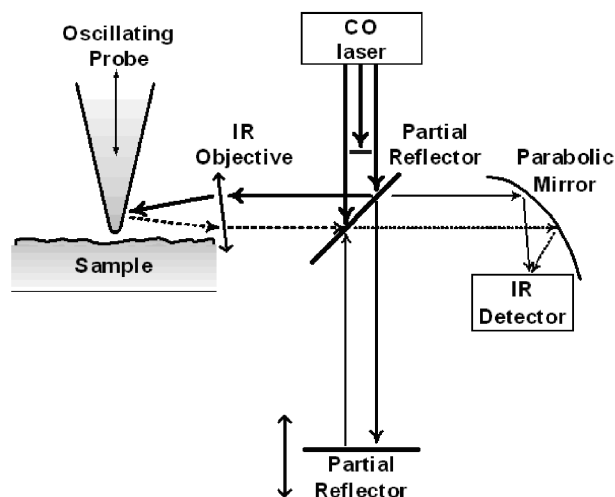


Figure 30. ANSIM apparatus with homodyning option.

Experiments have been done with molecular excitations by IR laser with CO_2 and then CO gas mixtures. CO laser was also used as a broad band source to probe the $\text{Fe}_2(\text{CO})_9$ absorption band at $\sim 1826 \text{ cm}^{-1}$.

Reducing interferometric contribution: Signal detection at $2f$

In order to minimize the interference of the scattered IR beams, the signal is often modulated at twice the frequency of the cantilever oscillation.

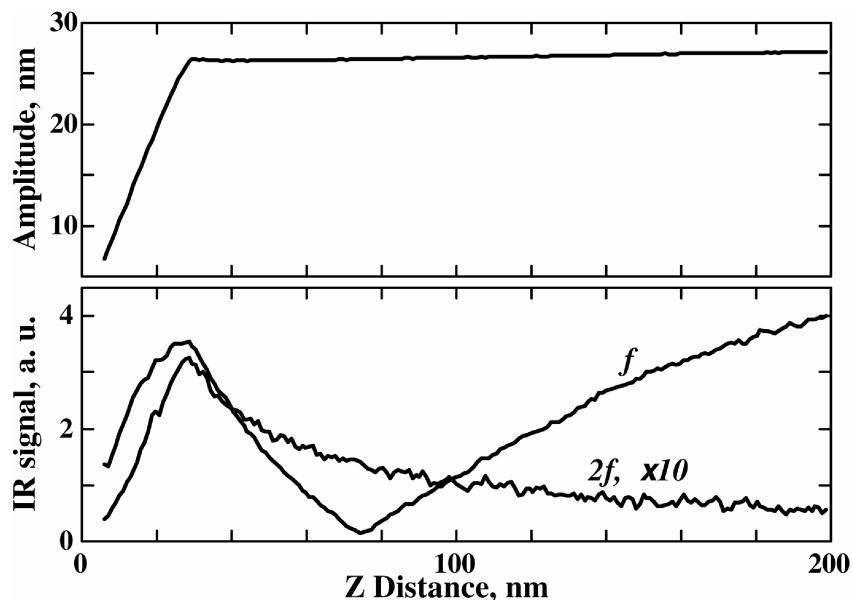


Figure 31. z-dependence of the amplitude of cantilever oscillation (top panel) and the first and second harmonic near-field signal (bottom panel). The interferometric feature present in the f -signal is missing from the $2f$ -signal. ^{125, 126}

- Probe oscillation upon approach toward the surface remains harmonic.
- Thus, the presence of the second harmonic in the scattered signal indicates strong non-linearity in the near-field signal upon approach to the surface.

The underlying assumption of the above arguments in favor of the second harmonic detection is that the contribution of direct scattering of the beam by the cantilever body and surface irregularities almost linearly depends on the tip-sample separation. Hence the second and higher harmonics contribution of the background scattering is relatively low.

Typical first harmonic z-plots above ultra-flat gold surface can look similar to the second harmonic z-plots (Figure 32). Usually, these shapes are interpreted as an indication that the optics is aligned and focused correctly. However, more careful investigation shows that the nature of the signal strongly

depends on the sample surface that is scanned over. While over the ultra-flat gold surface even the first harmonic looks like a “true” near field, the proximity of the absorbing surface, e. g. di-iron nonacarbonyl, can make the second harmonic signal appear worse than the first harmonic.

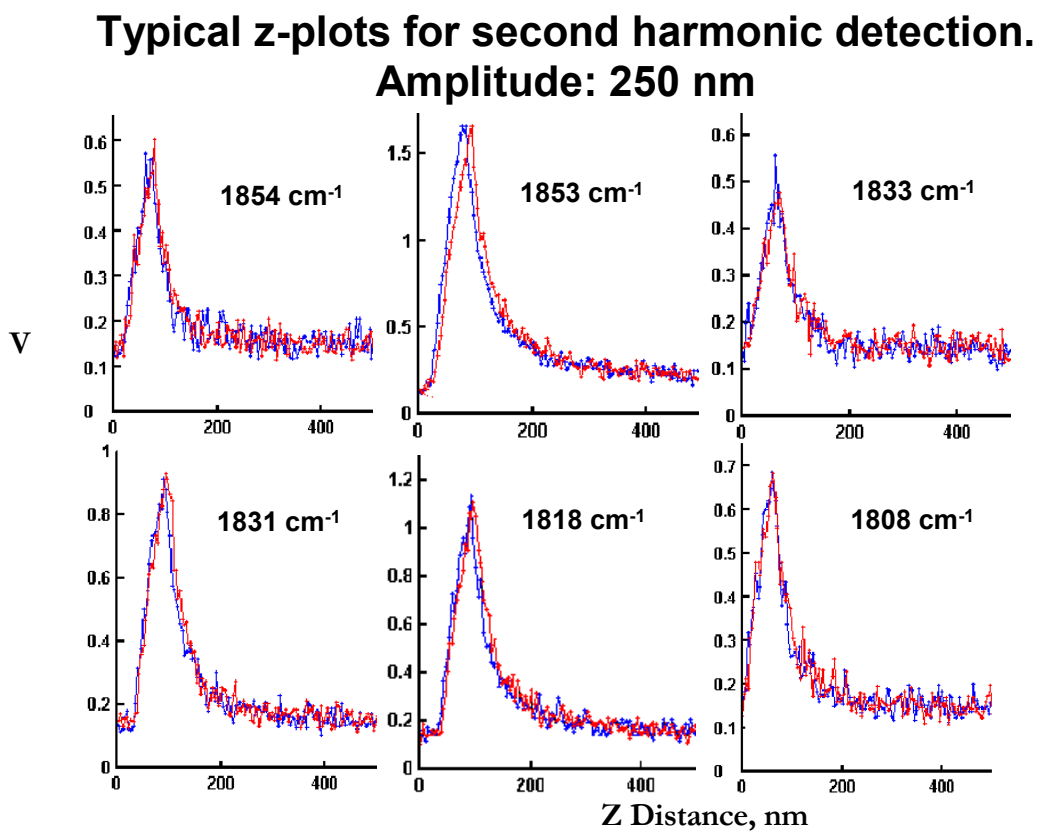


Figure 32. Typical second harmonic z-plots, signal (V) as a function of the vertical displacement (nm) above the gold surface for different wavelengths. The peak signal is proportional to the laser output power but the baseline does not change.

The z-dependence of the signal above the surface of a sample particle can be significantly different for both first and second harmonic detection, even for relatively flat particles (Figure 33).

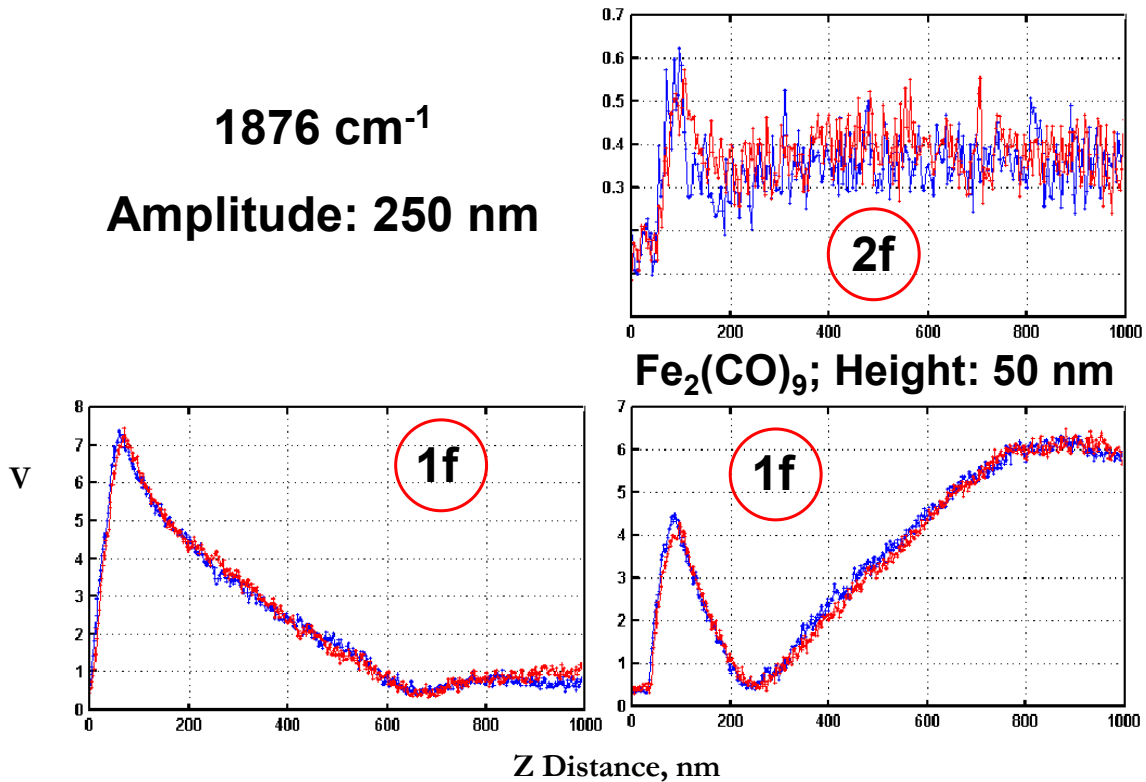


Figure 33. First and second harmonic z-plots (nm) of IR near field signal (V), at 1876 cm⁻¹ and the amplitude of cantilever oscillation of 250 nm. Lateral dimensions of a particle: $\sim 0.5 \times 1.0 \mu\text{m}$, the height is 50 nm. While both first (bottom right) and second harmonic (top) plots show interferometric features above the Fe₂(CO)₉ flake, the first harmonic z-plot above the gold surface near the particle (left) is very similar to z-plots away from any particles.

Signal-to-noise detection limit

Additionally, the intensity of the second harmonic signal is relatively low, which complicates the quantitative analysis of scattering amplitude versus wavenumber (see Figure 34).

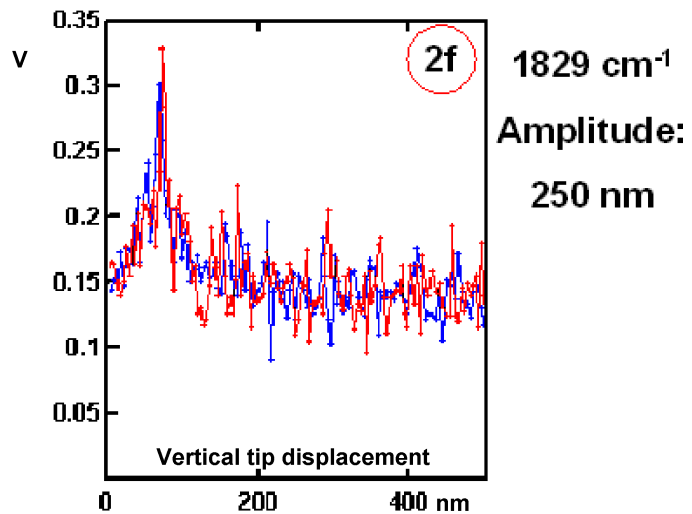


Figure 34. Second harmonic near-field signal at 1829 cm⁻¹. Signal-to-noise ratio is much lower than at the first harmonic frequency.

Homodyne reference for signal amplification

Detection of the weak scattered field is enhanced by homodyning. The idea behind this enhancement is usually simplified as follows. Since the total intensity of the infrared radiation incident upon a detector equals the square of the sum of two electromagnetic waves, it has three main terms, including the term proportional to the product of two amplitudes:

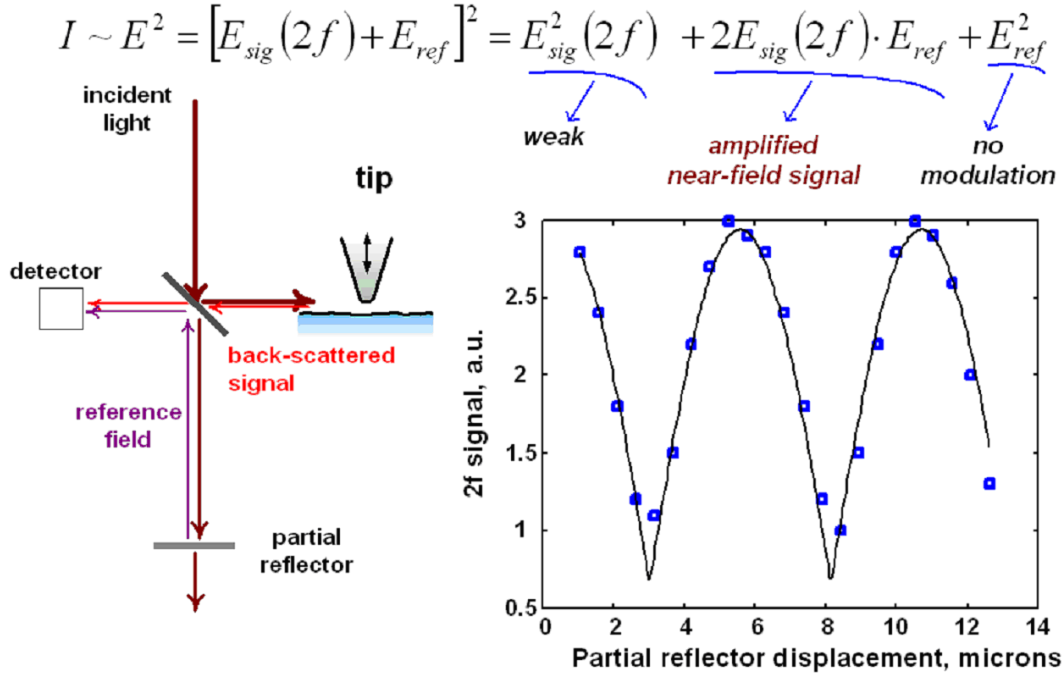


Figure 35. Dependence of the near-field signal on displacement of the partial reflector. ¹²³

It has been reported that lock-in detection results in a signal that is proportional to the absolute value of cosine of the phase shift between the reference and scattered beams (Figure 35), which was shown to be in agreement with a Fourier series truncated at the second harmonic. ¹²³ Generally, this is not the case however, because the temporal shape of the scattered near-field signal can be approximated by a rectangular wave whose duty cycle depends on the amplitude and the setpoint of the cantilever oscillation. In the simplest case of a squarewave signal, $V_{sw}(t)$ the second harmonic is absent:

$$V_{sw}(t) = \frac{4}{\pi} \sin \omega t + \frac{4}{3\pi} \sin 3\omega t + \frac{4}{5\pi} \sin 5\omega t \dots$$

If the intensity of the near-field scattering is modulated by an arbitrary periodic function $f_{\Omega}(t) = f_{\Omega}(t+2\pi n/\Omega)$ and the reference of the lock-in amplifier is proportional to $\cos(m\Omega t + \theta)$, the power incident at the detector is

$$\frac{1}{2}EE^* = \frac{1}{2} \left\{ A e^{-i\omega t} + e^{-i(\omega t + \varphi)} \cdot [1 + f_{\Omega}(t)] \right\} \cdot \left\{ A e^{i\omega t} + e^{i(\omega t + \varphi)} \cdot [1 + f_{\Omega}(t)] \right\} \quad (7)$$

and the demodulated signal equals

$$V = \oint_{2\pi/\Omega} \left\langle \left[\frac{1}{2} f_{\Omega}^2(t) + f_{\Omega}(t) + A \cdot f_{\Omega}(t) \cdot \cos \varphi \right] \otimes F(t, \tau) \right\rangle \cdot \cos(m\Omega \tau + \theta) \cdot d\tau. \quad (8)$$

Here A is an enhancement factor for the homodyne reference beam; $F(t, \tau)$ is the instrument convolution function that is determined by detection bandwidth, Δf . For very weak near-field scattering with non-negligible m -th harmonic Fourier component of the $f_{\Omega}(t)$ convolution, compared to that of $f_{\Omega}^2(t)$, maximum enhancement of the signal in case of a very fast detector ($\Delta f \gg \Omega$) can be estimated as follows

$$V = A \cdot \oint_{2\pi/\Omega} f_{\Omega}(t) \cdot \cos(m\Omega \tau + \theta) \cdot d\tau. \quad (9)$$

The homodyned first harmonic allows collecting high quality near field signal by scanning very close to the sample surface, at low tapping amplitude. The observed signal profile was similar to the second harmonic z -plots (Figure 36).

Both for the first harmonic single wavelength and the second harmonic broadband source, the contrast appears to be the same regardless of the particle height or lateral dimensions. Yet it begins to fade dramatically for thicknesses around 3 nm to 5 nm. This effect is further investigated in the next chapter. The limit of applicability of semi-infinite space approximation is estimated to be around 50 nm. The height of the particles selected for spectral analysis was 50 nm to 100 nm. The sub-micron-sized solid flat (mica type) flakes of $\text{Fe}_2(\text{CO})_9$ (Aldrich, 99.5% pure) were physisorbed onto the gold-coated (200 nm) substrate and then analyzed by using the ANSIM apparatus that collected the back-scattered electromagnetic response of the cantilever tip-surface structure. It was observed that the near

field reflectance of thinner flakes strongly depends on their height. It was also observed that gold reflectance between the particles can be anomalously high between the adjacent particles, even at the second harmonic detection (Figure 37).

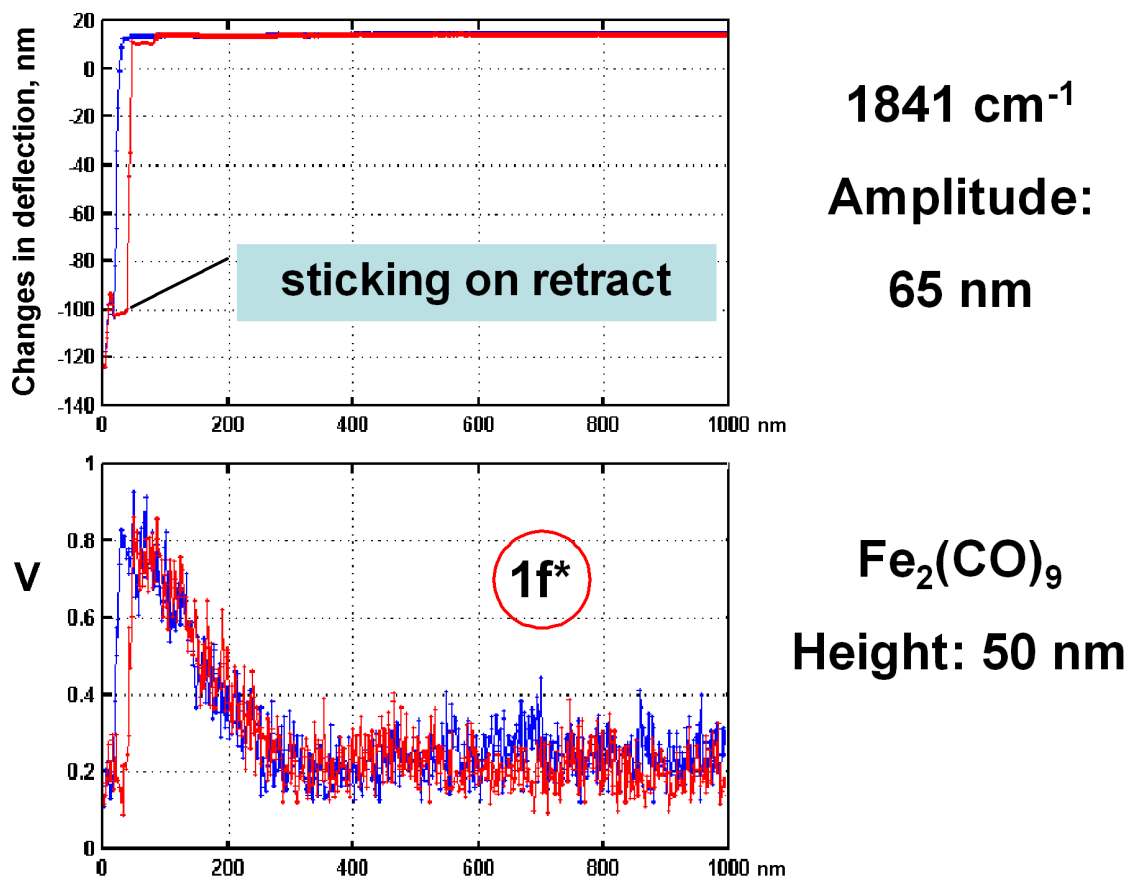


Figure 36. z-dependence of the homodyned first harmonic near-field signal (bottom) and the corresponding changes in the cantilever's peak-to-peak deflections.

Section Analysis of near field signal

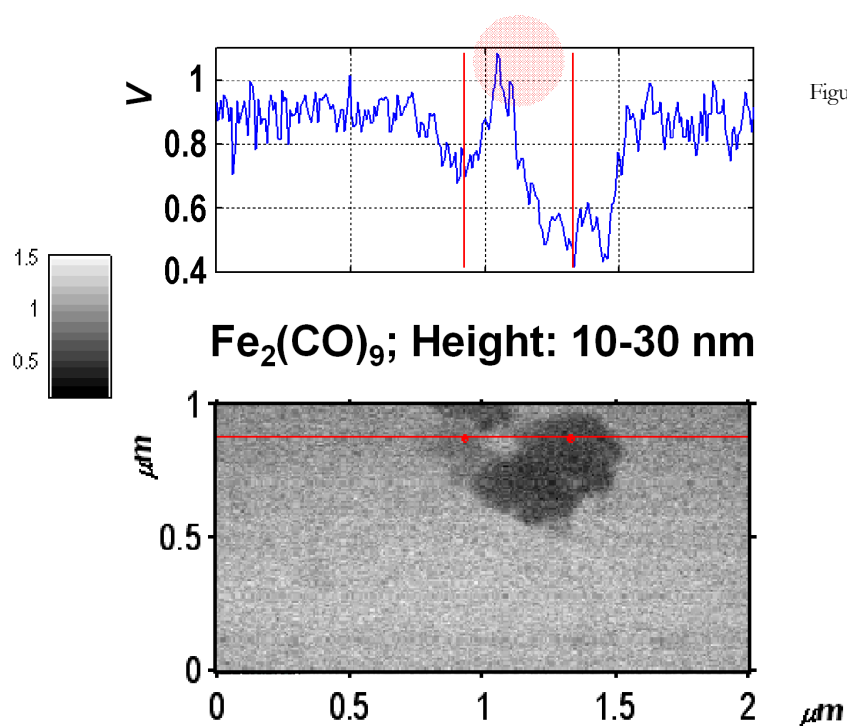


Figure 37. Multi-particle edge effect (the second harmonic detection): anomalously high scattering is observed between the adjacent absorbing particles.

Broadband detection

While single wavelength excitation allowed us to collect reproducible tapping mode scans, the use of a broad band source resulted in time dependence of the scattering signal:

k, cm ⁻¹	Power, mW	Persistency
1814	8	35%
1835	35	74%
1856	29	29%
1881	33	34%

The typical time scale for significant changes in power distribution among these lines was observed to be about half an hour (Figure 38).

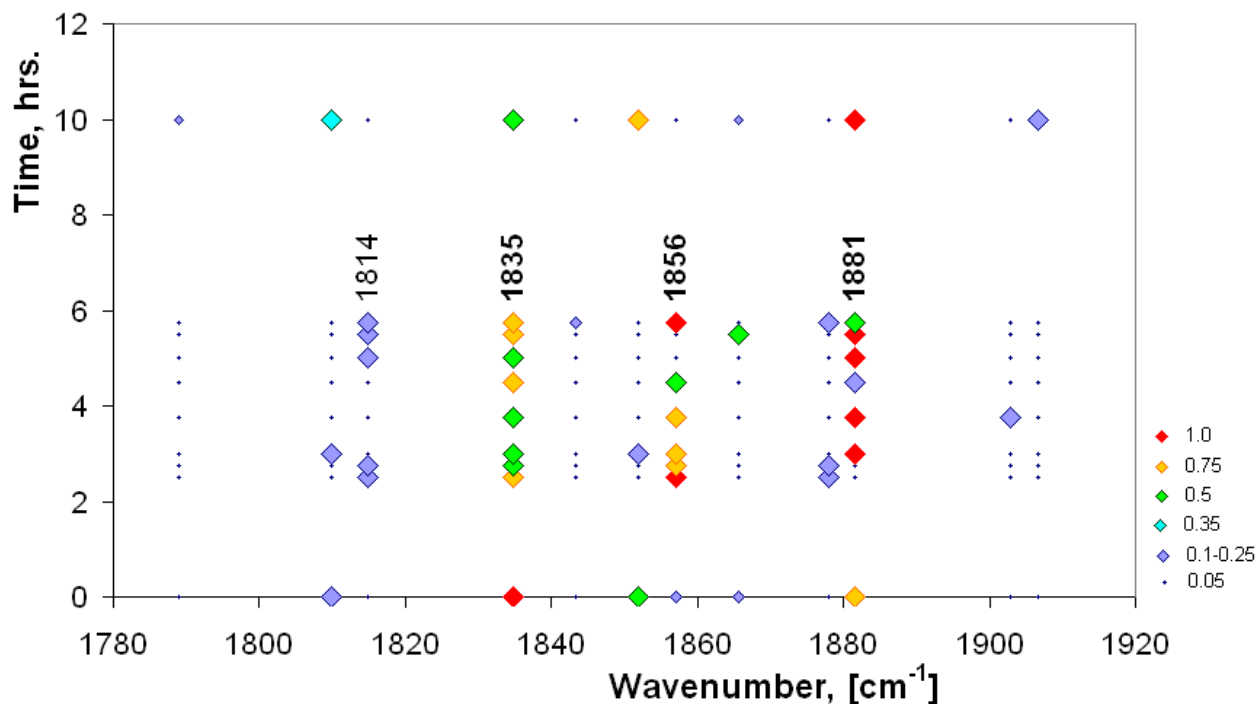


Figure 38. Broadband CO laser modes beating diagram. The color map (right margin) indicates the relative intensities of the emitting lines during the measurements.

The AFM images in Figure 39 show the instability of the IR scattering pattern over time while the focus and other relevant parameter of the apparatus remain constant. The image features due to iron carbonyl particles on gold surface changed from absorption to diffuse scattering (possibly, topographic artifacts) or a mix of those. The changes occurred on the time scale of several minutes to an hour. Similar changes can be induced by adjustment of the focal settings. As Figure 40 shows, that causes appearance of secondary and even tertiary peaks in z-dependence (along the vertical axis of tip-sample separation) of IR signal. The typical plot should have just one peak as in Figure 41 for tunable CO₂ laser. The near-field signal increases with the increase of amplitude but only one peak is observed along the tip-sample separation axis.

The multi-peak anomaly is attributed primarily to CO laser power beating at three major lines: around 1835 cm⁻¹ (corresponding to iron carbonyl absorption band), 1856 cm⁻¹ and 1881 cm⁻¹. The other plausible sources of multiple peaks are spatial modes and strong interference with the scattered light (self-homodyning). The force mode measurements have been made on a flat gold surface, a few micrometers away from large scattering objects. However, it is possible that there was some scattering from nearby less prominent surface features. In order to investigate the near-field effects induced by a

broadband source, the issue of stability of simultaneous oscillation on several transitions¹²⁷ should be addressed.

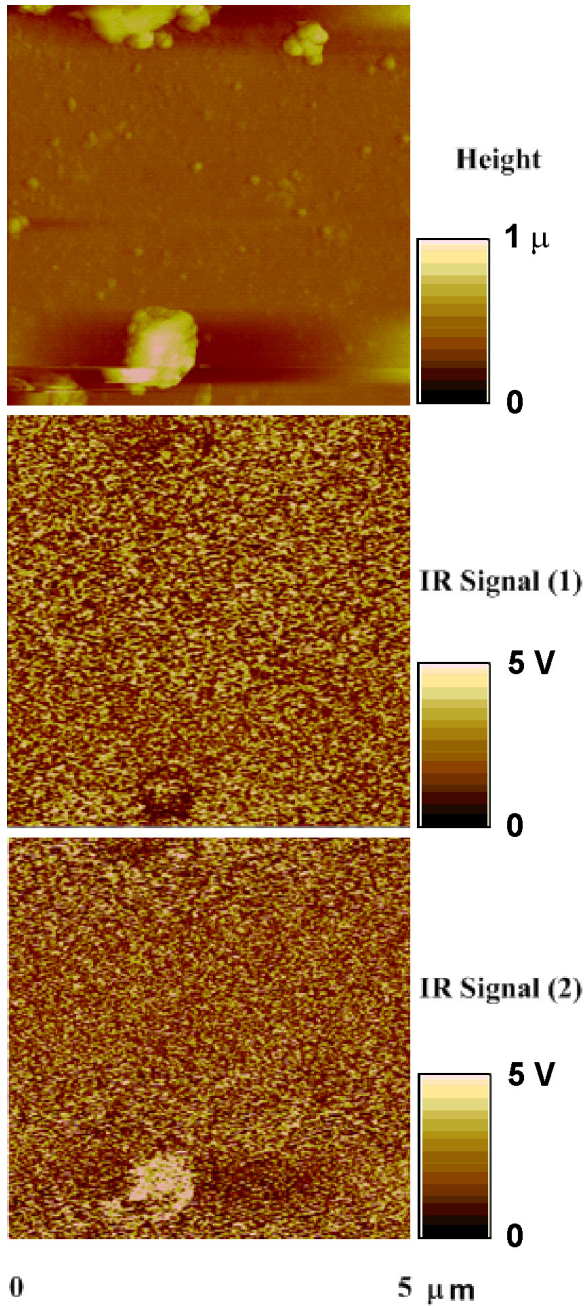


Figure 39. The infrared near-field signal changes over time: absorption (1) and diffuse scattering or topographic artifacts (2).

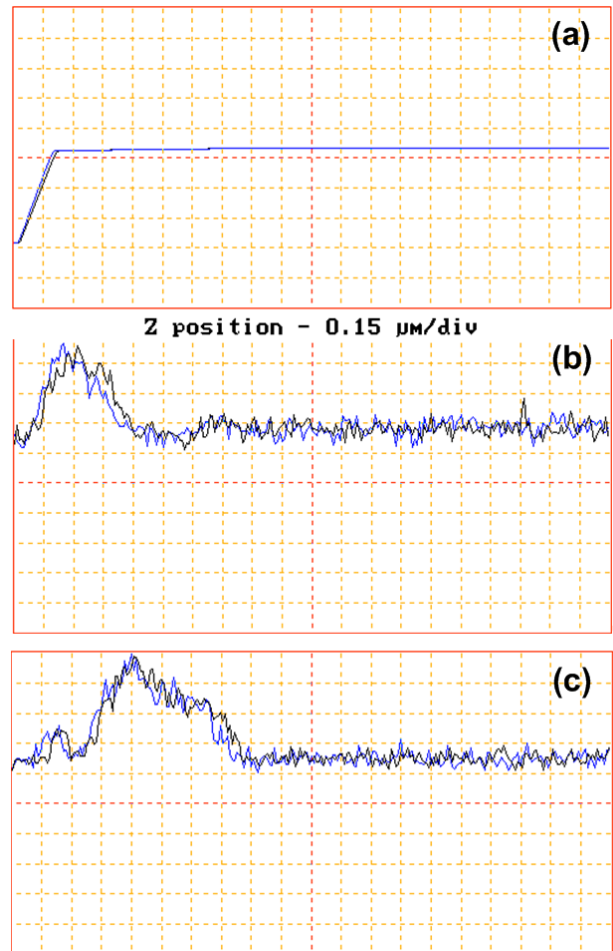


Figure 40. AFM Force Mode: Amplitude (a); IR Signal spatial decay at focal position #1 (b); IR Signal spatial decay at focal position #2 (c) – this unusual z-dependence of a signal can be attributed to multi-wavelength detection or the background scattering interference.

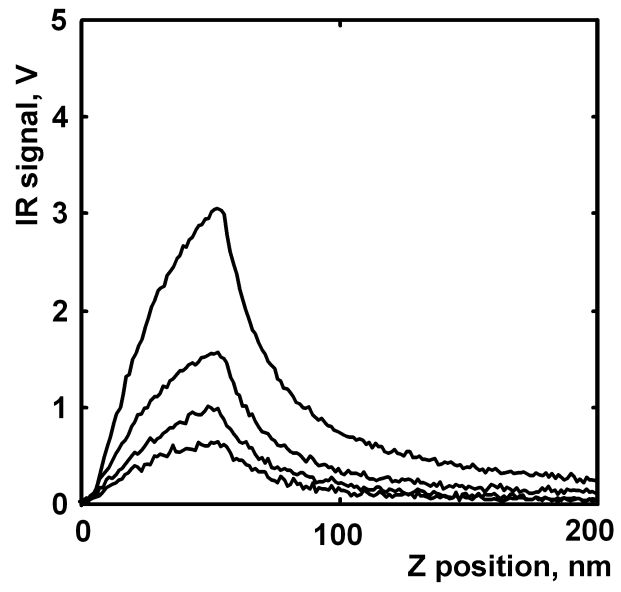


Figure 41. Typical signal at different amplitudes.

THEORETICAL MODELS AND ANALYSIS OF THE NEAR FIELD DATA

Light scattering by particles on a surface has been a focus of many theoretical studies. For practical applications, the calculation of light scattering from particles and nanostructures on a surface is of interest in calibration of near field instruments. For effective exploitation and advancement of the ANSIM technique, we need a quantifiable model for analysis of the collected signal. The inherent difficulty in the calculations compared to light scattering by spherical particles is that once the surface is added the spherical symmetry is broken and the expansion in spherical vector harmonics (Lorenz-Mie)¹²⁸ cannot account for the particle-surface interaction. A number of studies have addressed this problem by the use of widely differing methods.¹²⁹⁻¹³⁴

The formal Sommerfeld solution is time consuming, because it involves a numerical integration for each field evaluation.¹³⁵ The quasi-electrostatic image dipole approximation has been recently proposed as an analytical model for calculation of the forward scattered signal in apertureless near-field optical microscopy.^{4, 126, 136} (This is a reasonable estimate for metallic substrates with large real part of refractive index.) A more recent work,¹³⁷ attempting to predict the back-scattered signal dependence on imaging conditions, used a theoretical model that treats the substrate and the sample as a perfect conductor coated with very thin absorptive layer.

The coupled-dipole method was originally developed to compute light scattering from particles in free space. The solution to a dipole above a conducting ground was first considered by Sommerfeld¹³⁸ and later by Weyl¹³⁹ and has been of steady interest because of its application to antennas and radars.¹⁴⁰⁻¹⁴⁴

The related question of power absorbed in the lossy half space was presented by Sommerfeld and Renner in 1942.¹³⁵ Nevertheless, fundamental issues related to the vertical component of the interfacial current (coined as “E-field loss”)¹⁴⁵ have not been resolved. In some recent publications, several authors questioned the accuracy of various approximations, such as the image dipole with or without surface wave term and the quasi-static solution, in evaluating the near zone (field points close to the dipole) axial electric field.¹⁴⁵⁻¹⁵²

Taubenblatt and Tran¹²⁹ compared the results obtained by the finite-element solution to Maxwell's equations¹³⁰ and by using the full Sommerfeld calculation with those that they obtained using the image dipole method modified by the appropriate Fresnel reflection coefficient. For a spherical polystyrene particle with 300 nm diameter on silicon (the refractive index used was $3.85 + 0.018i$), they found that the approximate image dipole is in a good agreement with exact (Sommerfeld) calculations for forward scattering (the angle of incidence was 65°), but its estimates for back-scattered p-polarized light are slightly off, approximately by a factor of 1.5. For the particles that were very close to the surface, the reflection terms resembled those that are due to a static dipole above a dielectric half-plane. Overall, the Fresnel reflection method works well for an observation point far from the surface; a perfectly conducting substrate is well approximated by an image dipole.

In this work, we compare the application of the simplified coupled-dipole model and the NEC2¹⁵³⁻¹⁵⁵ plane-wave reflection method to the analysis of experimental data for near field scattering by iron carbonyl particles on gold surface.¹⁵⁶ Traditionally, near field of the tip-sample interaction is modeled by effective polarizability that is derived as a solution of an infinite series of instant electric fields induced by the incident plane wave, a dipole moment of the tip (regarded as a sphere to simplify calculations) and its mirror image in the sample. This model has proved itself useful for interpreting experimental data for relative intensity of the near field scattering by materials with almost flat frequency dispersion of the dielectric function, especially metals.

Coupled dipoles model for z-dependence of registered IR signal

Traditionally, the ANSIM relative near-field contrasts are described by the coupled-dipole model.¹⁵⁷ In the static dipole approximation,⁴ the near-field interaction of an incident p-polarized plane electromagnetic wave with the sample (half space characterized by the complex dielectric constant ϵ_s) and the AFM cantilever tip with the radius of curvature a and the coating characterized by the dielectric constant ϵ_t at a distance z from the sample's surface is governed by the effective polarizability of

$$\alpha_{eff} = \frac{\alpha(1 + \beta)}{1 - \frac{\alpha\beta}{16\pi(a + z)^3}}, \quad (10)$$

where α and β are polarizability of a sphere and its mirror image respectively ($p = \alpha E$, $p' = \pm \beta p$):

$$\alpha = 4\pi a^3 \frac{\varepsilon_t - 1}{\varepsilon_t + 2}, \quad (11)$$

$$\beta = \frac{\varepsilon_s - 1}{\varepsilon_s + 1}, \quad (12)$$

ε_t is a dielectric constant of the cantilever tip, ε_s is a dielectric constant of the sample, a is the tip's radius of curvature, and z is the tip-sample separation.

Unlike the forward scattering setup,⁴ where the total extinction cross-section is detected, we detect the back-scattered light. Thus, assuming the effective medium approximation, the intensity of back-scattered light should be proportional to the scattering cross-section

$$C_{sca} = k^4 \cdot |\alpha_{eff}|^2 / 6\pi. \quad (13)$$

In IR region, the real part of permittivity of metals is very large and the above formula (10) can be simplified to

$$\alpha_{eff} = \frac{8\pi a^3}{1 - \frac{a^3}{4(a+z)^3}} \quad (14)$$

and the intensity of the scattered radiation, which is proportional to the square of the effective polarizability, nonlinearly drops for $z > a$ (Figure 42).

Matlab simulation of the second harmonic scattering signal based on the above model matched the experimental data for gold and silicon relative intensities quite accurately, which allows using it for calibration of the method (Figure 43). However, the quasi-electrostatic condition, $S_{back} \approx S_{forward}$ does not always hold true, especially for metals.

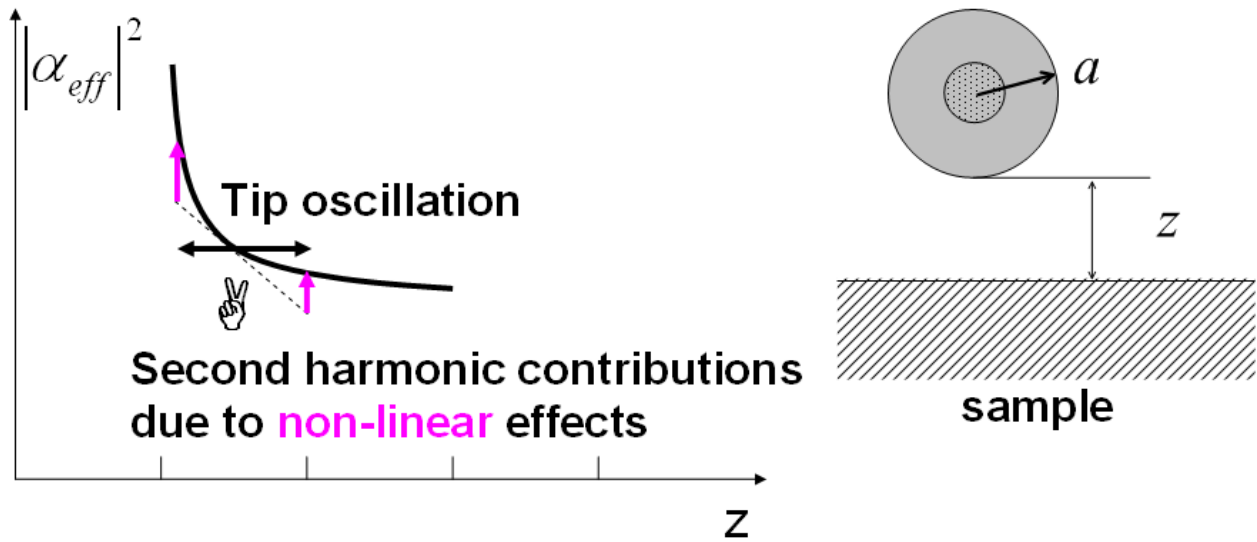


Figure 42. z-dependence of the near field scattering and the origin of the second harmonic signal.

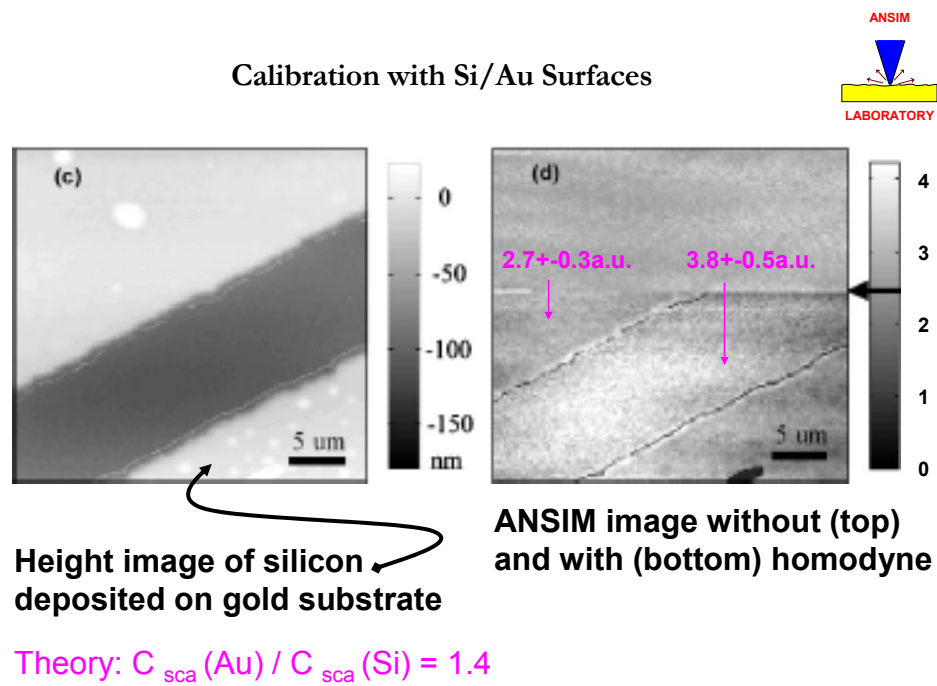
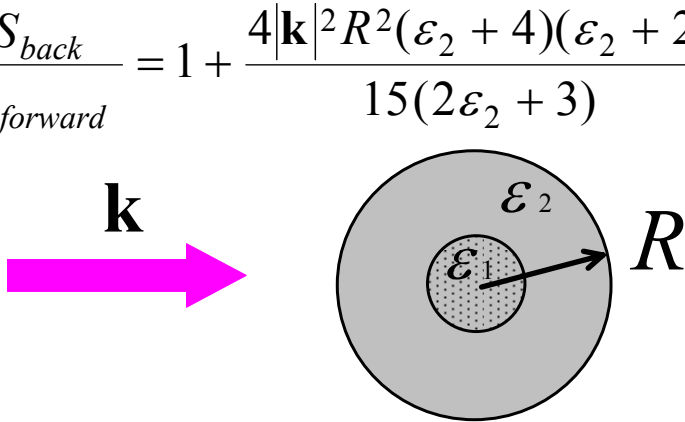


Figure 43. Near field contrast of silicon film deposited on gold surface. The averaged experimental intensities ratio is almost identical to the theoretical predictions of the coupled dipoles model in quasi-static limit.

Quasi-static limit

Formula (11) can be corrected for a coated tip by using effective medium approximation with the fill factor f (Figure 44).

$$\frac{S_{back}}{S_{forward}} = 1 + \frac{4|\mathbf{k}|^2 R^2 (\varepsilon_2 + 4)(\varepsilon_2 + 2)}{15(2\varepsilon_2 + 3)}$$



$f = \frac{R_1^3}{R_2^3}$

$$\alpha = 4\pi a^3 \frac{(\varepsilon_2 - 1)(\varepsilon_1 + 2\varepsilon_2) + f(\varepsilon_1 - \varepsilon_2)(2\varepsilon_2 + 1)}{(\varepsilon_2 + 2)(\varepsilon_1 + 2\varepsilon_2) + 2f(\varepsilon_1 - \varepsilon_2)(\varepsilon_2 - 1)}$$

Figure 44. Polarizability model for a coated tip. Effective medium approximation is applicable if $S_{back} \approx S_{forward}$.

A knowledge of the dielectric functions of the sample and the cantilever tip as a function of frequency permits a prediction of the near-field spectrum. This model has proved itself useful for interpreting experimental data for relative intensity of the near field scattering by materials with almost flat frequency dispersion of the dielectric function, especially metals.

Application of the coupled dipoles model to a single narrow vibrational band shows that the resulting near field spectrum may depend not only on the wavelength of the original peak but also on the absolute value of the oscillator strength and the high frequency refractive index or ε_∞ (Figure 45). Matlab calculations did not show any noticeable effects of the tip coating (whether it is gold, platinum or other good conductor) on near field signal.

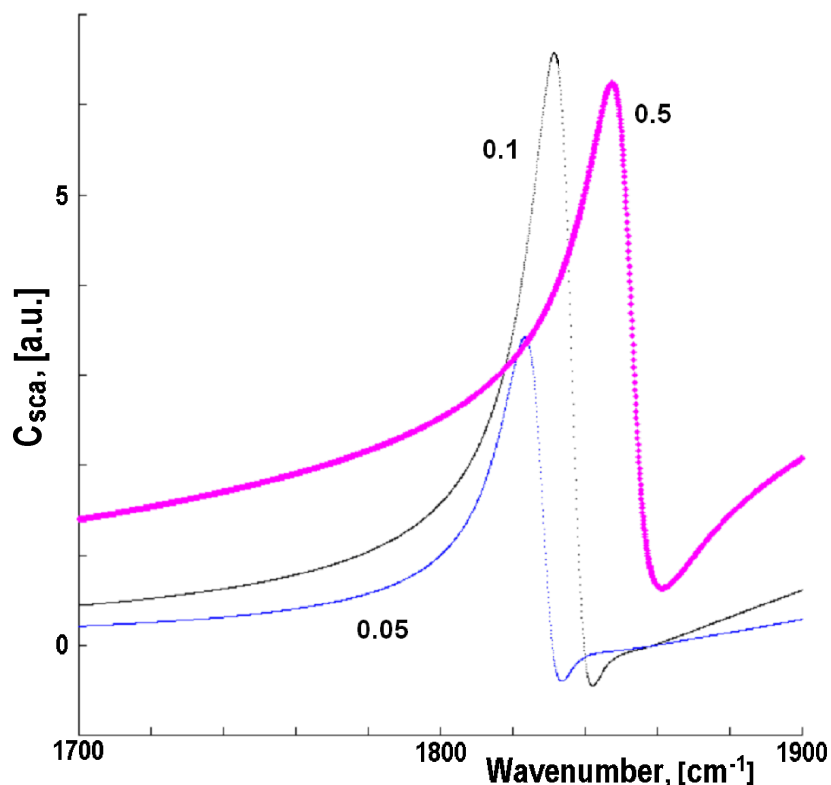


Figure 45. Near field scattering spectrum of a single vibrational mode (1826 cm^{-1}) computed within the coupled dipoles model (Pt tip over iron carbonyl surface). The resonance feature's shift depends on the oscillator strength multiplier (0.05 to 0.5) for a constant ϵ_∞ .

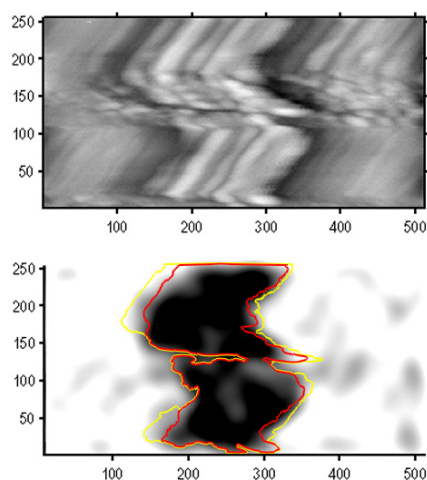
Detection of a Narrow Resonance due to Molecular Vibrations in a Nanoparticle

We collected the iron carbonyl versus gold relative near-field contrast spectra at the second harmonic without homodyning and separately at the first harmonic with homodyning. A broadband IR source was used for comparison. The results will be compared to simple theoretical models for the tip oscillation amplitude of 35 nm.

The spectral resolution was limited by the spacing ($\sim 4\text{ cm}^{-1}$) of the CO laser emission lines. The MCT detector-preamplifier adjustable bandwidth (DC to 5 MHz) was typically adjusted between 500 kHz and 1 MHz for better sensitivity and lower background noise. A phase-sensitive detector of the wide bandwidth lock-in amplifier demodulated (in a fundamental responding mode) the homodyned IR signal at the first harmonic of the tapping frequency of the AFM cantilever, 166-167 kHz. Both

homodyning and the lock-in detection used the phase auto-tune option for signal maximization. The same platinum-coated (25 nm) cantilever tip, with the radius of curvature ~ 35 nm, was used for the entire set of the fitted data. The raw (without flattening) demodulated intensity data were collected from the middle region of the sample particles and then converted from the electric field to the power scale. The background noise was estimated as about 20% of the gold film brightness. We did not notice any IR frequency-dependent variation of the noise level.

Spatial Resolution limits at 1850 cm^{-1}



1 pixel = 1 nm

- ✓ For particle thickness of **3 to 5 nm**, the near field resolution limit is more than 10 nm
- ✓ On edges, 1 to 2 nm, near field and height features do not always match
- ✓ The NF contrast vs. thickness rapidly increases from 1 nm to above 5 nm

The shape of the near field image does not always coincide with the shape of the particle even for the particle thickness of 5 nm and more. This is an indication that the observed signal is not caused by topography coupling. The differences between the two shapes could be due to the hollow structure of the particle or the hidden spaces underneath it. On the other hand, the reproducibility of the finer features can be a measure of the special resolution of the method. The contrast enhanced – by the background removal – near field image of the 5 nm thick particle (Figure 46) accurately shows some features as small as 10 nm, but some other features smaller than 20 nm are not reflected in the image. We can speculate again that this variation in spatial resolution is due to effective thickness of the particle being different from its height. As the thickness becomes smaller than 3 to 5 nm, the spatial resolution dramatically drops and 1 or 2 nm thick edges of the particle do not match the near field image.

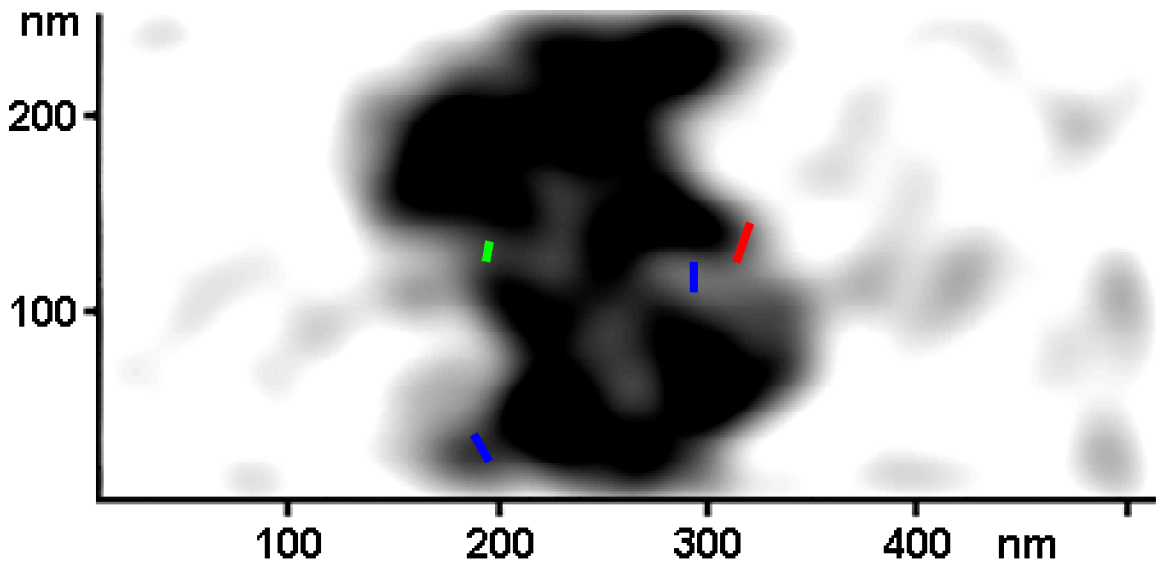


Figure 46. Near field image (1850 cm^{-1} , $500\text{ nm} \times 250\text{ nm}$), spatial resolution: 10 nm (green bar); 15 nm (blue bars); and 20 nm (red bar).

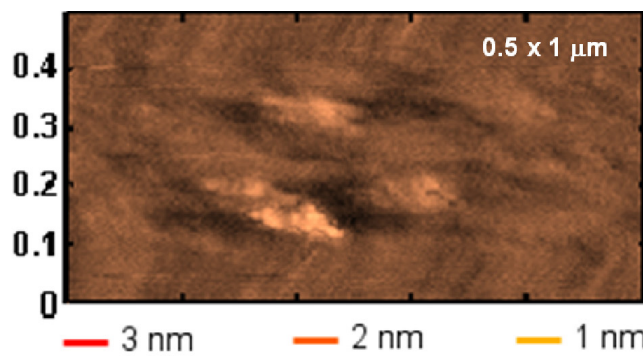
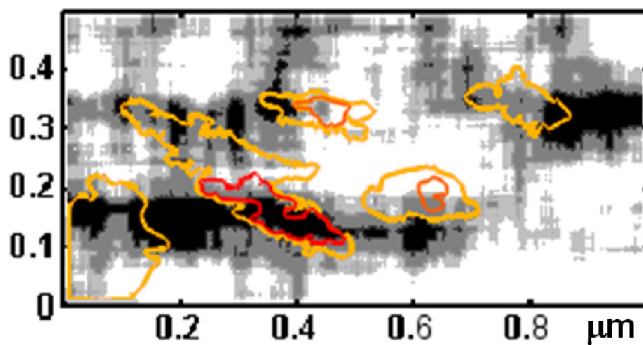
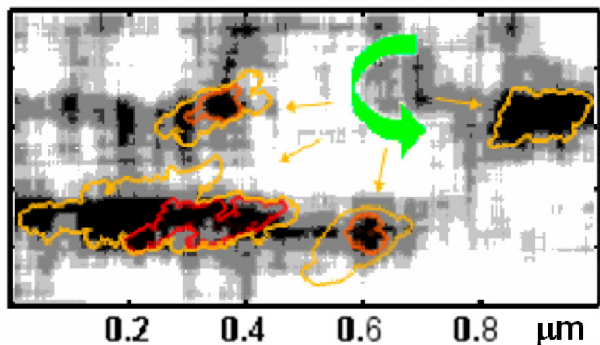


Figure 47. Top: AFM height image. Bottom left: Enhanced contrast (black-and-white) near-field image of the same particles; the contours show the border lines (red = 3nm, orange = 2.5nm, gold = 2nm) of the particles copied from the AFM height image (top). Bottom right: same as the left image but after rotation by 35° and the shift away from the common center. Displaced images are more prominent than near field images at the original particle locations.



Rotation 35° and 50-100 nm off



Detection limit for the thickness of the iron carbonyl flakes was between one and three nanometers. While the lateral spatial resolution for the particles thicker than 4 nm was approaching 10 nm, the thinner particles caused the apparent shift and rotation effects (Figure 47). The enhanced-contrast near-field images of very thin flakes do have some overlap with the physical location of the particles but their highest intensity is observed within 50 nm to 100 nm away. The transposition based on the shape similarity suggests existence of rotational centers in imaging of the extra thin (2 or 3 nm) flakes (Figure 47), possibly due to attractive tip-sample interaction that caused the very light flakes to move and stick to the side of the cantilever. Alternatively, the tip became dull, with more than 100 nm radius of curvature. In this case, it may attract the flakes that are more than 50 nm away from the scanned area because the vertical tip-sample separation is less than 10 nm. The rotation effect could be related to the tip's shape or specifics of the particle's binding site on the substrate.

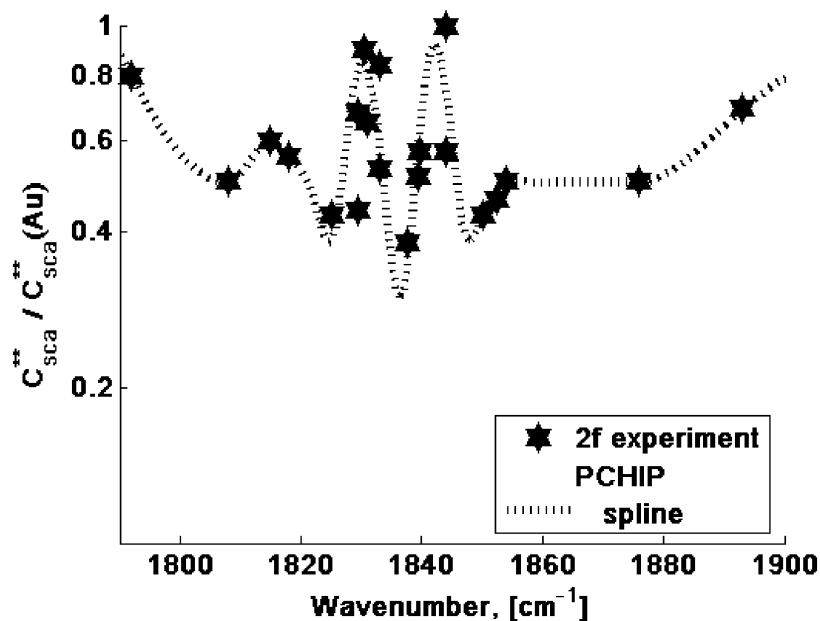


Figure 48. Second harmonic self-homodyned relative near-field scattering signal of di-iron nonacarbonyl on gold surface; interpolated by PCHIP, the piecewise cubic Hermite polynomial (step 3 nm) and the cubic spline (Matlab 7.0).

Detection at the second harmonic of the cantilever oscillation, without homodyning, resulted in near field spectrum of iron carbonyl that has multiple peaks near the frequency of vibrational resonance of bridging carbonyls, 1826 cm⁻¹ (Figure 48).

This is not what was expected, based on the simplified coupled-dipole model where the surface effects are approximated by the static image dipole (Figure 49).

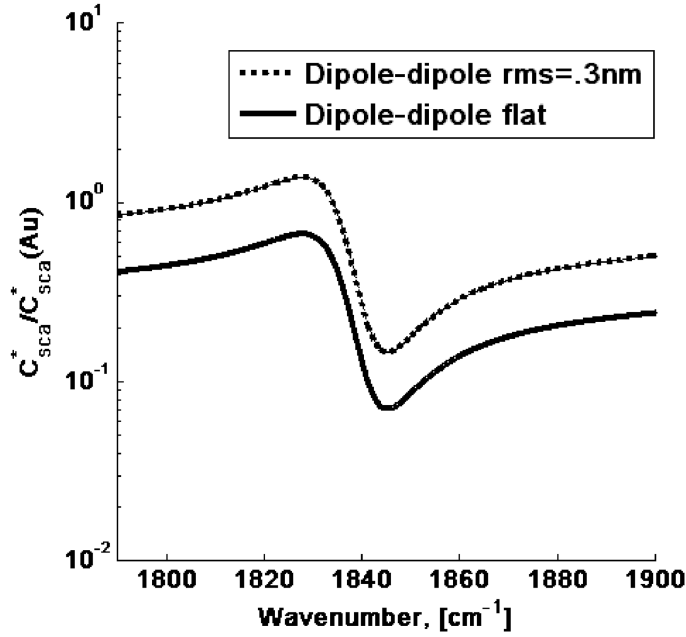


Figure 49. Computer simulations of $\text{Fe}_2(\text{CO})_9$ vs. gold near-field contrast, based on the static-dipole/image-dipole model and the effective medium approximation. Rough gold surface enhances the relative contrast of the iron carbonyl particles.

where $\alpha_{eff} = \frac{4\pi a^3(1+\beta)}{1 - \frac{\beta}{4(1+z/a)^3}}$ for an incident p-polarized plane electromagnetic wave.

The detected differential signal is proportional to the change in effective polarizability between the far field,

$$\left| \alpha_{eff}^{FF} \right| \cong 4\pi a^3 |\beta + 1| \quad (15)$$

and the near field,

$$\left| \alpha_{eff}^{NF} \right| \approx 4 \frac{\left| \alpha_{eff}^{FF} \right|}{|\beta - 4|}. \quad (16)$$

The calculations took into account the roughness of the gold film. The reflectivity of gold films has been studied for centuries. In recent years, several publications discussed the correlation between the reflectivity and various surface roughness characteristics.^{158, 159} *In situ* AFM roughness analysis on a typical 20 nm x 20 nm section of the gold substrate surface gave rms roughness = 0.7 nm and $R_a = 0.12$ nm. A higher resolution AFM showed that typical rms of our films is 0.3 to 0.5 nm on glass substrate and 0.2 nm for the ultra-flat gold films evaporated onto mica. The reflectivity of the gold substrate has been simulated for gold films with conductivity dominated by spherically shaped features with the radius of curvature between 0.2 and 0.3 nm. The resulting reflectivity is significantly lower than that of a perfectly flat surface of bulk gold, but a general shape of the spectrum remains the same.

Then the relative brightness of the sample (Figure 49) can be estimated as proportional to $|\alpha_{eff}(Pt \oplus sample)|/|\alpha_{eff}(Pt \oplus Au)|$, because of self-homodyning of the signal by the background scattering.

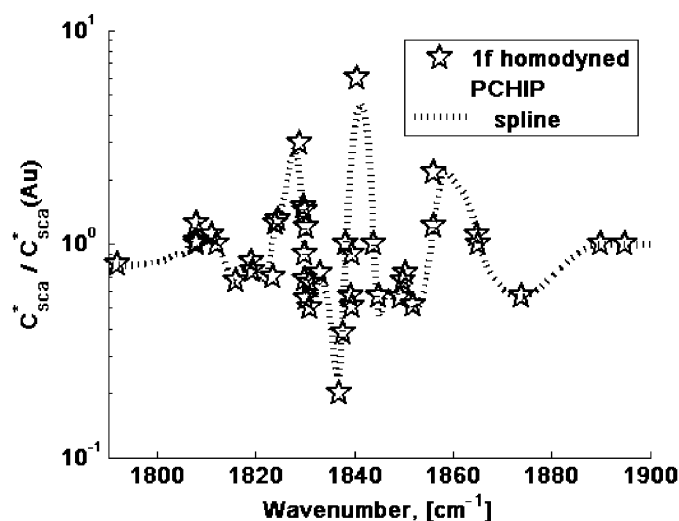


Figure 50. The first harmonic auto-homodyned relative near-field scattering signal of di-iron nonacarbonyl on gold surface. The contrast variations in resonance region are more dramatic than without homodyning.

The use of homodyning did not have any major impact on spectral profile, except for significant rise in magnitude of the scattering signal at the peaks (Figure 50). Since the homodyning option is designed to auto-tune the reference beam's phase shift for maximum amplitude of the interference demodulation signal at the lock-in detector reference frequency,¹²³ it can hop between gold and iron carbonyl maximum phases. On the other hand, without this option, the self-homodyned signal is optimized for

maximum phase of gold as the main scatter source. Then the difference between auto-homodyned and self-homodyned spectra should correlate with the phase relation between scattering from the sample and the substrate. As the instrument is typically aligned and focused with the cantilever being above the gold surface, it is not surprising that near the resonance the self-homodyned second harmonic signal had a tendency to be lower than the externally homodyned signal. In fact, the simulated phase difference (coupled-dipole model, see the NEC simulation in Appendix H) follows the same pattern as the apparent depression in the self-homodyned spectrum (Figure 51).

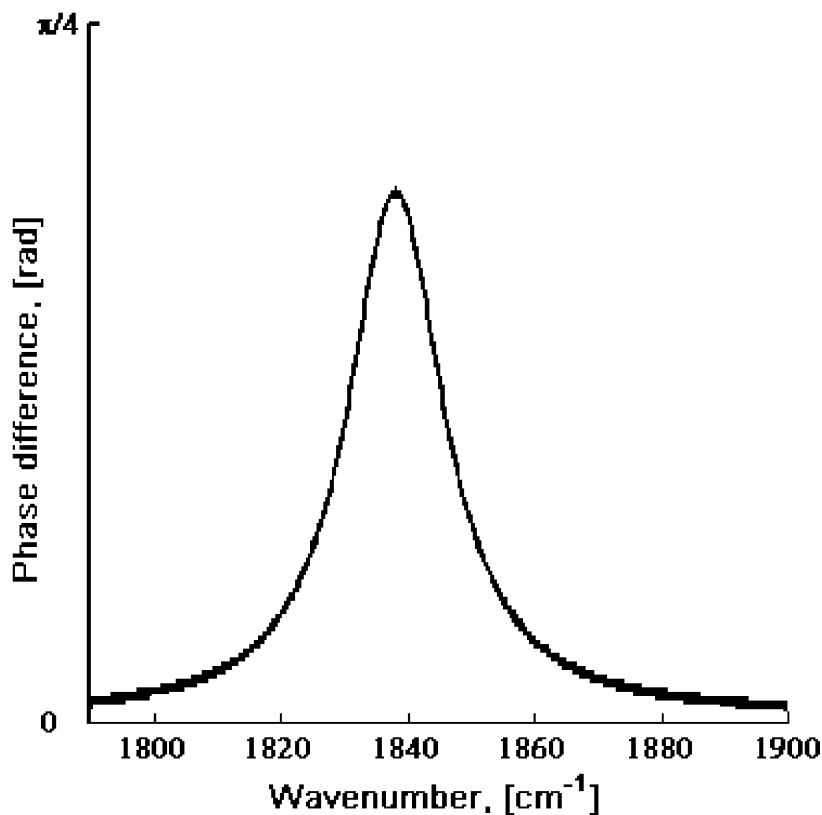
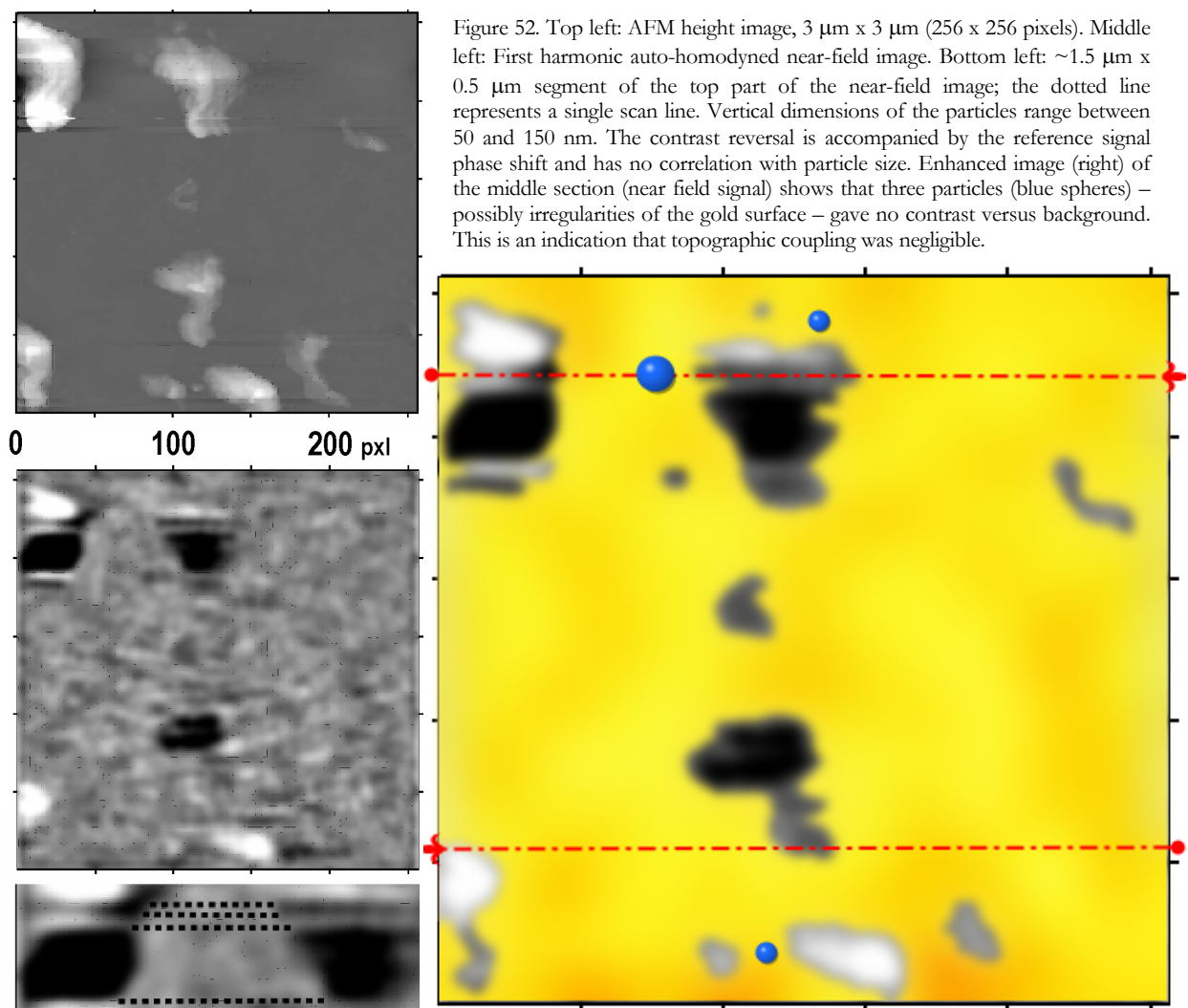


Figure 51. Computer simulations of $\text{Fe}_2(\text{CO})_9$ vs. gold near-field phase shift, based on the static-dipole / image-dipole model and the effective medium approximation.

However, the homodyned detection does not always promptly catch the phase that matches the highest signal for the surface that the cantilever is being scanned over. Whenever, the area is dominated by the highly reflecting iron carbonyl particles, which depends on the wavelength of light, the phase tends to tune to the particles and vice versa.



A clear manifestation of phase related effects has been observed at the wavelengths where the brightness of the particles is about the same as the brightness of the substrate. Slow (40-45 minutes) scans at 1856 cm^{-1} demonstrated that the phase jumps ($\sim \pi$ rad) at the lock-in amplifier cause immediate contrast reversals in the near-field image. The correlation is very strong within one scan line, i.e. 11.7 nm on 3 μm x 3 μm (256 x 256 pxl) image (Figure 52). Particle sizes (height: 30-150 nm; horizontal extension: 0.2-1.0 μm) had no effect on the sign or strength of the contrast. As the optics alignment and focusing had been performed above the gold surface, the starting phase (scanning from top to bottom) has been identified as optimal for gold. We observed that the iron carbonyl particles appeared darker than the substrate at this phase and brighter during the phase reversals.

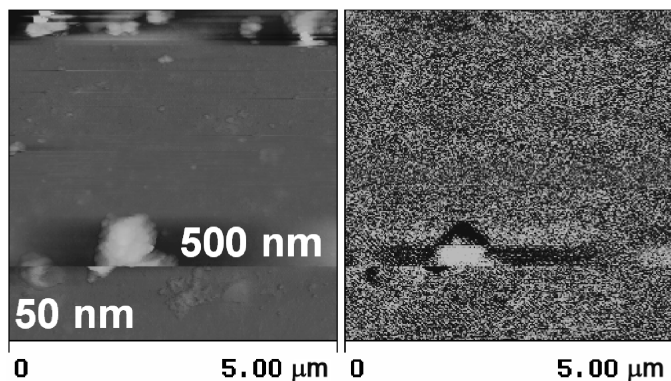


Figure 53. Left: AFM height image; numbers next to the particles indicate their heights. Right: Broadband second harmonic (315.4 kHz) auto-homodyned near-field image; gold surface appears darker whenever iron carbonyl is bright and vice versa.

Such contrast reversal is not limited to the first harmonic detection. Similar effects have been observed with a broadband CO laser (Figure 53) and rougher gold surface (100 nm thick sputter-coated layer), whenever the second harmonic detection with the auto-homodyning option was used. The key condition for observation of such phenomenon is that the peak scattering intensities have comparable values for the two types of surfaces (sample and substrate). Interestingly, the gold surface appears darker when the iron carbonyl particles are bright and vice versa. This is another indication of significant phase shift between the scattered signals coming from the gold surface and iron carbonyl particles, which results in different $\cos\phi$ values in Equation 8. Again, the particle sizes (height: 50-500 nm; horizontal extension: 0.1-1.0 μm) had no effect on the sign of the contrast (Figure 54). The absorption strength is also comparable for large and small particles. However, detuning of the wavelength, due to competition of the CO laser emission lines, (see Figure 38) obviously results in a loss of the near-field specific signal. This is manifested in a topographic coupling at the very large particles and a complete absence of any contrast at the smaller particles (Figure 54).

Because the image dipole approximation has obviously failed to accurately describe the near-field interaction of the iron carbonyl particles with gold substrate near the narrow vibrational resonance, we computed the same spectrum by using numerical electromagnetic code (NEC)¹⁵⁶ with Sommerfeld terms to account for the reflected dipole waves. For an observation point far from the surface, the reflection term is approximated by the field from an image dipole that is modified by Fresnel (plane-wave reflection) coefficients.¹²⁹ This option increases the calculational speed. The double-precision NEC2D codes, originally developed by Lawrence Livermore Laboratories, and the windows utility for source decks generation and output viewing (4NEC2, version 5.3.9 by Arie Voors, 4nec2@gmx.net) were downloaded from the NEC archives maintained by Raymond Anderson (WB6TPU, raymonda@ieee.org).

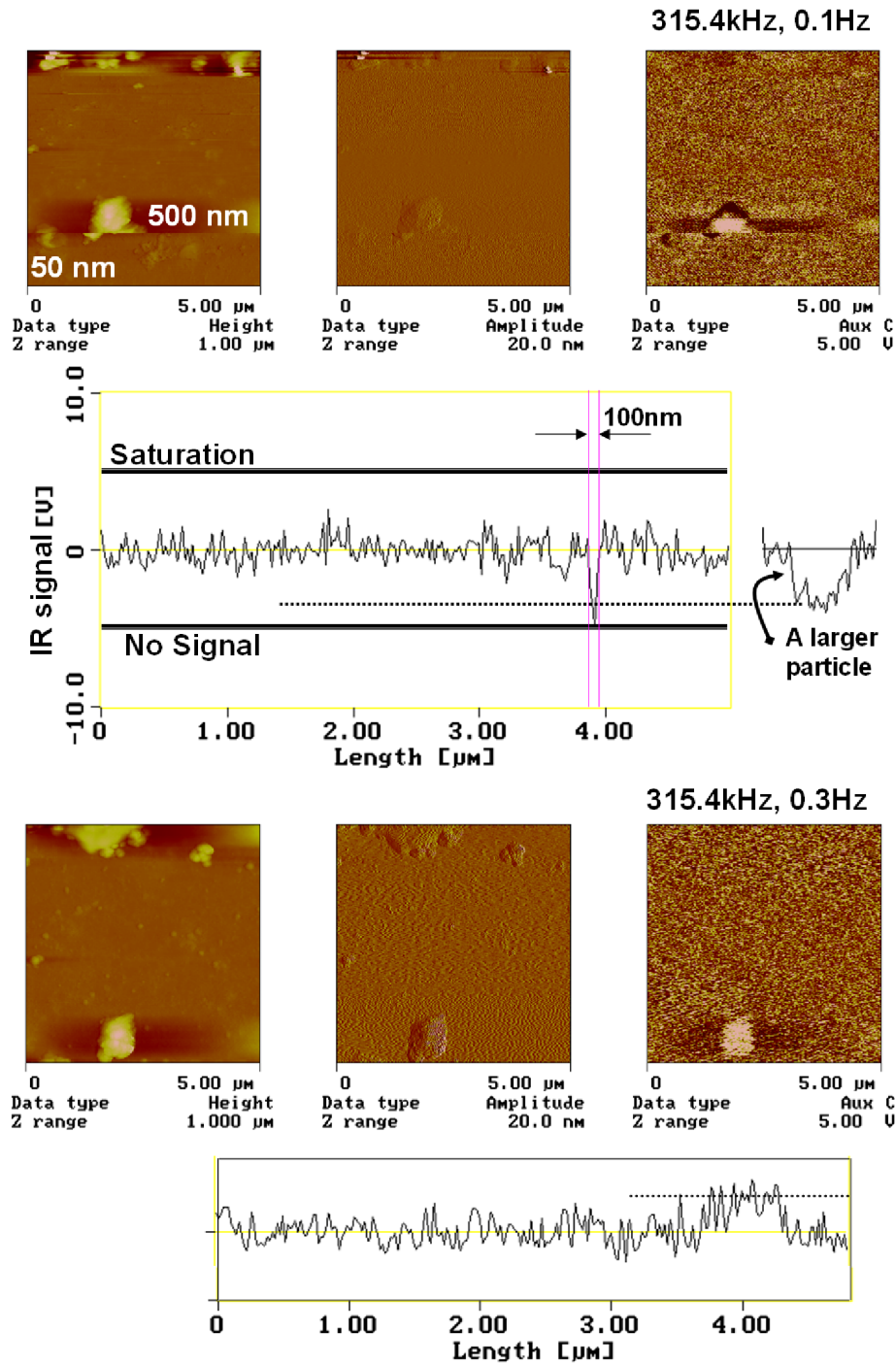


Figure 54. Second harmonic (315.4 kHz) detection with the broadband IR source and the auto-homodyning. Top: AFM height and phase plus ANSIM images. Bottom: Same scan as above one hour later, possibly, on a different wavelength.

We simulated a focused beam as a sum of eight plane waves, incident at $\sim 80^\circ$. The cantilever tip in our model was represented by a variable segmentation of a sphere, 80 patches of approximately equal areas, and both the sample and the substrate were simulated by half-space (Figure 55). The scattered

signal was calculated as a function of the observation angle, in horizontal (φ) and vertical (θ) planes. The back scattered waves were recombined alternatively as a sum of electric fields or intensities, with similar results. We tested this method by computing the scattering signal for two positions of the cantilever tip ($z = 0$ and far field) at various wavelengths and by comparing the relative signal (iron carbonyl vs. gold) away from vibrational resonance to analytical estimates within the coupled dipoles approximation.

Computational Model

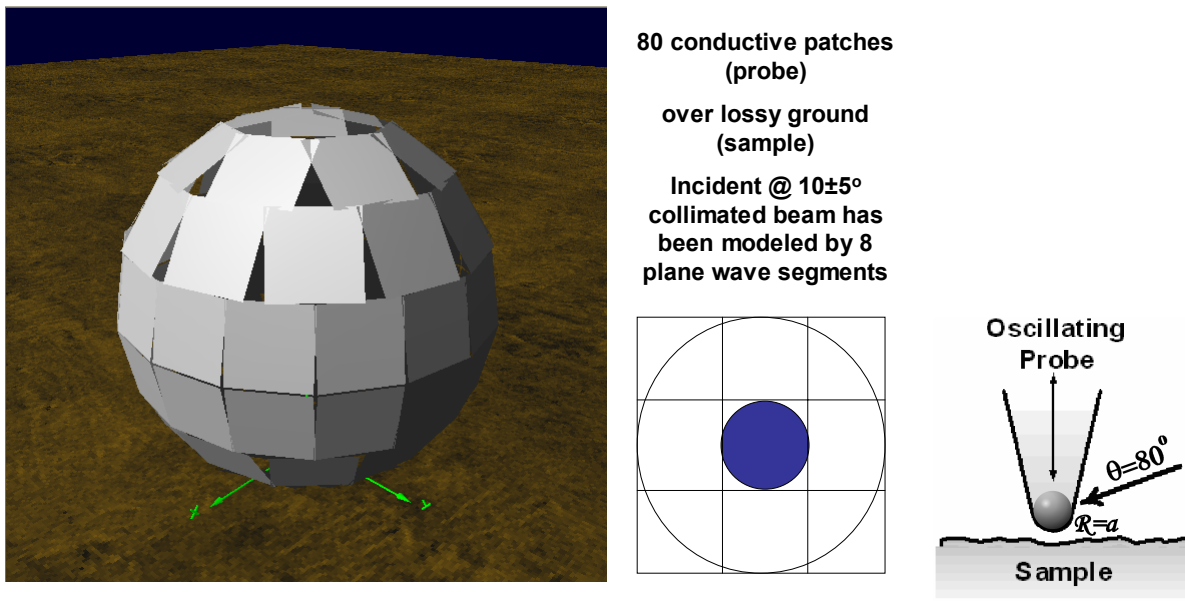


Figure 55. Geometrical model of a cantilever tip (80 patches) and a surface (half space) for NEC simulations.

The results of simulations for Fresnel reflection coefficients approximation do show some similarity with the second harmonic data without homodyning, but the first harmonic data collected with the use of the instrument's homodyning feature yield the results that are much closer to the NEC curve.

The Figure 56 compares the two theoretical models and the experimental data for the first harmonic homodyned signal. Unlike the static image-dipole model with effective medium approximation, the NEC Fresnel model does generate multiple peaks in the simulated near-field spectrum. The static image dipole approximation can fairly accurately fit the onset of the near-field absorption band and the relative contrast away from the narrow vibrational resonance. However, it does not account for the multiple sharp peaks at the frequencies just above the resonance.

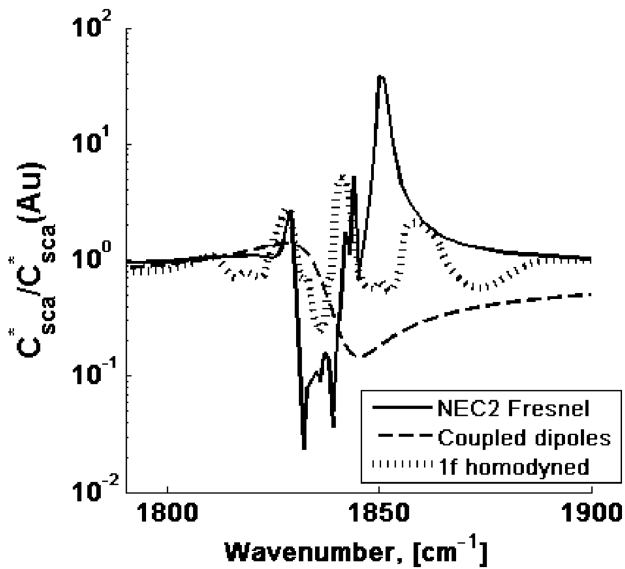


Figure 56. Comparison of the theoretical models and the experimental results for the first harmonic auto-homodyned near-field spectra.

The origin of the sharp peaks is in a strong directionality of the scattered waves (Figure 57) as opposed to the effective medium approximation for calculations of C_{sca} , the scattering cross-section. Thus, our experimental results provide the evidence that the simplified effective medium approximation that works well for materials with broad spectra is not reliable when it comes to modeling strong narrow resonances. At the same time, when the Sommerfeld reflection term is approximated by the image dipole that is modified by Fresnel reflection for the appropriate observation angle, a simple two-point estimate yielded useful results.

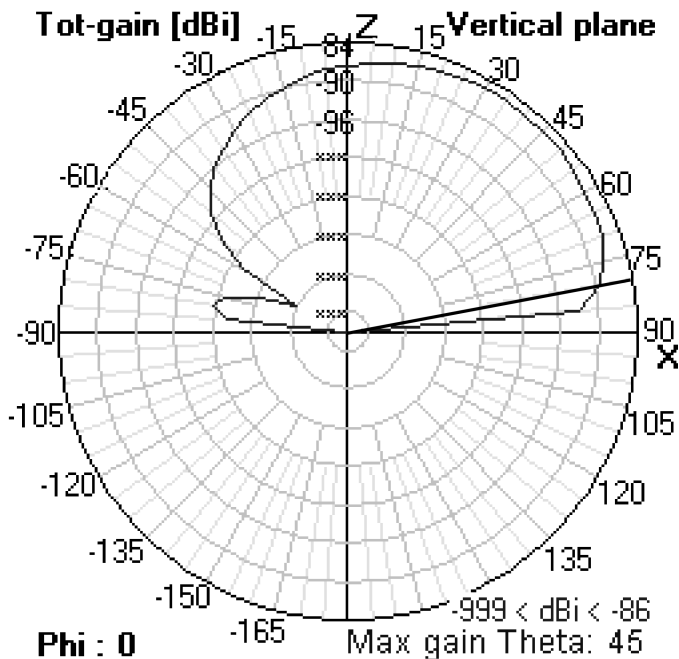


Figure 57. NEC simulations of the angular distribution in the 1845 cm^{-1} near-field scattering signal (plane of incidence); $\theta < 0$ for forward scattering. The line of incidence and back scattering is at $\theta = 80^\circ$.

The major apparent difference between the experimental data and the Fresnel model is the prominence of the short wavelengths peak. According to the model, this peak can be observed only very close to the surface. Thus, if the sample surface is not flat and the tip is not sharp enough, the intensity of the near field signal can drop. Theoretically, the signal is not expected to show strong dependence on the amplitude of oscillation since the near field components decay just a few nanometers away from the surface. However, that is not always the case as the cantilever tip may have some irregular shape or it can pick up some tiny chips that serve as imperfect conductors. Thus, we need a more sophisticated model that accounts for specific instrumental parameters and sample properties.

To quantitatively measure the concentration of specific chemical groups or detect conformational changes and intermolecular interactions on nano scale, the near field infrared microscopy should yield interpretable line shapes of the “fingerprint” resonances. In order to find a better fit of the experimental data, more detailed analysis is required of the parameters defining the dielectric function of the sample, z-dependence of the near-field signal, and the instrument function.

A knowledge of the dielectric functions of the sample and the cantilever tip as a function of frequency permits a prediction of the near-field spectrum. The best-fit combinations of Lorentzian oscillators (Equation 4) can be used to describe the dielectric function of iron carbonyl (see Table 7).

Table 7. Vibrational oscillator strengths: t=terminal, b=bridging.

Vibrational mode	ν , cm^{-1}	γ , cm^{-1}	Oscillator strength vs. ϵ_∞				
			1.5	1.8	2.0	2.1	2.2
$\nu(\text{Fe-C})_t$	454	16	0.0245	0.026	0.037	0.039	0.041
$\delta(\text{FeCO})_t$	599	15	0.116	0.117	0.185	0.196	0.207
$\delta(\text{FeCO})_t$	675	38	0.026	0.025	0.045	0.048	0.051
$\nu(\text{CO})_b$	1826	17.5	0.042	0.046	0.049	0.0506	0.0523
$\nu(\text{CO})_t$	2012	11	0.0248	0.0255	0.0255	0.0255	0.0256
$\nu(\text{CO})_t$	2018	14	0.0071	0.0115	0.015	0.0159	0.0167
$\nu(\text{CO})_t$	2086	12.5	0.008	0.0051	0.0054	0.0057	0.0059

In a coupled-dipole method, an array of dipole moments \mathbf{P} is found from the matrix equation:

$$\mathbf{A}\mathbf{P} = \mathbf{E}, \quad (17)$$

where \mathbf{E} is the total field at each dipole and \mathbf{A} is the interaction matrix.

In presence of the surface the interaction matrix must be modified to account for the reflection of the dipole waves from the surface; and the electric field \mathbf{E} becomes a standing wave. Thus,

$$\mathbf{A}_{ii} = 1/\alpha - \mathbf{R}_{ii}, \quad (18)$$

$$\mathbf{A}_{i \neq j} \bullet \mathbf{P}_j = -(E_{ij} + \mathbf{R}_{ij}), \quad (19)$$

where \mathbf{R} represents the reflected dipole wave;¹²⁹

$$E_{ij}(r) = k^2 (\mathbf{n}_{ij} \times P_j) \times \mathbf{n}_{ij} \frac{\exp(ikr)}{r} + [3\mathbf{n}_{ij} (\mathbf{n}_{ij} \bullet P_j) - P_j] \left(\frac{1}{r^3} - \frac{ik}{r^2} \right) \exp(ikr), \quad (20)$$

\mathbf{n}_{ij} is the unit-direction vector and k is the wave number of the incident radiation.

To simplify the analysis, the observation point was specified at 1 m away from the scatterer, at the angles of original incidence (70°, 75°, and 80°). Since the Sommerfeld/Norton method in NEC is only limited to wires, the reflection coefficient approximation was used for all interactions with patches. In practice the Fresnel approximation may be adequate for use in the dipole interaction matrix,¹²⁹ either due to sufficiently good representation of the Sommerfeld terms (as for the high-refractive index substrate) or because the direct interactions of the dipoles dominate the surface-derived interactions.

From parametric fit of the far field IR transmittance spectra, we estimated that the iron carbonyl ϵ_∞ was within the range 1.5-2.5 (90% confidence interval). After analysis of the high concentration measurements, we hypothesized that the observation of the 1826 cm^{-1} peak “bleaching” anomaly at the percolation limit is due to in-matrix multiple scattering. The extinction profile-matching values of ϵ_∞ were estimated to be 1.7-2.1, with 1.8-1.9 being the best fit.¹⁵⁶

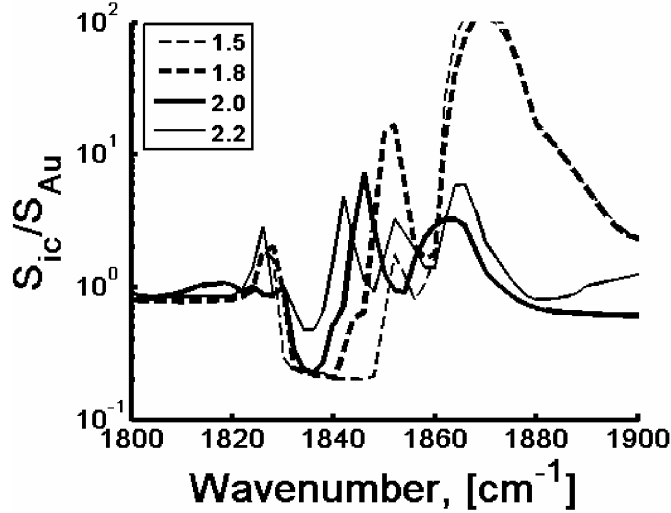


Figure 58. Typical NEC2 simulated response for $\epsilon_\infty = 1.5, 1.8, 2.0$ and 2.2 , which accounts only for a difference between the scattered signal from the tip touching the surface and the tip's far field position.

For the simplified near field spectrum, the best fit range of ϵ_∞ appears to be between 2.0 and 2.2 , while the theoretical plots for 1.5 to 1.8 have very high peaks at $1865\text{-}1875\text{ cm}^{-1}$ (Figure 58) and the predicted response for 2.4 is too flat. These spectra are lacking some features that would be present for the simulations of a focused beam but demonstrate similar trends. Alternatively, the same results as for the $\epsilon_\infty=2.1$ should be observed for the $\epsilon_\infty\approx 1.8\div 1.9$, if the oscillator strength of the 2018 cm^{-1} line is taken as 0.05 , which is still within the margin of error.

The error is so large because of the doublet splitting of a single molecular line in the polycrystalline iron carbonyl. In fact, the solid angle Ω averaging of the power absorbed by the face $(0001)^{160}$ of the polycrystalline flake, can increase the line intensity by three times (up to $0.035\text{-}0.045$):

$$\iint \cos^2(\theta) d\Omega = 1/3.$$

Figure 59 shows that transient electromagnetic modes (during the tip approach or lift-off phase) may give significant contributions at certain wavelengths, depending on the speed of the cantilever approach of the surface and the time it stays in direct contact with the sample. Our model treats these factors by introducing the effective set point, **sp** which accounts for the maximum change in the cantilever's deflection after it comes in contact with the surface (Figure 60). Here we call the "contact" a condition when the scattering field can be estimated in the zero (practically, less than 0.1 nm) tip-sample separation approximation. More detailed description of the model is given in Appendix H.

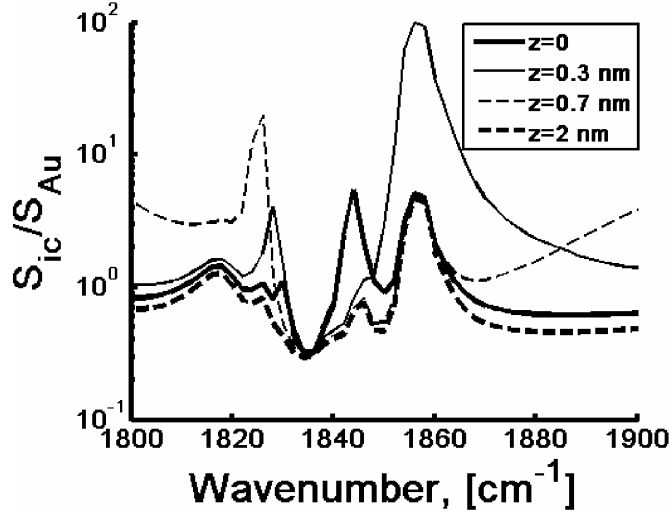


Figure 59. Transient modes contribution to the near field response for $\epsilon_\infty=2.1$. The signal as a function of the wavenumber practically does not change for some ranges of the tip-sample separation: between 0 and 0.1 nm, 0.2 - 0.4 nm, and above 2 nm. The large peak at 1855 cm^{-1} is only due to the transient modes.

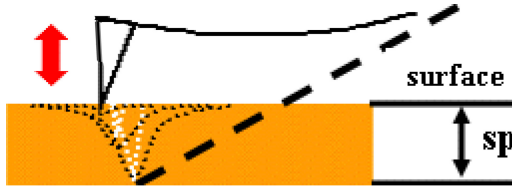


Figure 60. Cantilever deflection model. The cantilever body's additional (after the tip touched the surface) deflection, down to the z value, is assumed to be quasi-harmonic.

The lock-in amplifier output signal is calculated as

$$S_L = \oint_{-\infty}^t \cos(2\pi \cdot f \cdot t + \varphi) \cdot S_D(z(t')) \cdot F_D(t - t') dt' f dt, \quad (21)$$

where f is the reference frequency (frequency of the cantilever oscillation), φ is the phase shift introduced within the lock-in amplifier (it is assumed to be in phase with the maximum near field signal), and S_D is the signal proportional to the power collected by the infrared detector, which depends on the tip-sample separation z :

$$z(t) = z_0 \cos(2\pi f t) - \mathbf{sp}, \quad (22)$$

where z_0 is the amplitude of the cantilever's harmonic oscillation.

The instrument convolution function can be approximated by the exponential decay function:

$$F_D(t - t') = 2\pi \Delta f \cdot \exp(-2\pi \Delta f (t - t')), \quad (23)$$

where Δf is the MCT detector bandwidth.

Practically all near field features vanish at $z > 2$ nm, so we can estimate the signal as proportional to the difference between two extreme phases. We calculated the signal variability for the peak phases between zero and the phase (φ_L) corresponding to the tip's separation from the surface:

$$\varphi_L = \arccos(1 - sp/z_0). \quad (24)$$

For the bandwidth less than 700 kHz, the contribution of the transient modes becomes very significant and a good fit to the experimental data can be achieved only for increasingly large set point values (See Figures 61 and 62). For low set point values, the anharmonicity factors, such as the electrostatic or van der Waals tip-sample interactions at the lower part of the tip's trajectory, need to be accurately accounted for. Apparently, detection at the lower amplitudes z_0 should reduce this error.

The increase of the bandwidth above 800-900 kHz practically does not affect the theoretical plots, as well as the matching set point values. Interestingly, the best fit value of $\epsilon_\infty=2.1$ ($\Delta f=700$ kHz) shows a strong phase dependence around 1855 cm^{-1} (Figure 63). This is exactly what we observed experimentally.¹⁵⁶

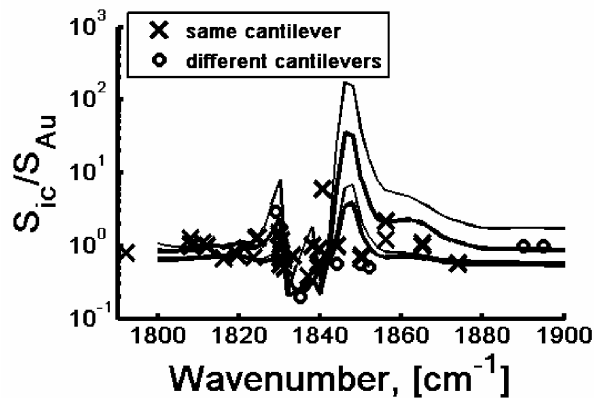


Figure 61. NEC2 simulated response for $\epsilon_\infty=2.0$ within the phase variation from 0 to the tip's lift-off from the surface; a good fit for $\Delta f=700$ kHz/ $sp=3$ nm (thick lines). The data variability near the absorption band is better accounted for by $\Delta f=500$ kHz/ $sp=8$ nm (thin lines).

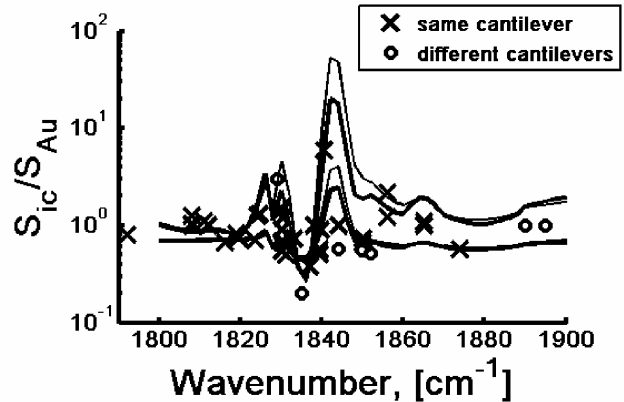


Figure 62. NEC2 simulated response for $\epsilon_\infty=2.2$, $\Delta f=700$ kHz/ $sp=3$ nm (thick lines) and $\Delta f=500$ kHz/ $sp=9$ nm (thin lines); same phases as in Figure 6. Technically, the correlation with the experimental data is still good but the plot starts to become too flat, especially within the absorption band.

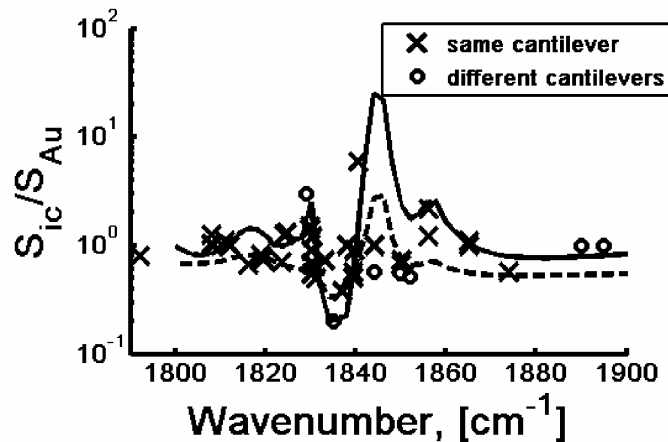


Figure 63. NEC2 simulated response for $\epsilon_{\infty}=2.1$, $\Delta f=700$ kHz, and $y=3$ nm; the best fit. The anomalous response variability between the zero detection phase (solid line) and the lift-off phase (dashed line) around 1855 cm^{-1} is similar to the experimental observations.

We used a fudge factor ΔS to shift the plots along the logarithmic scale of the relative signal to adjust for gold film brightness. ΔS varies from 0 for a rough thin (typically, 50-100 nm thick) film to 1.8 for a perfectly flat bulk gold surface. For all the NEC2 simulated plots, this parameter equals 0.2.

SUMMARY OF THE NEAR FIELD STUDY

We tested two theoretical models against our experimental data for correct prediction of the absorption band shift and of the overall shape of the near field spectrum. The static image dipole approximation can fairly accurately fit the onset of the near-field absorption band and the relative contrast away from the narrow vibrational resonance. However, it does not account for the multiple sharp peaks at the frequencies just above the resonance. (Figure 64)

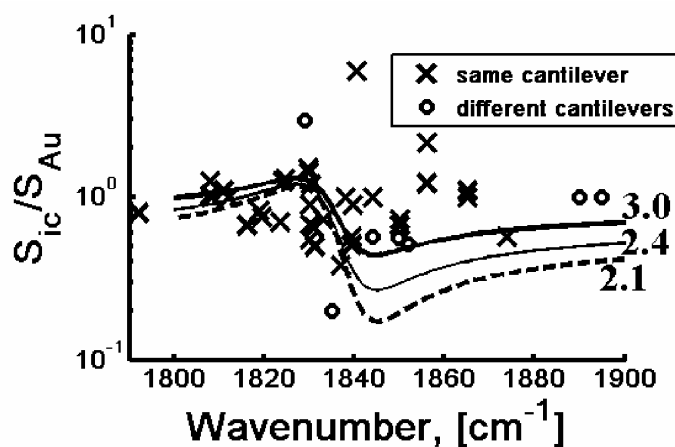


Figure 64. Static image dipole model (effective medium approximation). Even for very high dielectric constant of a sample ($\epsilon_\infty=2.1, 2.4,$ and 3.0), the model predicts very low ratio of the near field signal of iron carbonyl versus gold in the regions where bright reflection peaks are observed experimentally.

On the other hand, the NEC2 simulations showed that the low frequency edge of the major near field absorption band for iron carbonyl $\nu(\text{CO})_b$ vibrational mode matches the experimental data very well, while the shape of the secondary features strongly depends on the high-frequency dielectric function, ϵ_∞ . This model allows us to virtually eliminate the possibility of $\text{Fe}_2(\text{CO})_9$ decomposition into $\text{Fe}_2(\text{CO})_8$ isomers, because the displaced absorption band was not experimentally observed between 1805 and 1815 cm^{-1} . On the contrary, a group of experimental data points at around 1810 cm^{-1} sits just above a

minor local peak predicted by the model at 1815 cm^{-1} , although one might speculate that the experimental data in 1810 cm^{-1} to 1825 cm^{-1} range suggest some presence of excited states of $\text{Fe}_2(\text{CO})_9$, with the absorption bands shifted by $15\text{-}20\text{ cm}^{-1}$ rather than 25 cm^{-1} (complete decomposition).¹⁶¹ This result is significant by itself because the complex is known to undergo thermal decomposition at room temperature under a focused laser beam.¹⁶² (In our experiment, the IR laser beam, with the power of $50\text{-}100\text{ mW}$, was focused into a small spot of ~ 50 micron diameter.)

The fit of experimental data by a wide band rather than a line is the main issue of this study. A good correlation between the boundaries of the set point interval and the spread of the experimental data points, most notably within $1850\text{-}1860\text{ cm}^{-1}$ range (Figure 63), indicates a strong dependence of the near field signal on the quality of the contact between the cantilever tip and the sample. In order to collect the data set that can be fitted by a single trend line, the reproducibility of the contact should be significantly improved, which requires significant advances in the design of the AFM apparatus. Data collection should be very systematic, that is the area of the particle to be monitored should be selected prior to scan and the data point can not be rejected based on post hoc rationalization.

Once the experimental techniques are dramatically improved – this may take a few years of research – the proposed theoretical model will be truly tested. It is possible that some improvements can be made within the Fresnel reflection coefficients approximation, such as creating a fine mesh of computed data points for z dependence (very time consuming) so that Fourier transform integration could be done over the entire path of the cantilever tip. The source can be more finely approximated by a sum of the plane waves incident at the various angles within a cone of the focused beam. Alternatively, the wire model (instead of patches, Figure 55) could be used to simulate the cantilever tip. It is not as good as the patch model in representing the voluminous bodies but it has an advantage of a second ground option (accounting for a finite thickness and lateral dimensions of a particle) as well as the option of using the Sommerfeld/Norton method, very time consuming but more appropriate than the above Fresnel model for the scattering objects very close to the surface.

Another issue is the anisotropy of the dielectric function of iron carbonyl due to contribution of the terminal stretching band at $\sim 2015\text{ cm}^{-1}$. Both IR-unique and Raman-unique bands can take part in the near field interaction, because the electromagnetic modes that interfere near the surface are not purely TE or TM plane waves and the selection rules can be relaxed. The fact that NEC2 does not allow for anisotropic dielectric function is a serious limitation of this version of the code.

BIBLIOGRAPHY

1. Kreibig, U. and Vollmer, M. *Optical Properties of Metal Clusters* (1995)
2. Ash, E. A. & Nichols, G. *Nature* **237** (1972) 510-512
3. Akhremitchev, B. B.; Pollack, S.; Walker, G. C. *Langmuir* **17** (2001) 2774-2781
4. Knoll, B. & Keilmann, F. *Nature* **399** (1999) 134-137
5. Romanov, V. N. & Walker, G. C. "Infrared Near-field Detection of a Narrow Resonance due to Molecular Vibrations in a Nanoparticle," Prepared for *Langmuir* (2005)
6. Stas, Joseph D. in: *Glass Processing Days*, ISBN 959-91-0885-0 (1999)
7. Sakoske, G. E., Ryan J., Romanov, V., Klimas, D., Tunker, G. and Heitman, O. in: *Glass Processing Days*, ISBN 959-91-0885-0 (1999)
8. Boaz, P. in: *Glass Processing Days*, ISBN 959-91-0885-0 (1999)
9. Anquetil, J. & Danger, A. U.S. Patent 5,350,718 (1994) 501/21
10. Chang, R. K.; Furtak, T. E. (Eds.), *Surface Enhanced Raman Scattering*, Plenum Press, New York (1982)
11. McQuillan, A. J.; Hendra, P. J.; and Fleischmann, M. J. *Electroanal. Chem.* **65** (1975) 933
12. Hache, F.; Ricard, D.; and Flytzanis, C. *J. Opt. Soc. Am. B* **3** (1986) 1647
13. Niklasson, G. A. *Solar Energy Materials* **17** (1988) 217
14. Papavassiliou, G. C. *Prog. Solid State Chem.* **12** (1980) 185
15. Kreibig, U. *J. Phys. F: Met. Phys.* **4** (1974) 999
16. Libuda, J. et al. *Rev. Sci. Inst.* **71** (2000) 4395
17. Wang, C. R. C. et al. *Z. Phys. D: Atoms, Molecules and Clusters* **19** (1991) 13
18. Jean, J. H. ; Gupta, T. K. *J. Mat. Res.* **7** (1992) 3103
19. Barzakovskii, V. P. *Khimicheskoe i Prakticheskoe Primenenie Silikatov*, Inst. Khimii Silikatov, Acad. Sci. USSR (1960) 189
20. Chen, P. J.; Colaianni, M. L.; Yates, J. T.; and Arbab, M. Jr. *J. Non-Crystalline Solids* **155** (1993) 131
21. Ichikura, E., Yonemori, S., Satoh, M., Hayashi, Y. in: *Glass Processing Days*, ISBN 959-91-0885-0 (1999)

22. Sakoske, G. E. *Glass Researcher* (Alfred University) **7** (1997) 11
23. Svedberg, Th. *Kolloid Z.* **53** (1930) 96
24. Cockram, D. R.; Haider, Z.; and Roberts, G. J. *Phys. Chem. Glasses* **10** (1969) 18-22
25. Guggenheim, E. A. *Thermodynamics* (1967)
26. de Groot, S. R. and Mazur, P. *Non-Equilibrium Thermodynamics* (1969)
27. Alper, A. M. (Ed.) *Phase Diagrams: Mat. Sci. and Technol.* **1** (1970)
28. Rosenberger, F. *Fundamentals of Crystal Growth I* (1979)
29. Lupis, C. H. P. *Chemical Thermodynamics of Materials* (1983)
30. Chernov, A. A. in: *Modern Crystallography III* (1984)
31. Wilke, K. Th. & Bohm, J. *Kristallzuchtung* (1988)
32. Pelton, A. D. in: Haasen, P. (Ed.) *Mat. Sci. and Technol.* **5** (1991)
33. Hurle, D. T. J. (Ed.) *Handbook of Crystal Growth* **1a** (1993)
34. Rudolph, P. in: Fornari, Paorici (Eds.) *Theoretical and Technological aspects of Crystal Growth* (1998) 1
35. Parker, R. L. in: Ehrenreich et al. (Eds.) *Solid State Physics* **25** (1970)
36. Hurle, D. T. J. (Ed.) *Handbook of Crystal Growth* **3** (1994)
37. Jackson, K. A. in: *Am. Soc. Metals* (1958) 99
38. Markov, I. V. *Crystal Growth for Beginners* (1995)
39. Tiller, W. A. *The Science of Crystallization: Microscopic Interfacial Phenomena* (1995)
40. Mie, G. *Ann. Phys.* **25** (1908) 377-445
41. Bond, W. L. & Andrus, J. *Phys. Rev.* **101** (1956) 1211
42. McKenzie, H. W. & Hand, R. J. (Eds.) *Basic Optical Stress Measurement in Glass*, Society of Glass Technology (1999)
43. Shui, W. Y.; Bennema, P.; van der Linden, W. H.; Boshaar, J.; Van Kessel, J. W. M.; and Klapper, H. *J. Crystal Growth* **83** (1987) 471
44. Norman, N. C. (Ed.) *Chemistry of Arsenic, Antimony and Bismuth* (1998)
45. Ingle, J. D., Jr. & Crouch, S. R. *Spectrochemical Analysis* (1988)
46. Peters, D. G., Hayes, J. M., Hieftje, G. M. *A Brief Introduction to Modern Chemical Analysis* (1976)

47. Scherrer, P. *Nachr. Ges. Wiss. Göttingen* **2** (1918) 96
48. Pye, La Course, Stevens (Eds.) *The Physics of Non-Crystalline Solids* (1992) 387
49. Simmons, Uhlmann, Beall (Eds.) *Advances in Ceramics*, ACS **4** (1982)
50. Zanotto, E. D. *J. Non-Cryst. Solids* **129** (1991) 183-190
51. Turnbull, D.; Fisher, J. C. *J. Chem. Phys.* **17** (1949) 71-73
52. James, P. F. *J. Non-Cryst. Solids* **73** (1985) 517-540
53. Zanotto, E. D. & James, P. F. *J. Non-Cryst. Solids* **74** (1985) 373-394
54. Weinberg, M. C.; Zanotto, E. D. *J. Non-Cryst. Solids* **108** (1989) 99-108
55. Jortner, J.; Levine, R. D.; and Rice, S. A. (Eds.) *Adv. Chem. Phys.*, John Wiley & Sons, New York **70** (1987) 263
56. Tolman, R. C. *J. Chem. Phys.* **17** (1949) 333-337
57. Oriani, R. A. and Sundquist, B. E. *J. Chem. Phys.* **38** (1963) 2082-2089
58. Doremus, R. A. (Ed.) *Growth and Perfection of Crystals* (1958)
59. Kolmogorov, A. N. *Izv. Akad. Nauk SSSR, Ser. Matem.* **3** (1937) 355-359
60. Johnson, W. A. & Mehl, B. F. *Trans. AIME* **135** (1939) 416
61. Avrami, M. J. *Chem. Phys.* **7** (1939) 1103-1112
62. Avrami, M. J. *Chem. Phys.* **8** (1940) 212-224
63. Avrami, M. J. *Chem. Phys.* **9** (1941) 177-184
64. Weinberg, M. C. *J. Non-Cryst. Solids* **72** (1985) 301-314
65. Dusil, J. and Cervinka, L. *Glass Tech.* **17** (1976) 106-112
66. Marotta, A.; Buri A.; Valenti G. L. *J. Mater. Sci.* **13** (1978) 2483-2486
67. Hautojärvi, P.; Vehanen, A.; Komppa, V.; Pajanne, E. *J. Non-Cryst. Solids* **29** (1978) 365-381
68. Francillon, N. J.; Pacadd, F.; and Querille, P. in: *Proc. Int. Symp. Radwaste Management* (1982) Berlin, RFA
69. Zanotto, E. D. & Galhardi, A. *J. Non-Cryst. Solids* **104** (1988) 73-80
70. Turnbull, D. *Contemp. Phys.* **10** (1969) 473

71. Uhlmann, D. R. *J. Non-Cryst. Solids* **7** (1972) 337-348
72. Cabral, A. A. Jr.; Fredericci, C.; and Zanotto, E. D. *J. Non-Cryst. Solids* **219** (1997) 182-186
73. Bard, A. J. & Faulkner, L. R. *Electrochemical Methods* (1980)
74. Shriver, D. F. & Atkins, P. *Inorganic Chemistry* (1994)
75. Cotton, F. A. & Wilkinson, G. *Advanced Inorganic Chemistry* (1988)
76. Haberland, H. (Ed.) *Clusters of Atoms and Molecules* (1994)
77. Mulvaney, P. *Langmuir* **12** (1996) 788-800
78. Mackay, R. A.; Texter, J. (Eds.) *Electrochemistry in Colloids and Dispersions*, VCH Pub., New York (1992)
79. Henglein, A.; Mulvaney, P.; and Linnert, Th. *Faraday Discuss.* **92** (1991) 31-44
80. Romanov, V. N. "Formation and spectral properties of silver clusters in sintered glass composites," *J. Non-Cryst. Solids* (In press, 2005)
81. Ahmed A. A., Abd Allah E. W., *J. Am. Ceramics Soc.* 1995; **78**: 2777-2784.
82. Hole D. E., Stepanov A. L., Townsend P. D., *Nuclear Inst. Methods Research B.* 1999; **148**: 1054-1058.
83. Nistor L. C., van Landuyt J., Barton J. D., Hole D. E., Skelland N. D., and Townsend P. D. *J. Non-Cryst. Solids.* 1993; **162**: 217-224.
84. Henglein, A. *J. Phys. Chem.* **97** (1993) 5457-5471
85. Torigoe, K. & Esumi, K. *Langmuir* **9** (1993) 1664-1667
86. Tiggesbaumker, J.; Koller, L.; Meiwes-Broer, K. H.; Liebsch, A. *Electr. Waves* **2** (1993) R1749
87. Zachariasen, W. H. *J. Am. Chem. Soc.* **54** (1932) 3841. - *Glastechn. Ber.* **11** (1933) 120
88. Frischat, G. H. *Ionic Diffusion in Oxide Glasses*, Trans Tech Publications, Ohio (1975)
89. Boolchand, P. and Blesser, W. J. *Nature* **410** (2001) 1070
90. Weast, R. C. *CRC Handbook of Chemistry and Physics*, CRC Press, Cleveland (1981) F-216
91. Asahara, Y.; Sakai, H.; Ohmi, S.; Nakayama, S.; Yoneda, Y.; Izumitani, T. *Applied Optics* **25** (1986) 3384

92. Ross, L.; Lilienhof, H. J.; and Holsher, H. W. *Buried waveguides for passive integrated optics by Cs+ exchange*, SPIE **651** (1986) 32
93. Fan, T. *Thermal Diffusion of Silver in the Ion Exchanged Glasses* (1993)
94. Morey, G. W. in: *Properties of Glass*, Reinhold Publishing Corporation, New York (1960)
95. Lilienhof, H.; Voges, E.; Ritter, D.; Pantschew, B. *IEEE J. Quantum Electronics* **18** (1982) 1877
96. Rothmund, V. and Kornfeld, G. *Z. Anorg. Allgem. Chem.* **103** (1918) 129
97. Deppe, J. in: Balkanski, M. and Elliot, R. (eds.) *Atomic Diffusion in Disordered Materials: Theory and Applications* (1998)
98. Ramaswamy, R. W.; Cheng, H. C.; Srivastava, R. *Applied Optics* **27** (1988) 1814
99. Lide, R. D. (Ed.) *CRC Handbook of Chem. & Phys.*, CRC Press (1995) 5-7
100. van de Hülst, H. *Light Scattering by Small Particles*, Wiley, New York (1957)
101. Vobornik, D. et al. *Infrared Physics & Technology* **45** (2004) 409-416
102. Dazzi, A. & Salomon, L. *Int. Workshop on Infrared Microscopy and Spectroscopy with Accelerator Based Sources*, Lake Tahoe, CA (2003)
103. Gross, N. et al. *EPJ-AP* **16** (2001) 91
104. Keilmann, F. J. *Electron Microscopy* **53** (2004) 187-192
105. Poliakoff, M.; Turner, J. J. *J. Chem. Soc. (A)*, London (1971) 2403-2411
106. Romanov, V.; Stebounova, L.; Akhremitchev, B.; Walker, G. *Proc. ANTEC - Society of Plastics Engineers* **2** (2004) 2364-2366
107. Park, E. S.; Andrews, S. S.; and Hu, R. B. *J. Phys. Chem. B* **103** (1999) 9813
108. Powell, H. M. & Evans, R. V. G. *J. Chem. Soc.*, London (1939) 286
109. Cotton, F. A. & Wilkinson, G. *Advanced Inorganic Chemistry*, Wiley-Interscience, New York (1973)
110. Butler, I. S.; Kishner, S.; and Plowman, K. R. *J. Mol. Struct.* **43** (1978) 9-15
111. Adams, D. M. and Taylor, I. D. *J. Chem. Soc., Faraday Trans. 2* **78** (1982) 1551
112. Kristoff, J. S. and Shriver, D. F. *Can. J. Spectrosc.* **19** (1974) 156

113. Jang, J. H.; Lee, J. G.; Lee, H.; Xie, Y.; Schaefer, H. F. III *J. Phys. Chem. A* **102** (1998) 5298
114. Dunning, T. H. *J. Chem. Phys.* **53** (1970) 2823
115. Huzinaga, S. *J. Chem. Phys.* **42** (1965) 1293
116. Ghodgaonkar, D. K.; Ali, N. A.; Giubbolini, L. *15th World Conference on Non-Destructive Testing*, Rome, Italy (2000)
117. Angelescu, C.; Negosanu, M.; Ioachim, A.; Itoacsen, M.; Sandu, D. D. *16^{eme} Colloque International Optique Hertzienne et Dielectriques Groupement AMPERE*. Universite du Maine, Le Mans, France (2001) 369
118. Wessel, J. J. *Opt. Soc. Am. B* **2** (1985) 1538-1540
119. Hayazawa, N.; Inouye, Y.; Sekkat, Z.; Kawata, S. *Chem. Phys. Lett.* **335** (2001) 369-374
120. Kawata, S. (Ed.) *Near-Field Optics and Surface Plasmon Polaritons*, Springer, Osaka, Japan (2001)
121. Lahreck, A.; Bachelot, R.; Cleyzes, P.; Boccara, A. C. *Appl. Phys. Lett.* **71** (1997) 575-577
122. Grésillon, S.; Ducourtieux, S.; Lahrech, A.; Aigouy, L.; Rivoal, J. C.; Boccara, A. C. *Appl. Surf. Sci.* **164** (2000) 118-123
123. Stebounova, L.; Akhremitchev, B. B.; Walker, G. C. *Review of Scientific Instruments*, **74** (2003) 3670-3674
124. Akhremitchev, B. B.; Sun, Y.; Stebounova, L.; Walker, G. C. *Langmuir*, **18** (2002) 5325-5328
125. Wurtz, G.; Bachelot, R.; and Royer, P. *Eur. Phys. J. Appl. Phys.* **5** (1999) 269-275
126. Knoll, B.; Keilmann, F. *Opt. Commun.* **182** (2000) 321-328
127. Gorobets, V. A.; Petukhov V. O.; Tochitsky, S. Ya.; Churakov, V. V. *Applied Physics B* **64** (1997) 423-427
128. Bohren, C. F. & Huffman, D. R. *Absorption and Scattering of Light by Small Particles*, Wiley, NY (1983)
129. Taubenblatt, M. A.; Tran, T. K. *J. Opt. Soc. Am. A* **10** (1993) 912
130. Wojcik, G. L.; Vaughn, D. K.; and Galbraith, L. K. in: Ehrlich and Tsao (eds.) *Lasers in Microlithography*, Proc. Soc. Photo-Opt. Instrum. Eng. **774** (1987) 21-31
131. Bobbert, P. A. and Vleiger, J. *Physica* **137A** (1986) 209-242
132. Assi, F. I. *Electromagnetic wave scattering by a sphere on a layered substrate*, Master's Thesis, U. of Arizona, Tucson, Ariz., 1990

133. Videen, G. J. *Opt. Soc. Am. A* **9** (1992) 1341-1351
134. Johson, B. R. *J. Opt. Soc. Am. A* **9** (1992) 1341-1351
135. Sommerfeld, A. and Renner, F. *Ann. Phys.* (1942) 41
136. Aravind, P. K.; Metiu, H. *Surf. Sci.* **124** (1983) 506-528
137. Akhremitchev, B. B.; Walker, G. *C. Bulletin of the Chem. Society of Japan* **75**(5) (2002) 1011-1018
138. Sommerfeld, A. *Ann. Phys.* **28** (1909) 665
139. Weyl, H. *Ann. Phys.* **60** (1919) 481
140. Baños, A. Jr. *Dipole Radiation in the Presence of a Conducting Half-Space*. Pergamon, Oxford, 1966
141. Mohsen, A. *IEE Conf. Publ.* **129H** (1982) 177
142. Michalski, K. A. *IEE Conf. Publ.* **132H** (1985) 312
143. Michalski, K. A. and Butler, C. M. *IEE Conf. Publ.* **134H** (1987) 93
144. Drachman, B.; Cloud, M.; and Nyquist, D. P. *IEEE Trans. Antennas Propag.* **37** (1989) 403
145. Wait, J. R. *Proc. IEEE Trans. Antennas Propag. Symp. Dig.* (1997) 240
146. Collin, R. E. *IEEE Trans. Antennas Propag.* **52** (2004) 3133
147. Yokoyama, A. *IEEE Trans. Antennas Propag.* **43** (1995) 541
148. Wait, J. R. *IEEE Trans. Antennas Propag.* **44** (1996) 271
149. King, R. W. P. and Sandler, S. S. *IEEE Trans. Antennas Propag.* **45** (1997) 309
150. Mahmoud, S. F. *IEEE Trans. Antennas Propag.* **47** (1999) 1745
151. King, R. W. P. and Sandler, S. S. *IEEE Trans. Antennas Propag.* **47** (1999) 1746
152. King, R. W. P. *Radio Sci.* **25** (1990) 149
153. Lager, D. L.; Lytle, R. J. *Rep. UCRL-51688*, Lawrence Livermore Laboratory, Livermore, CA, 1974
154. Lager, D. L.; Lytle, R. J. *Rep. UCRL-51821*, Lawrence Livermore Laboratory, Livermore, CA, 1975
155. Burke, G. J. and Poggio, A. J. *Rep. UCID 18834*, Lawrence Livermore Laboratory, Livermore, CA, 1975

156. Romanov, V. N.; Walker, G. C.
“The Resonance Effects in the
Electromagnetic Response of a
Sphere-Plane Structure;
Applications to Apertureless
Near-field Microscopy,” Prepared
for *Langmuir* (2005)
157. Zenhausern, F.; Martin, Y.; and
Wickramasinghe, H. K. *Science* **269**
(1995) 1083-1085
158. Munoz, R. C.; Arenas, C.;
Kremer, G.; Moraga, L. *J. Phys.:
Condens. Matter* **12** (2000) L379
159. Munoz, R. C.; Vidal, G.; Kremer,
G.; Moraga, L.; Arenas, C. *J. Phys.:
Condens. Matter* **11** (1999) L299
160. Adams, D. M.; Taylor, I. D.
J. Chem. Soc., Faraday Trans. 2 **78**
(1982) 1551
161. Poliakoff, M.; Turner, J. J. *J.
Chem. Soc. (A)* (1971) 2403
162. Swanson, B. I.; Rafalko, J.;
Shriver, D. F.; San Filippo, J. Jr.;
and Spiro, T. G. *Inorg. Chem.* **14**
(1975) 1737

APPENDIX A:
CHEMICAL DIFFUSION

1. CEMENTATION EXCHANGE

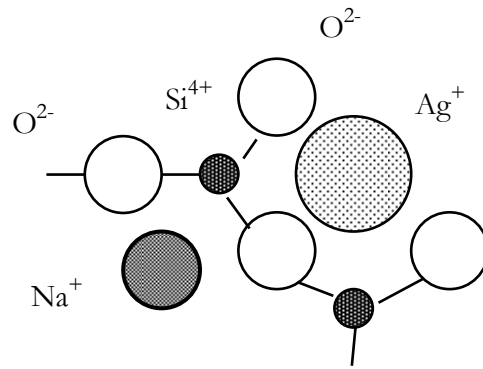
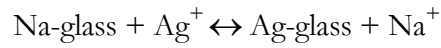
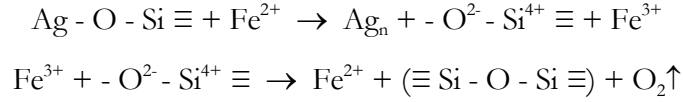


Figure A1. Ions in Glass network.

The Si-O network of the glass may be regarded relatively stable during ion-exchange reaction. According to Zachariassen's (random-network)⁸⁷ model, the basic units in vitreous silica are $\text{SiO}_{4/2}$ tetrahedra forming short-range order. When network modifiers Na and Ca are added to SiO_2 , the cation Na^+ goes into holes in the network which exist between the oxygen tetrahedra. For each Na_2O molecule added to SiO_2 , two nonbridging oxygens are formed with alkali ions randomly distributed in the network (experimental evidence⁸⁸ favors some preferred clustering of the modifying cations). The rapid diffusion of Ag^+ ions through the tetrahedral interstitial sites is due to a delicate balance between ionic and covalent forces. This balance causes the free energy difference between hexa coordinate and tetra coordinate Ag to nearly vanish.⁸⁹ The larger radius of Ag^+ compared to Na^+ ($r_{\text{Ag}^+}/r_{\text{Na}^+} = 1.29$)⁹⁰ results in glass surface defects as silver ions replace sodium ions at the vacancies of the glass network. (It is known to cause large, up to 0.22-0.27, depending on degree of ion conversion, increase in refractive index.)⁹¹ Thus, silver ions (atoms) inside the network will tend to move towards the surface to minimize the strain energy. The thermally activated breaking of Ag-O bond can result in oxygen evolution and formation of pure silica glass in the areas depleted of sodium.

2. ROLE OF POLYVALENT ELEMENTS (CATALYSIS)

Ag^+ has been found to be thermally unstable in ion-exchange glasses.⁹²



(“ \equiv ” here refers to glass network bonding)

Although the binding energy in silver metal is about 0.5-0.7 eV lower than Ag-O bond energy in ion-exchange glass, the energy gain due to increase in binding energies of O1s and Si2p outweighs it.⁹³

3. MULTICOMPONENT DIFFUSION

In 1945, Onsager extended the Fick's first law to describe diffusion in multicomponent (N species with elimination of r -th species flux) system by $(N-1)$ square matrix of diffusion coefficients D_{ij}^r , originally in terms of chemical potential (free energy per particle) gradients. In silicate structures (glasses), the volume is largely controlled by oxygen spacing; the cations fit into interstices and can move with their intrinsic flux densities. Thus, the condition of no overall pressure build-up is

$$V_o \cdot J_o = 0$$

where the change in volume of the system due to addition of oxygen

$$V_o = (\partial V / \partial N_o)_{T,P,N_j,\dots}$$

Since the oxygen density is nearly constant over a wide range of compositions,⁹⁴ the convention of a single anion system appears a reasonable premise for oxide glasses. This means the oxygen anion is in chemical equilibrium everywhere and migrates only to preserve electrical neutrality.

Then the diffusion equation for diffusing ion A (silver) can be derived in the following form:⁹⁵

$$\frac{\partial C_A}{\partial t} = \frac{\mu_A \cdot \mathbf{E} \cdot \nabla C_A + n \cdot D_A \cdot \nabla^2 C_A}{(1 - \alpha \cdot C_A)},$$

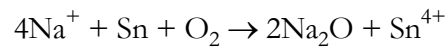
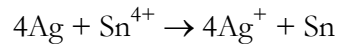
where $\alpha = 1 - \mu_A / \mu_B$, μ_i is the mobility of ion i , \mathbf{E} is the applied electric field, C_A is the concentration of ion A in glass relative to the surface concentration, and (after Rothmund and Kornfeld):⁹⁶

$$n = \frac{\partial \ln \bar{a}_A}{\partial \ln C_A},$$

where \bar{a}_A is the thermodynamic activity of the ion A.

This can be solved to obtain the silver concentration profile provided the initial and the boundary conditions are known. One of the boundary conditions involves knowledge of the silver cation concentration at the glass surface. Determination of this boundary condition requires the study of silver kinetics in glass coating and the role of interface.

For many materials, diffusion along grain boundaries may dominate mass transport. However, atomic diffusion across interfaces of fast ionic conductors is usually inhibited by the boundary layer. This interface diffusion problem has been addressed with the aid of one-dimensional lattice gas model generalized by introduction of a finite width interface region with an energy barrier.⁹⁷ This model should be further modified for tin side of the soda-lime float glass by the introduction of interfacial charge transfer reactions such as



Diffusion coefficients of cations are concentration and temperature dependent. The self-diffusion of silver is reportedly by a factor of 4 to 12 times smaller than that of sodium.⁹⁸ The dependence of the self-diffusion coefficient versus temperature satisfies the Arrhenius equation:

$$\check{D} = D_0 \cdot \exp(-Q/kT),$$

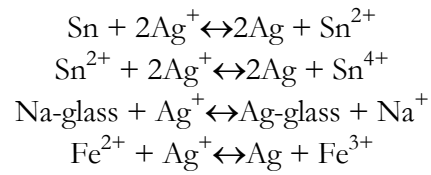
where $D_0 = N \cdot \nu$ (N is the concentration of defects; ν is the vibration frequency of diffusing ion and should lie near the Debye frequency)⁸⁸ and the activation energy; $Q = \Delta G + kT - P \cdot \Delta V$ (P is pressure, ΔV is increase in volume accompanying activation, ΔG is free energy change) is almost constant at low and high temperatures (with discontinuity around glass transition temperature, T_g due to structural changes in glass network) and differentiation between energies of defect formation and migration is hardly possible.

Ion mobilities can be estimated by the Einstein's formula:

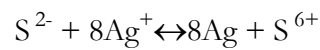
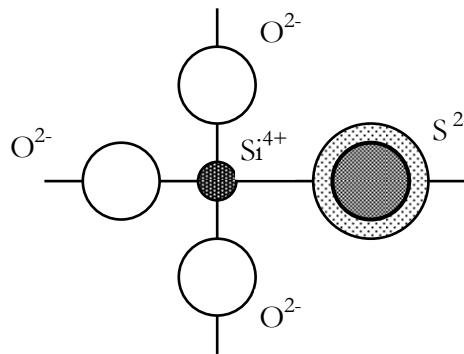
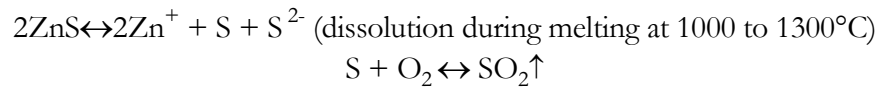
$$\mu = e\check{D} / kT.$$

APPENDIX B:
REFERENCE DATA

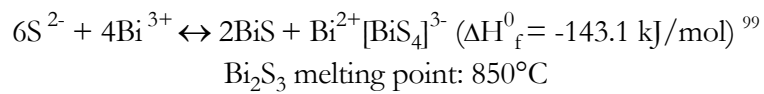
1. SILVER CHEMISTRY



2. SULFUR BARRIER IN ZINC BOROSILICATE FRIT



3. BISMUTH CHEMISTRY



APPENDIX C:
MIE SCATTERING

Mie theory is based on the assumption that particle properties can be described by a single dielectric function of a cluster:

$$\varepsilon(\omega) = \varepsilon_1(\omega) + i \cdot \varepsilon_2(\omega) = 1 + \chi_l(\omega) + \chi_f(\omega) + \chi_{ib}(\omega)$$

$\varepsilon(\omega)$ expresses microscopically the average linear polarization due to lattice, free electron and interband excitations

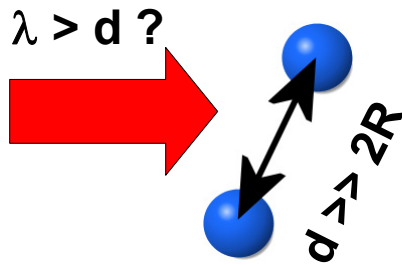
Because of this gravid simplification, the dielectric function of the bulklike cluster material does, in general, not fit in a realistic description. In order to keep the classic electrodynamic (in particular, the Maxwellian boundary conditions) applicable, $\varepsilon(\omega, ..)$ has to be properly modified to include cluster-size and interface effects. Thus, $\varepsilon(\omega)$ in Mie's theory is a phenomenological constant which can be found by developing (quantum theoretical) microscopic models for the properties of a cluster further cumulated in the introduction of proper correction or extension terms into $\varepsilon(\omega, ..)$. This indirect procedure is justified as it makes possible quantitative comparison with experiments on metal clusters of arbitrary sizes.

The theory permits the solution of any scattering and propagation problem, if the four components of the scattering matrix, R are known for each individual particle. Solution can be found for a spherical particle for any polarized and natural light. The matrix R relates the electric field components B in a far field of scattered spherical wave to electric field A of planar incident wave. It is assumed that the optical polarizability tensor is diagonal ($R_3 = R_4 = 0$).

The phenomenological dielectric function of a cluster can be represented as a sum of the real part, $\varepsilon_1(\omega, ...)$ and the imaginary part related to conductance, $\sigma(\omega, ...)$. It is a function of the particle size and in general is determined empirically by the closest fit to experimental data.

The section below gives an outline of computations made to simulate the reflectance curves of silver clusters in soda-lime-silica glass substrate depending on changes in interface area refractive index of glass matrix and the particle size distribution.

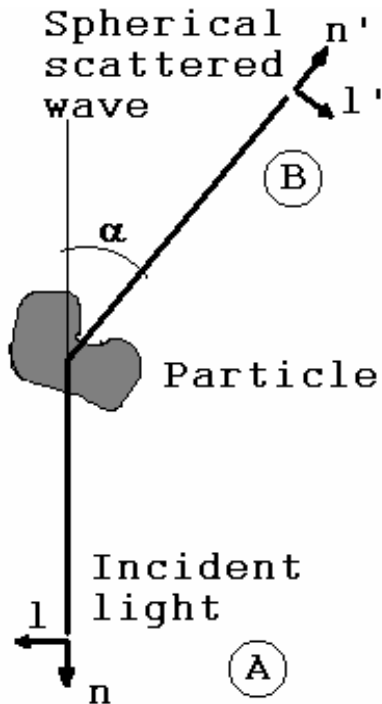
Non-interacting spheres



Neutral metal clusters in molten glasses tend to aggregate into spheres to minimize the surface energy.

If cluster sizes are much smaller than distances between them, they are treated independently.

Project sponsored by dmc² Corporation



r is perpendicular to the plane;

Direct experiment:

$$\begin{bmatrix} B_1 \\ B_r \end{bmatrix} = \begin{bmatrix} R_2 & R_3 \\ R_4 & R_1 \end{bmatrix} \cdot \begin{bmatrix} A_1 \\ A_r \end{bmatrix}$$

$$m = \frac{n(\text{particle})}{n(\text{medium})} = \sqrt{\frac{\epsilon_1(\omega)}{\epsilon_m} + \frac{4 \cdot \pi \cdot \sigma(\omega)}{\omega \cdot \epsilon_m}} \cdot i$$

$$x = \frac{2 \cdot \pi \cdot \rho}{\lambda} \cdot n(\text{medium})$$

Non-diagonal elements of the transformation matrix are approximated by zero and the invariant representations of the incident and the scattered electric field are expressed in form of the Stoke's vector.¹⁰⁰

Phase matrix for transformation of Stoke's vector (van de Hulst, 1957)

$$\begin{bmatrix} I_s \\ Q_s \\ U_s \\ V_s \end{bmatrix} = \frac{1}{k^2 \cdot r^2} \cdot \begin{bmatrix} S_{11} & S_{12} & 0 & 0 \\ S_{12} & S_{11} & 0 & 0 \\ 0 & 0 & S_{33} & S_{34} \\ 0 & 0 & -S_{34} & S_{33} \end{bmatrix} \cdot \begin{bmatrix} I_i \\ Q_i \\ U_i \\ V_i \end{bmatrix}$$

$$R_1 = \frac{S_{11}}{k \cdot r}$$

$$R_2 = \frac{S_{22}}{k \cdot r}$$

$$I = \text{mean} \left[\left(|E_l| \right)^2 + \left(|E_r| \right)^2 \right]$$

$$Q = \text{mean} \left[\left(|E_l| \right)^2 - \left(|E_r| \right)^2 \right]$$

$$U = \text{mean} \left(\overline{E_l \cdot E_r} + \overline{E_r \cdot E_l} \right)$$

$$V = \text{mean} \left(\overline{E_l \cdot E_r} - \overline{E_r \cdot E_l} \right)$$

$$S_{11} = \frac{1}{2} \left[\left(S_2 \right)^2 + \left(S_1 \right)^2 \right]$$

$$S_{33} = \frac{1}{2} \left(\overline{S_2} \cdot S_1 + S_2 \cdot \overline{S_1} \right)$$

$$S_{12} = \frac{1}{2} \left[\left(S_2 \right)^2 - \left(S_1 \right)^2 \right]$$

$$S_{34} = \frac{1}{2} \left(\overline{S_2} \cdot S_1 - S_2 \cdot \overline{S_1} \right)$$

$$S_1 = \sum_n \frac{2 \cdot n + 1}{n \cdot (n + 1)} \cdot (a_n \cdot \pi_n + b_n \cdot \tau_n)$$

$$S_2 = \sum_n \frac{2 \cdot n + 1}{n \cdot (n + 1)} \cdot (a_n \cdot \tau_n + b_n \cdot \pi_n)$$

π_n and τ_n are Associated Legendre Polynomials

$$\pi_0 = 0 \quad \pi_1 = 1 \quad \pi_n = \frac{2 \cdot n - 1}{n - 1} \cdot \cos(\alpha) \cdot \pi_{n-1} - \frac{n}{n - 1} \cdot \pi_{n-2}$$

$$\pi_2 = 3 \cdot \cos(\alpha) \quad \tau_n = n \cdot \cos(\alpha) \cdot \pi_n - (n + 1) \cdot \pi_{n-1}$$

$$a_n = \frac{m \cdot \psi_n(m \cdot x) \cdot \frac{d}{dx} \psi_n(x) - \psi_n(x) \cdot \frac{d}{dx} \psi_n(m \cdot x)}{m \cdot \psi_n(m \cdot x) \cdot \frac{d}{dx} \xi_n(x) - \xi_n(x) \cdot \frac{d}{dx} \psi_n(m \cdot x)}$$

$$b_n = \frac{\psi_n(m \cdot x) \cdot \frac{d}{dx} \psi_n(x) - m \cdot \psi_n(x) \cdot \frac{d}{dx} \psi_n(m \cdot x)}{\psi_n(m \cdot x) \cdot \frac{d}{dx} \xi_n(x) - m \cdot \xi_n(x) \cdot \frac{d}{dx} \psi_n(m \cdot x)}$$

ψ_n and ξ_n are Ricatti-Bessel functions of the first and second kind

The reflectance spectra of predominant size (from 5 to 200 nm) Ag_n clusters in soda-lime glass will shift (ref. Figure 10) with accompanying changes in refractive index of glass surface layer (1.51 to 1.78).

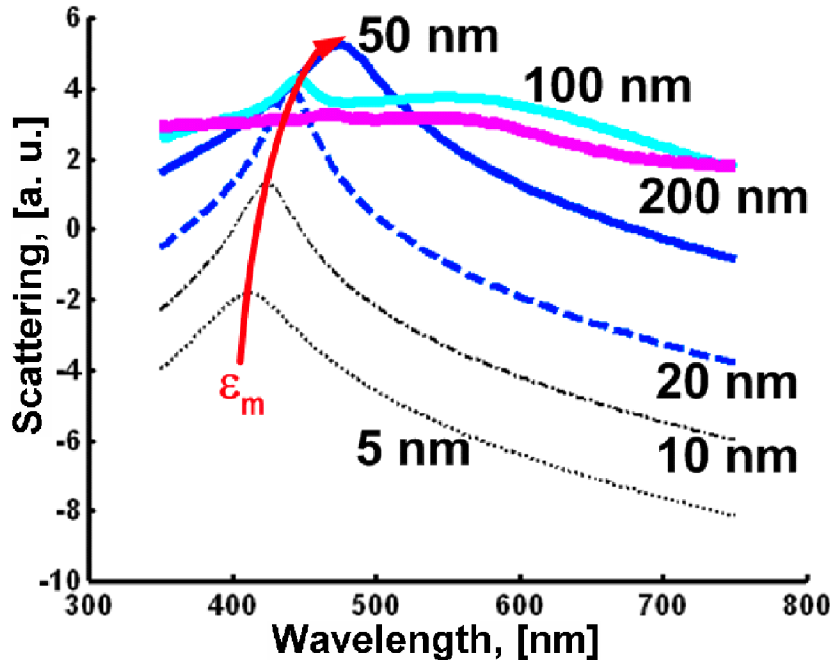


Figure B1. Mie scattering with uniform particle size.

These changes can be explained by the ion-exchange models.⁹³ Mie resonances can also shift due to chemical interface effects such as static charge transfer by chemisorption at a metal cluster surface:¹

$$\omega_s = [N / \epsilon_0 m_{\text{eff}}]^{1/2} [2\epsilon_m + 1 + \chi(\omega)]^{-1/2}$$

(m_{eff} is the effective mass of the charge carriers at the surface).

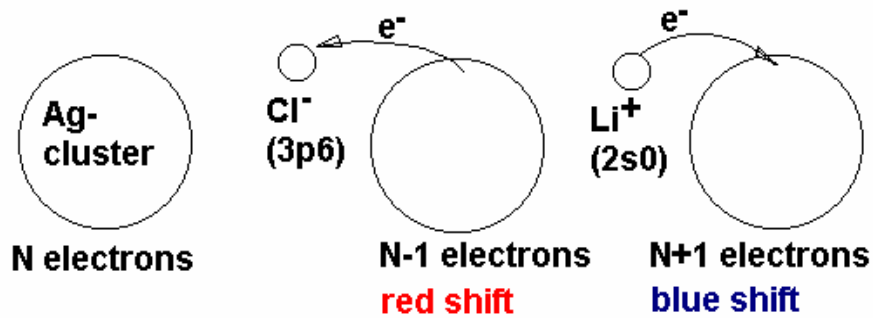


Figure B2. Effect of chemisorption on Mie resonance.

Non-uniform particle size distribution also shifts and broadens the Mie resonances. The figure below illustrates the changes corresponding to half-the-particle-size width of distribution (Lanczos Window simulation).

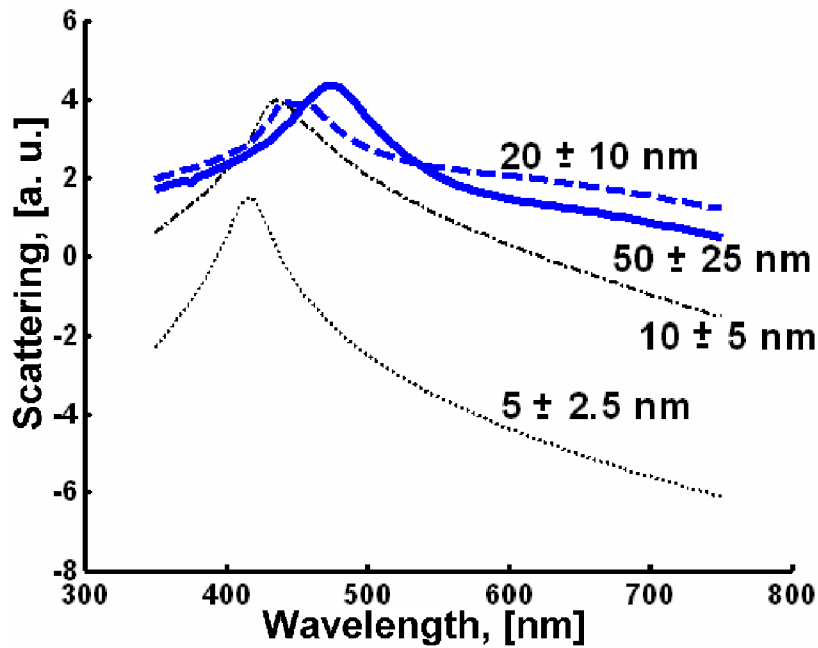


Figure B3. Effect of Particle size distribution on Mie resonance spectrum.

At higher concentrations, the interaction between the particles and multiple light scattering can no longer be ignored. The variations of the optical extinction depending on the aggregate shape, aggregate size, single cluster size, and the neighboring cluster distance have been compiled by Kreibig and Vollmer¹ for Ag clusters, which exhibit the sharpest resonance among all metals.

Figure B4b of the four panel figure below demonstrates that the typical two-peak structure (lowest-order, "in-phase" plasmon polariton modes of the coupled oscillators) is split and shifted towards low frequencies when the length of the chain (N_A) grows.

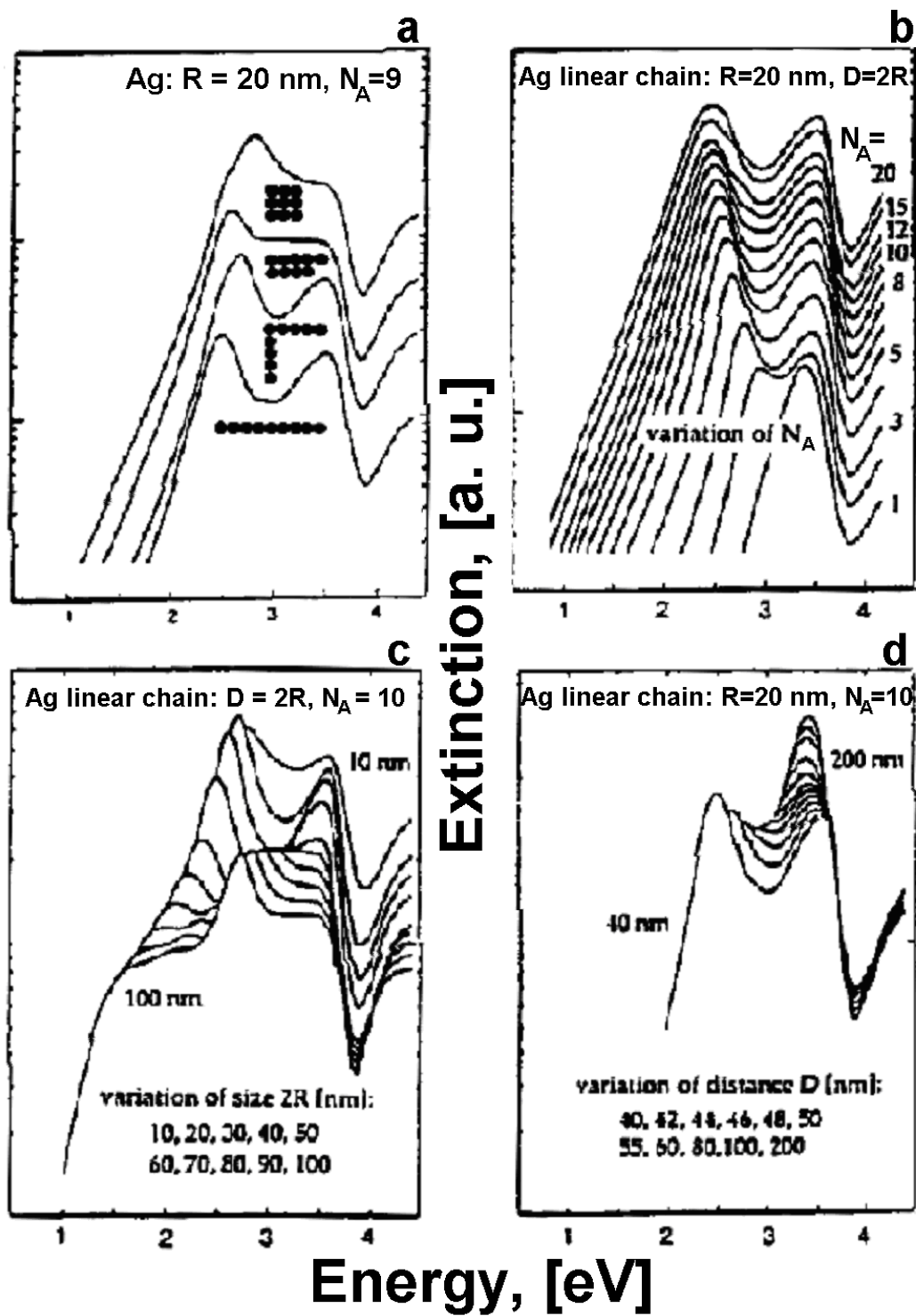


Figure B4. Effect of cluster-cluster interaction on extinction spectrum [from ref. 1].

APPENDIX D: MICROANALYSIS

1) Spatial resolution for a typical SEM collimator lens:

$$\text{CuK}\alpha_1 := 1.54051$$

$$\text{CuK}\alpha_2 := 1.54433$$

$$\Delta\lambda_0 := 0.05$$

$$\lambda_0 := \frac{2 \cdot \text{CuK}\alpha_1 + \text{CuK}\alpha_2}{3}$$

$$\Delta E := \frac{12396 \cdot \Delta\lambda_0}{(\lambda_0)^2}$$

$$eV := 20000$$

$$E := \frac{12396}{\lambda_0} + eV$$

$$\lambda := \frac{12396}{E}$$

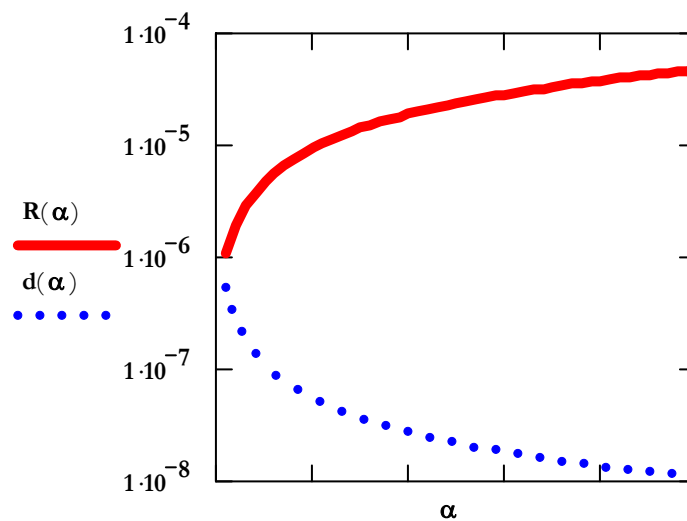
$$C_c := 1 \quad (\text{chromatic aberration})$$

$$C_s := 1.8 \quad (\text{spherical aberrations})$$

$$\alpha := 0.0001, 0.0002 \dots 0.005$$

$$d(\alpha) := \frac{1.22 \cdot \lambda \cdot 10^{-10}}{\sin(\alpha)}$$

$$R(\alpha) := \sqrt{\left(\frac{1.22 \cdot \lambda \cdot 10^{-10}}{\sin(\alpha)}\right)^2 + \left[\left(\frac{\Delta E}{E} C_c\right) \cdot \alpha\right]^2 + \left(\frac{1}{2} \cdot C_s \cdot \alpha^3\right)^2}$$



2) XRD line broadening

x is the distance from the position of the peak

$f(x)$ is the intensity of line broadened by diffraction

$g(x)$ is the intensity from instrumental broadening

$$h(q) = \int_{-\infty}^{\infty} f(x) \cdot g(q - x) dx$$

$$(\sigma_h)^2 = (\sigma_f)^2 + (\sigma_g)^2$$

$$2 \cdot \sigma_x \cdot \cos(\theta) = K_1 \cdot \frac{\lambda}{L} \quad \text{for x'tal broadening:} \quad L = \sqrt[3]{\text{volume}}$$

$$2 \cdot \sigma_s \cdot \cot(\theta) = K_2 \quad \text{for strain broadening:}$$

$$\delta\theta = - \left(\frac{\delta d}{d} \right) \cdot \tan(\theta)$$

$$(\sigma_f)^2 = (\sigma_x)^2 + (\sigma_s)^2$$

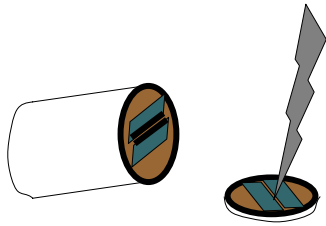
$$4 \cdot (\sigma_f)^2 \cdot (\cos(\theta))^2 = \left(K_1 \cdot \frac{\lambda}{L} \right)^2 + \left(K_2 \cdot \sin(\theta) \right)^2$$

3)

TEM microscopy (Surface Science Center)

Sample preparation:

- ✓ Glass in copper tube
- ✓ Epoxy
- ✓ Cut off disks
- ✓ Grind out the center



Observations:

- ✓ Uniform Ag particle distribution near enamel-substrate interface
- ✓ Particle sizes range from 10 nm to 15 nm

APPENDIX E:

Visual Basic code for electro-chemical diffusion (file attached)

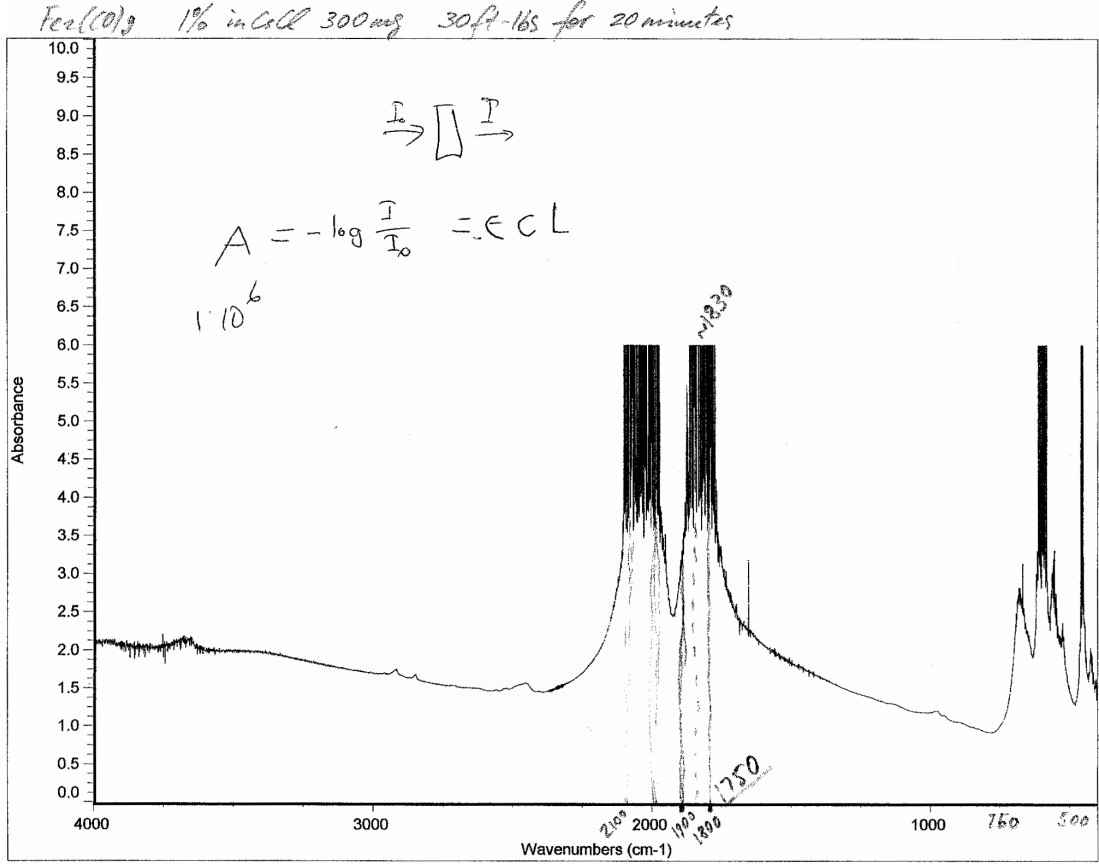
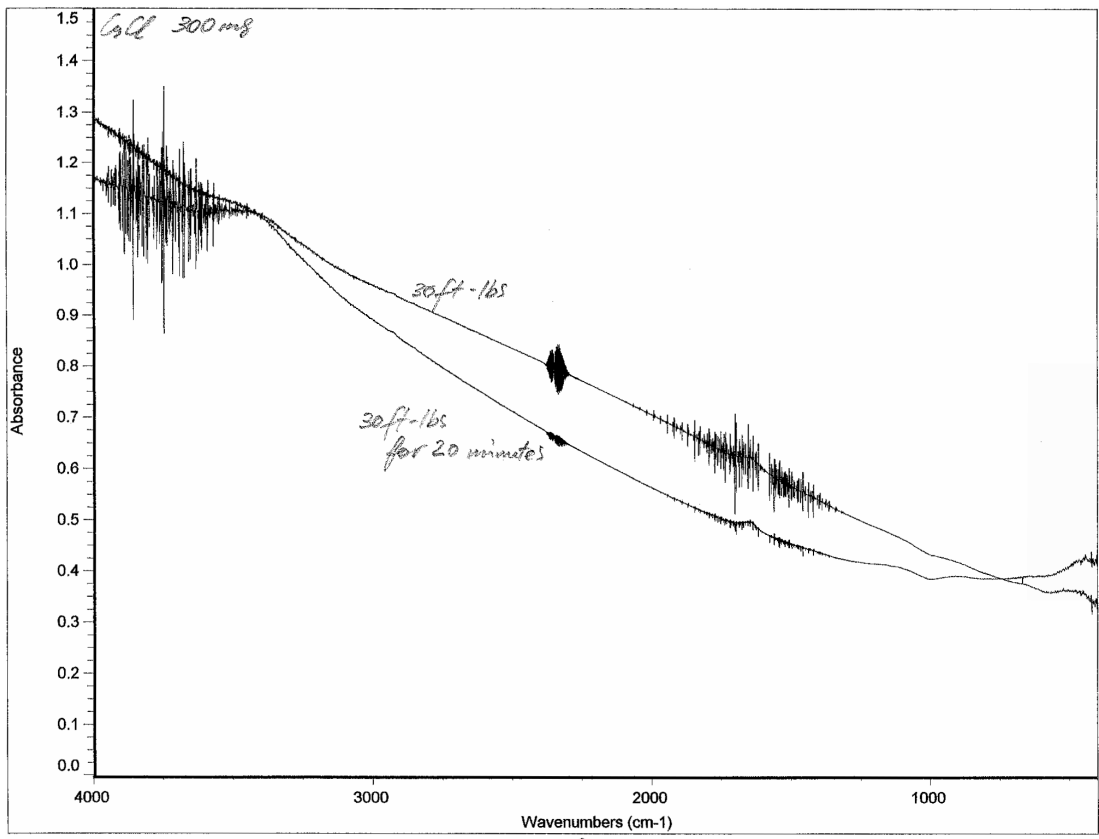
APPENDIX F:

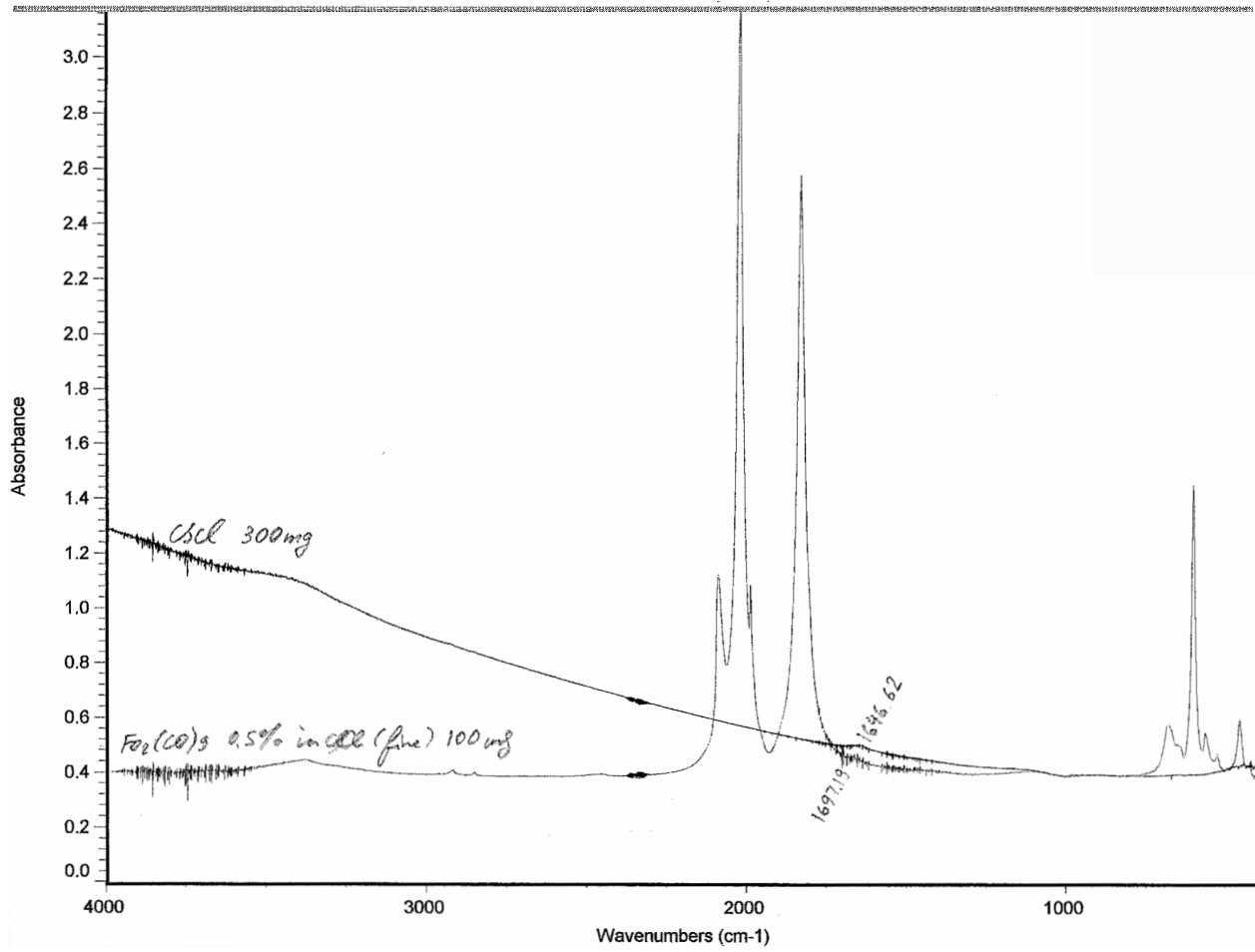
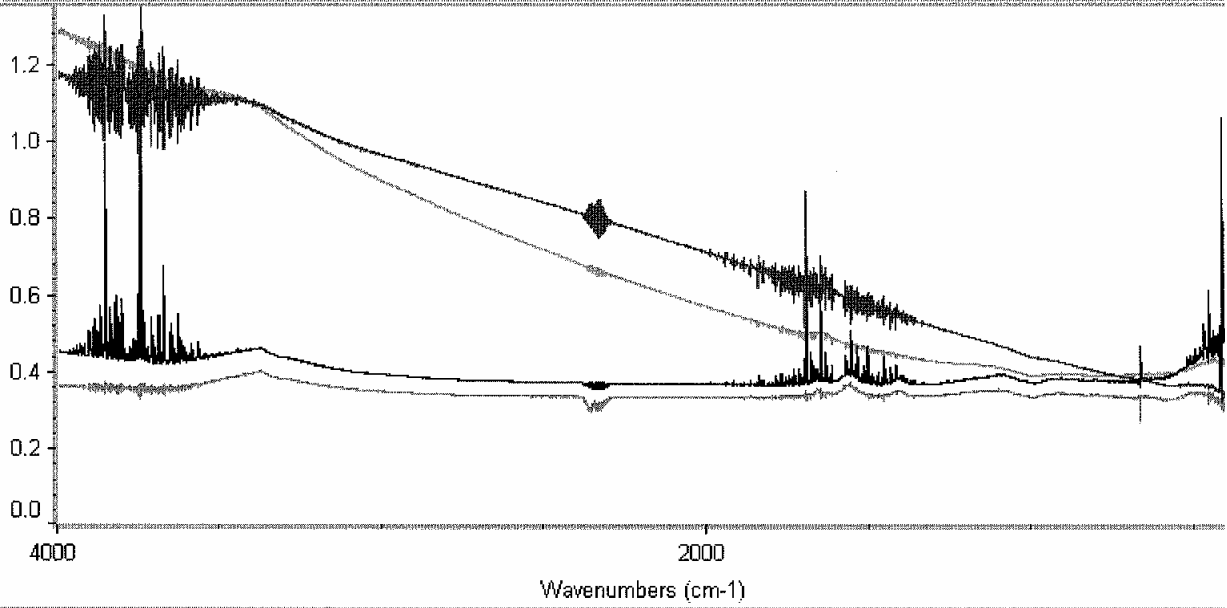
Infrared Transmittance of Di-iron Nonacarbonyl

Dry solid flakes of $\text{Fe}_2(\text{CO})_9$ (Aldrich, 99.5% pure) and the IR transparent filler (CsCl, KBr, or CsI) were ground separately with agate mortar and pestle and then mixed together and pressed into ≤ 0.5 mm thick pellets. The mixture (~ 100 mg) was pressed for 5 to 40 minutes at up to 40 N·m (30 ft-lb). IR transmission spectra were collected by the AVATAR 360 FT-IR E.S.P. spectrometer, with resolution of 0.5 cm^{-1} (two data points per division), within spectral range of 400 to 4000 cm^{-1} . The quality of the spectra was optimal for the sample preparation procedure described in Chapter 7. Excessive grinding of the matrix powder resulted in higher level of absorbed moisture and very noisy spectra. Insufficiently fine particles contributed to the increased extinction of the shorter wavelengths. Decrease in torque and in pressing time (below 20 minutes) produced opaque non-cohesive pellets with significant distortion of the extinction spectrum, similar to the transmittance and reflectance spectra collected by Adams and Taylor.¹¹¹ No cooperative effects were observed for the analyte concentrations below 1%.

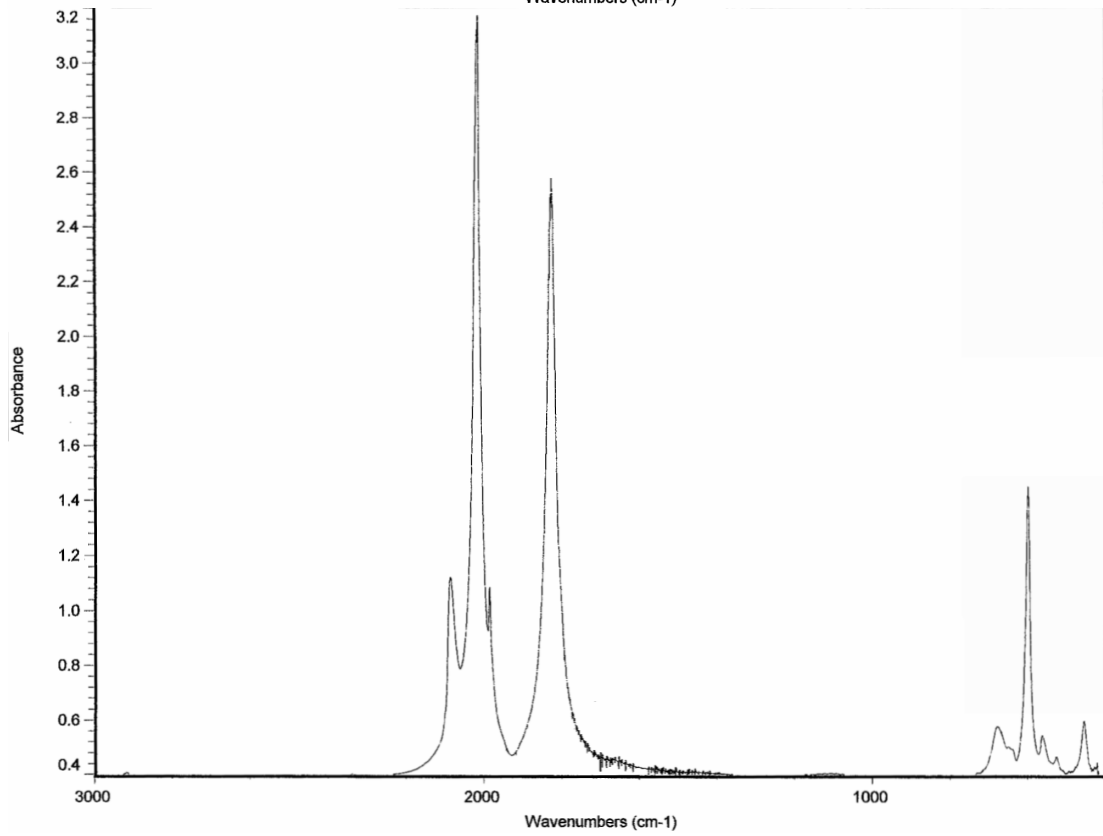
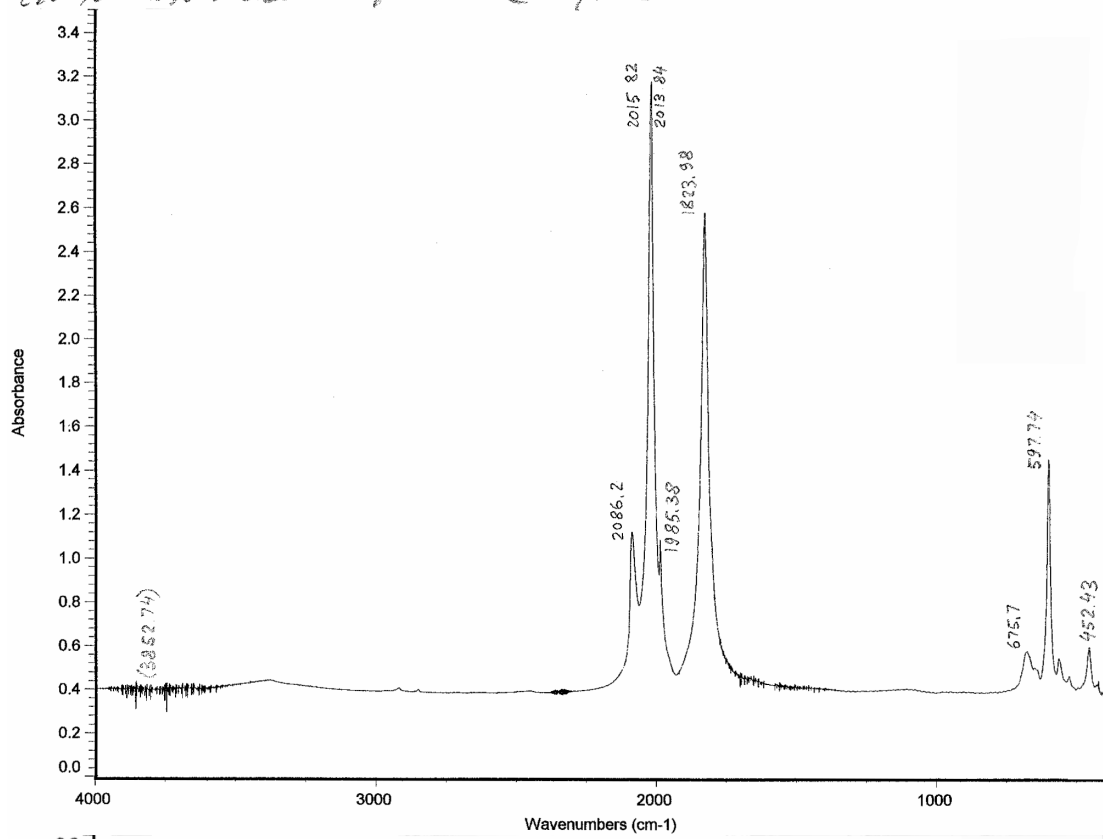
Alternative explanation of the side bands in the Adams and Taylor spectra – other than poor sample preparation technique – can be found in the filler powder contamination. Acidic H-bonds could account for a broad peak at $\sim 1730\text{ cm}^{-1}$, asymmetric broadening of the bridging band can be attributed to acyl halides, and RCOOH could contribute to the shorter wavelength dispersion.

The experimental infrared spectra collected during this research study are reported below.

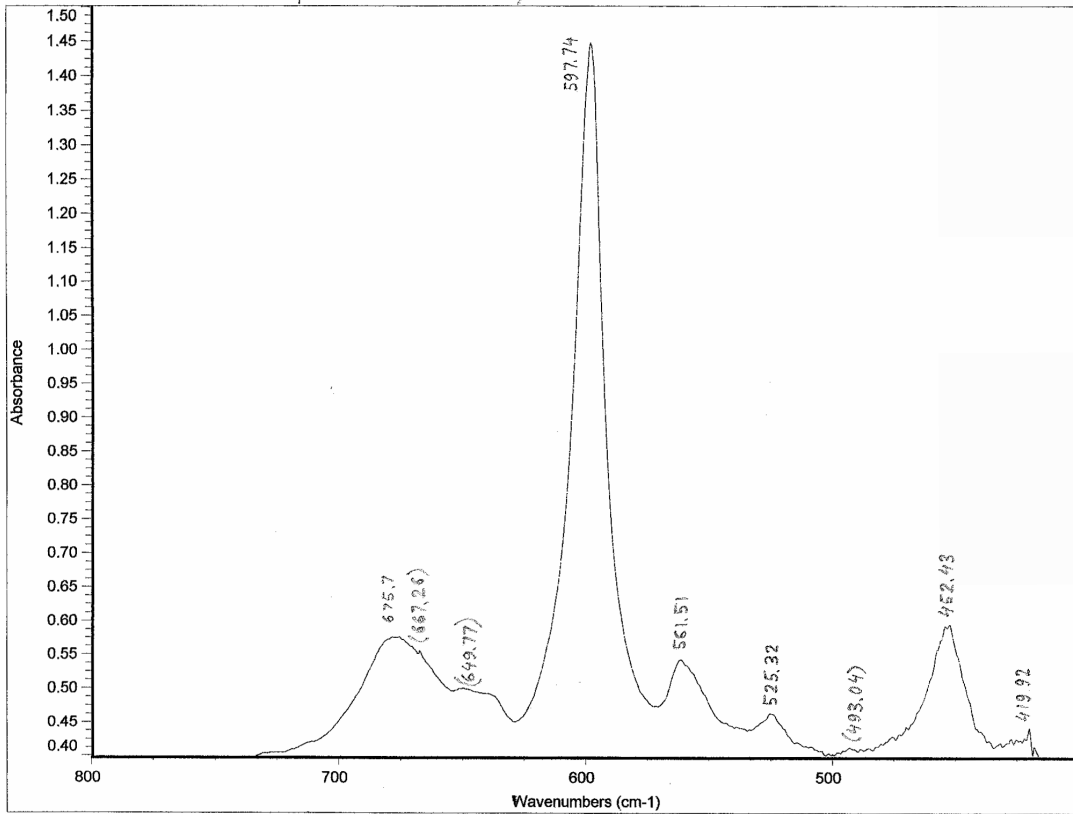




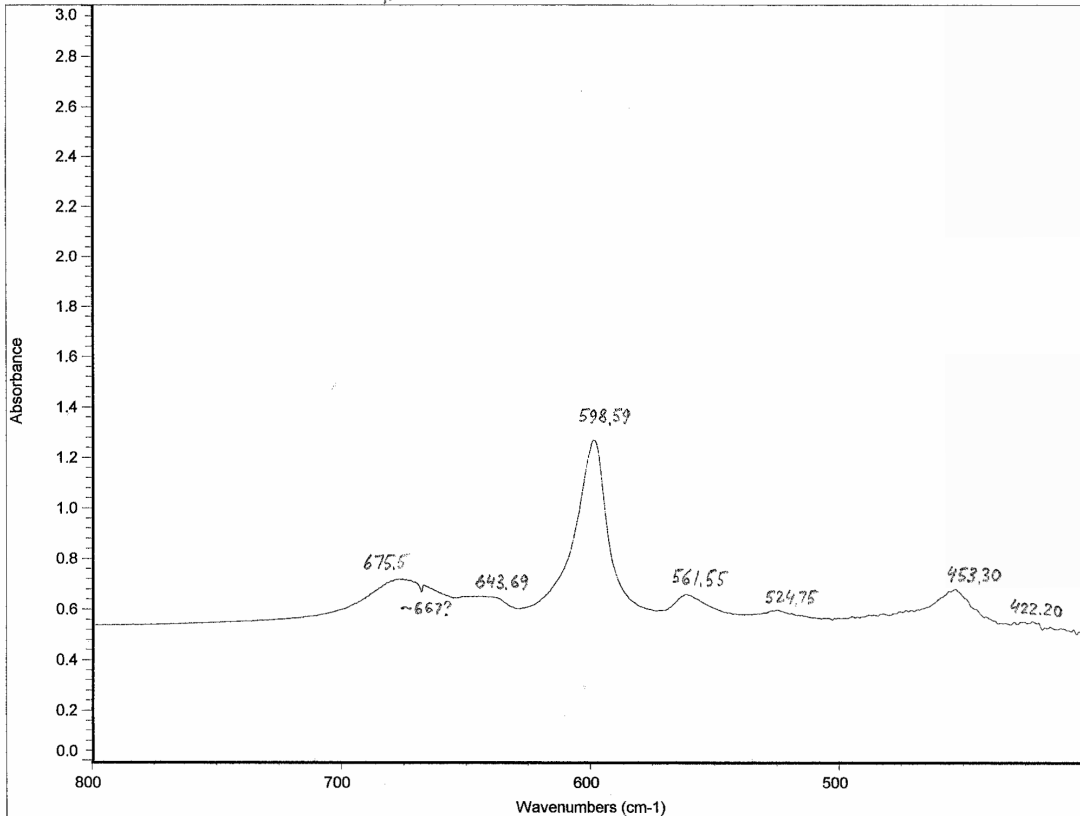
$Fe_2(CO)_9$ 0.5% in Cell 100 mg 30 min @ 30 ft-lbs



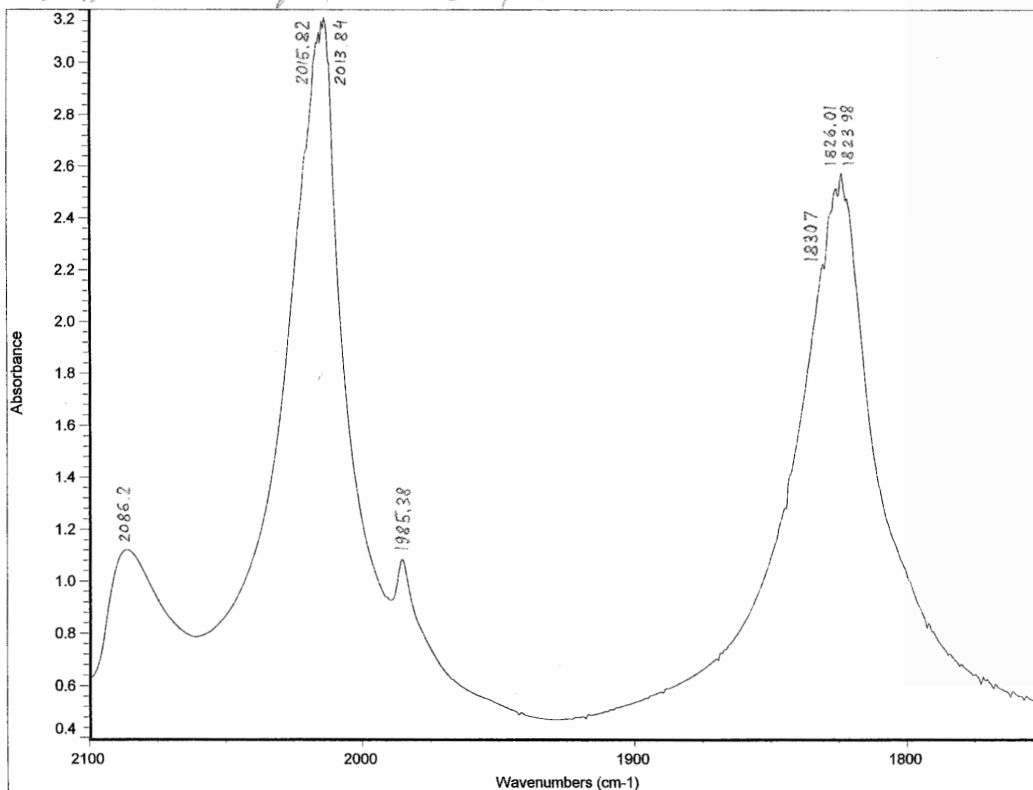
Fe₂(CO)₉ 0.5% in CCl₄ (fine) 30 min @ 30 ft-lbs



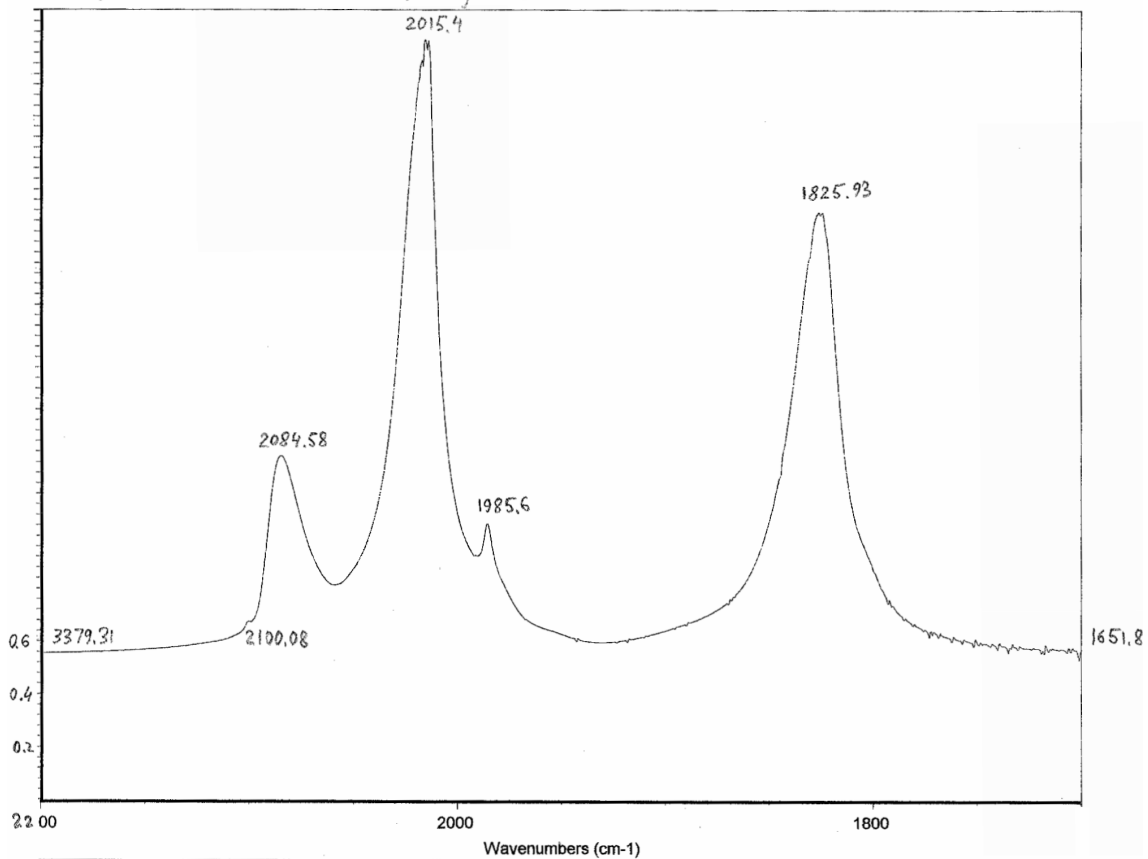
Fe₂(CO)₉ 0.25% in C₆H₆ 30 min @ 40 ft-lbs



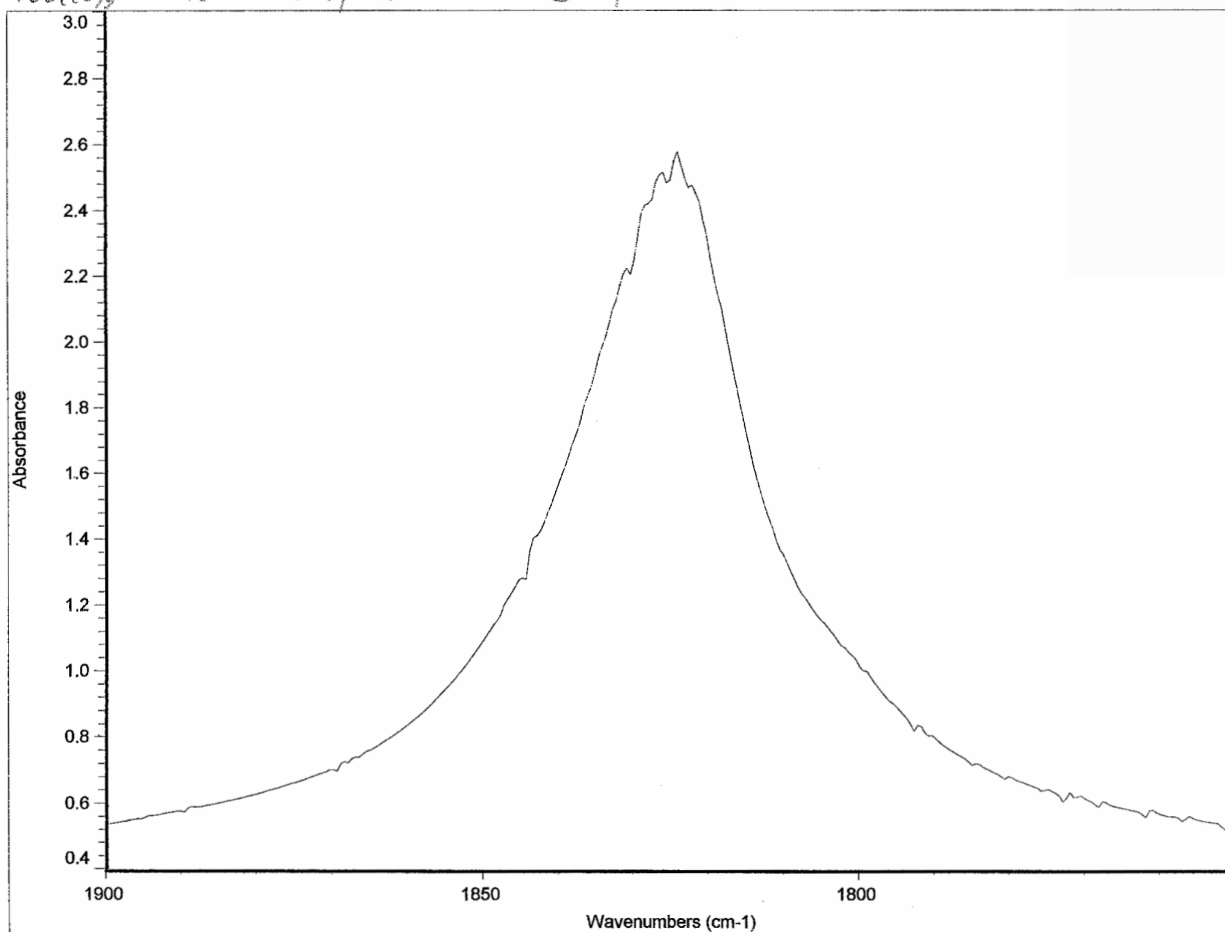
$Fe_2(CO)_9$ 0.5% in CS_2 (fine) 30 min @ 30 ft-lbs



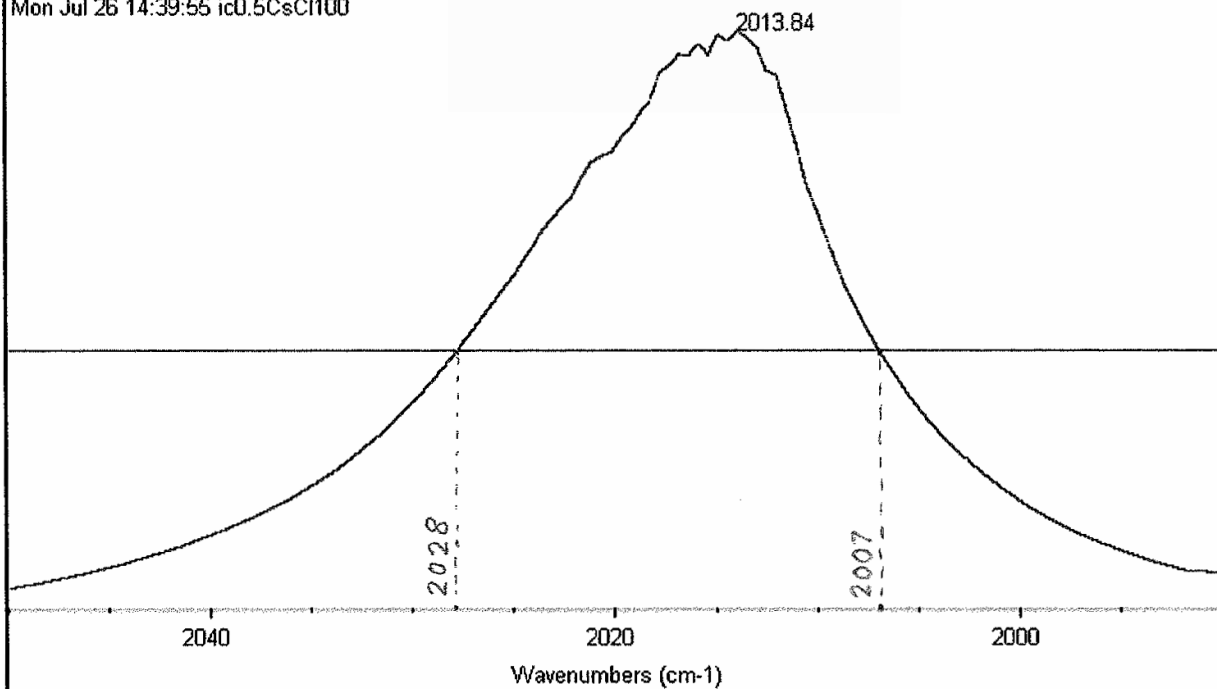
$Fe_2(CO)_9$ 0.25% in C_2Cl_4 30 min @ 40 ft-lbs



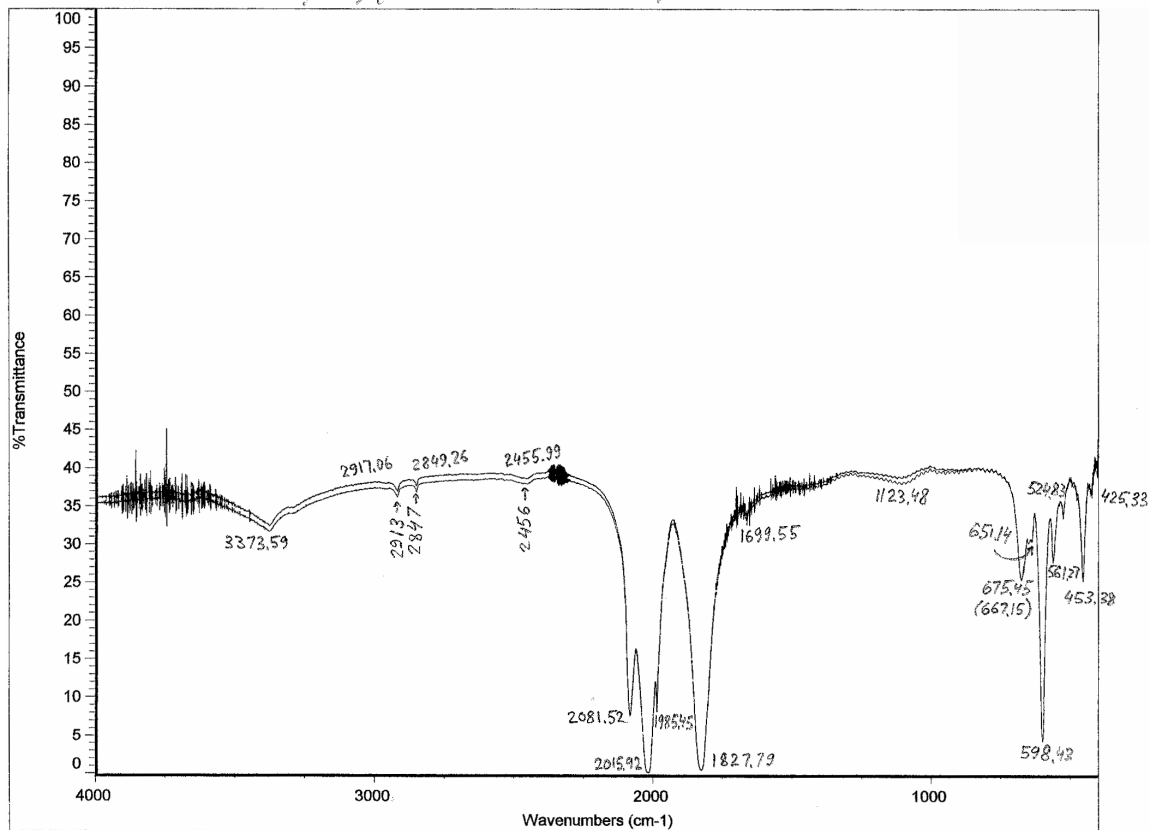
Fe₂(CO)₉ 0.5% in CsCl (fine) 30 min @ 30 ft-16s



Mon Jul 26 14:39:55 ic0.5CsCl100

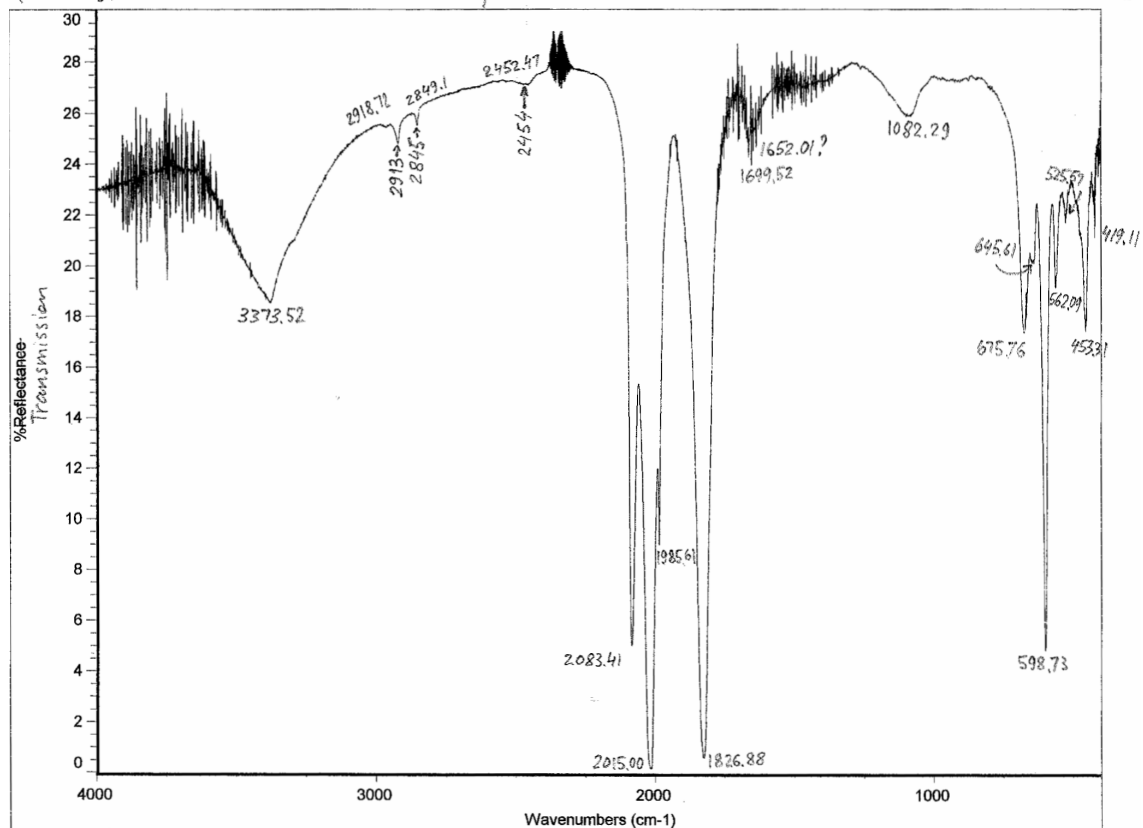


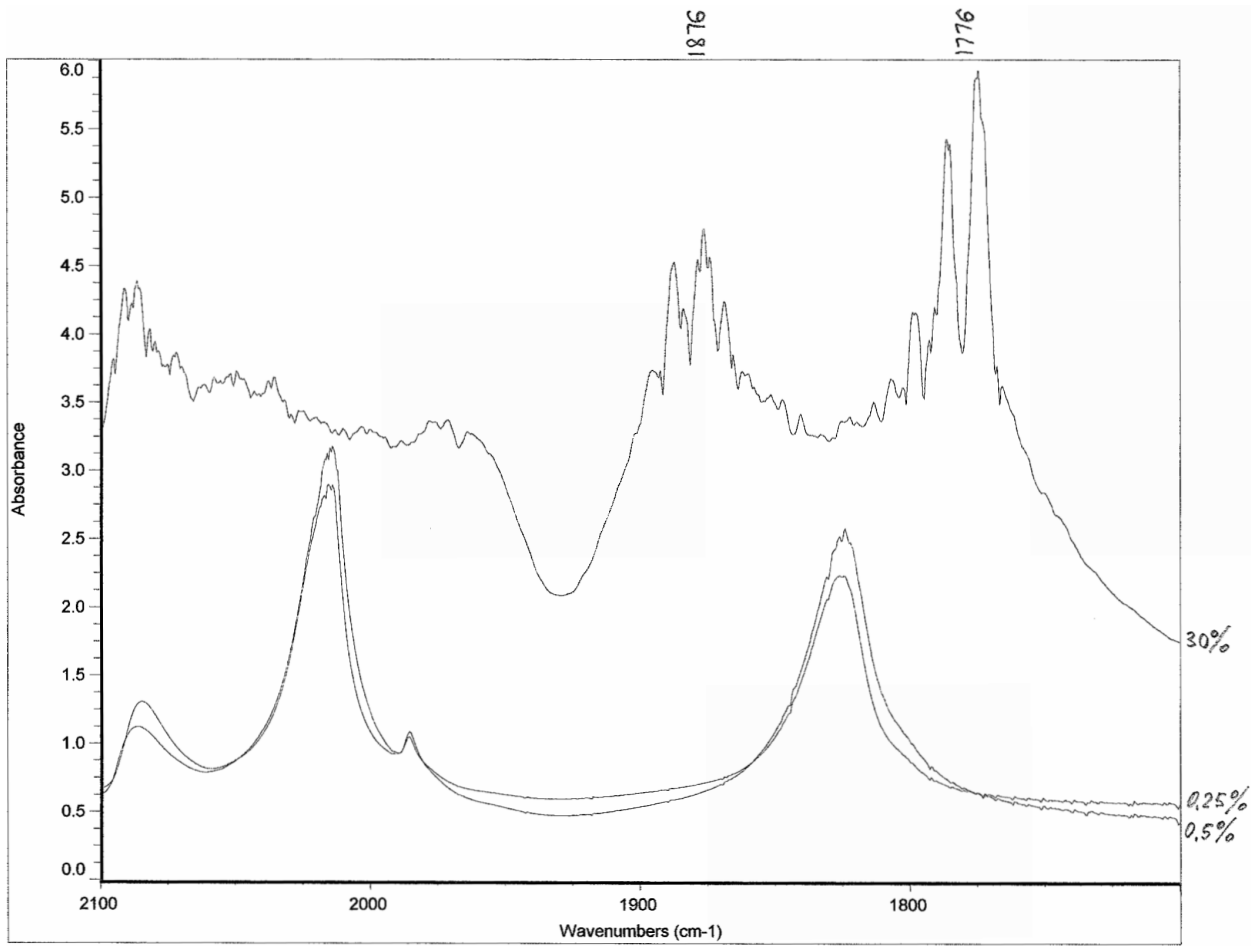
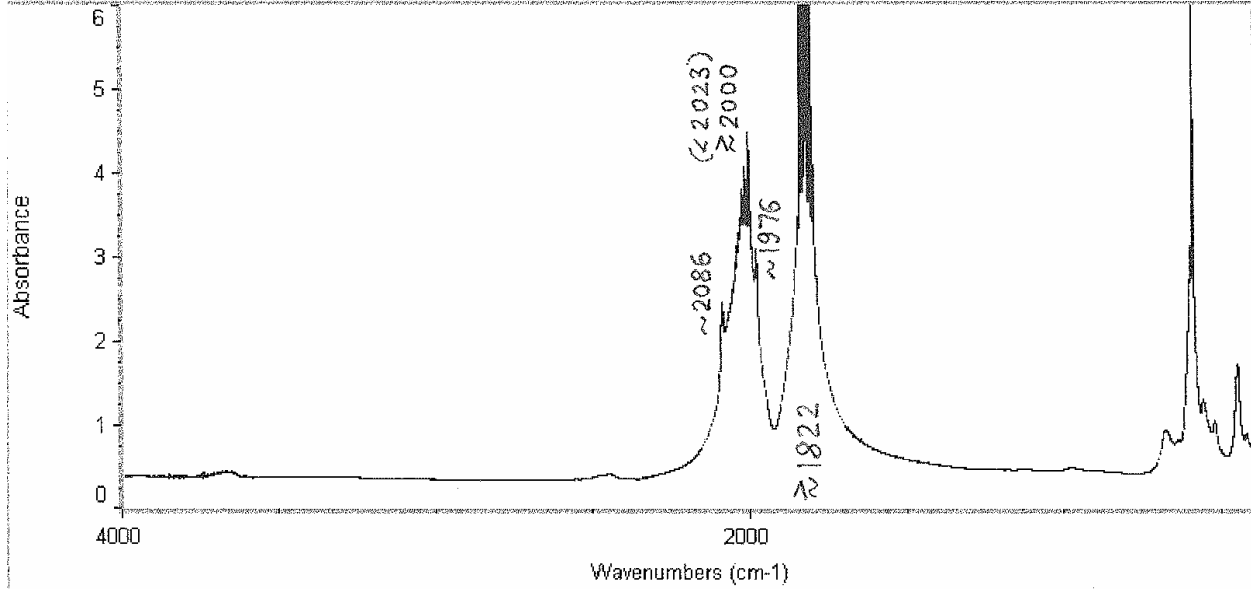
$Fe_2(CO)_9$ 0.5% in CCl (finely ground) 30 min @ 30ft-16s



$(Fe_2(CO)_9) - 0.25%$ in CCl 30 min @ 40ft-16s

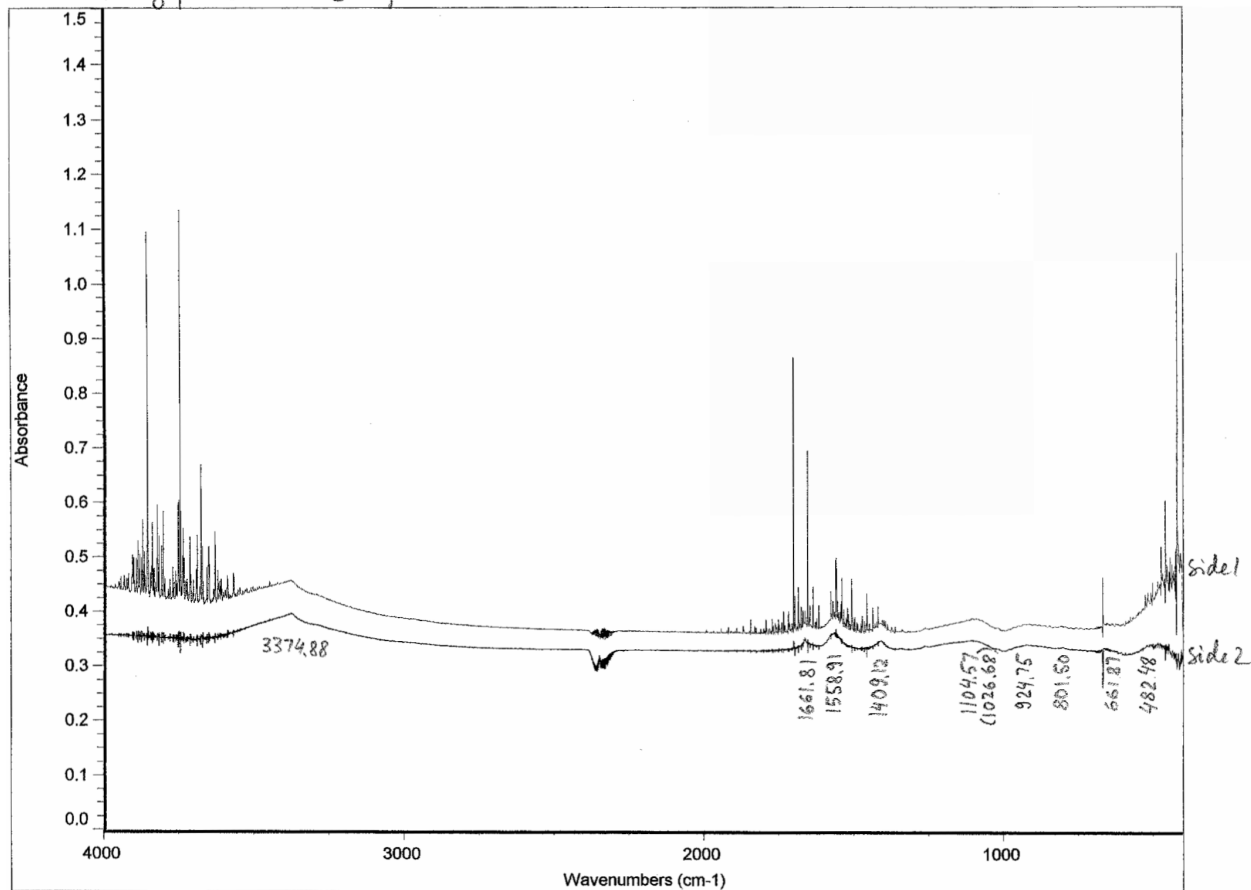
CO_2





CsCl 100mg pellet 1hr @ 40ft-lbs

CO₂ + H₂O



APPENDIX G:

Matlab 5.0 and Matlab 7.0 codes (files attached)

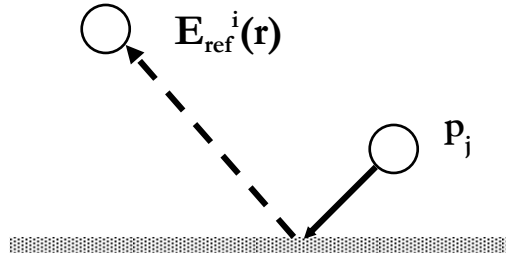
APPENDIX H:

Numerical Electromagnetic Code simulations

In a coupled-dipole method, an array of dipole moments \mathbf{P} is found from the matrix equation:

$$\mathbf{A}\mathbf{P} = \mathbf{E}, \quad (\text{H1})$$

where \mathbf{E} is the total field at each dipole and \mathbf{A} is the interaction matrix, which is simply the inverted polarizability matrix α in this case, since $\mathbf{P} = \alpha \bullet \mathbf{E}$.



In presence of the surface the interaction matrix must be modified to account for the reflection of the dipole waves from the surface; and the electric field \mathbf{E} becomes a standing wave. Thus,

$$\mathbf{A}_{ii} = 1/\alpha - \mathbf{R}_{ii}, \quad (\text{H2})$$

$$\mathbf{A}_{i \neq j} \bullet \mathbf{P}_j = -(E_{ij} + \mathbf{R}_{ij}), \quad (\text{H3})$$

where \mathbf{R} represents the reflected dipole wave;¹²⁹

$$E_{ij}(r) = k^2 (n_{ij} \times P_j) \times n_{ij} \frac{\exp(ikr)}{r} + [3n_{ij} (n_{ij} \bullet P_j) - P_j] \left(\frac{1}{r^3} - \frac{ik}{r^2} \right) \exp(ikr), \quad (\text{H4})$$

n_{ij} is the unit-direction vector and k is the wave number of the incident radiation.

Major additions in NEC-2 are the Numerical Green's Function, $\overline{\overline{G}}(\vec{r}, \vec{r}')$ for partitioned-matrix solution and a treatment for lossy grounds that is accurate for the scattering object very close to the ground surface.

Integral equation for free space

$$(\alpha_i)^{-1} \bar{P}_i - \bar{E}_{direct,i} - \bar{E}_{reflect,i} = \bar{E}_{inc,i}$$

$$\bar{E}_{direct,i} = \frac{k^2}{\epsilon_0} \cdot \sum_{j \neq i} \bar{G}_{ij} \cdot \bar{P}_j$$

$$\bar{E}_{reflect,i} = \sum_{j=1}^N \left(\frac{k^2 \cdot (k_s^2 - k^2)}{\epsilon_0 \cdot (k_s^2 + k^2)} \cdot \bar{G}_{ij}^I + \underbrace{\bar{S}_{ij}}_{\text{Lager \& Lytle}} \right) \bar{P}_j$$

Sommerfeld
integrals

$$\bar{G}(\bar{R}) = \frac{e^{i(\bar{k} \cdot \bar{R})}}{4\pi R} \cdot \left\{ \left[1 - (\bar{k} \cdot \bar{R})^{-2} + i(\bar{k} \cdot \bar{R})^{-1} \right] \cdot \bar{I} - \left[1 - (\bar{k} \cdot \bar{R})^{-2} + 3i(\bar{k} \cdot \bar{R})^{-1} \right] \cdot e_R e_R \right\}$$

$$\bar{G}_{ij}^I = -\bar{G}(\bar{r}_i - \bar{I}_R \cdot \bar{r}_j)$$

$$\bar{I}_R = e_x e_x + e_y e_y - e_z e_z$$

$$(\bar{B} + \bar{A} + \bar{R}) \otimes \bar{P} = \bar{E}_{inc}; \bar{P} = [\bar{P}_1, \dots, \bar{P}_N]^T; \bar{E}_{inc} = [\bar{E}_{inc,1}, \dots, \bar{E}_{inc,N}]^T$$

NEC2 Fresnel Reflection

- The Numerical Electromagnetic Code (Lawrence Livermore Lab) computes response of metal structures above the ground
- NEC2 options: large smooth surfaces and lossy ground for structures that are very close to it
- Sommerfeld integral solution is most accurate for distances less than one wavelength but it is very time consuming
- The modified image method for lossy grounds provides useful results by use of the Fresnel plane-wave reflection coefficients

The Fresnel far zone approximation:

- The reflection coefficient method for finitely conducting ground uses the image fields modified by the Fresnel reflection coefficients:

$$\vec{E}_{sca}(\vec{r}) = \frac{k^2}{\epsilon_0} \cdot \frac{e^{i(\vec{k} \cdot \vec{r})}}{4\pi r} \cdot \mathcal{P} \quad (H5)$$

$$\mathcal{P} = \sum_j \left\{ e^{i(\vec{k}_{sca} \cdot \vec{r}_j)} \cdot \left[(\vec{p}_j^* \cdot \vec{e}_1) \vec{e}_1 + (\vec{p}_j^* \cdot \vec{e}_2) \vec{e}_2 \right] \right. \\ \left. + e^{-i(\vec{k}_{I,sca} \cdot \vec{r}_j)} \cdot \left[R^{TM} (\vec{p}_j^* \cdot \vec{e}_1) \vec{e}_1 + R^{TE} (\vec{p}_j^* \cdot \vec{e}_2) \vec{e}_2 \right] \right\}$$

$$\vec{k}_{I,sca} = \vec{k}_{sca} \cdot \vec{I}_R$$

- Specular reflection does not always accurately describe near field behavior (reradiated field is not a plane wave) but gives the correct far zone field;
- Attraction of the method is simplicity and speed of calculation.

The double-precision NEC2D codes, originally developed by Lawrence Livermore Laboratories, and the windows utility for source decks generation and output viewing (4NEC2, version 5.3.9 by Arie Voors, 4nec2@gmx.net) are available from the NEC archives maintained by Raymond Anderson (WB6TPU, raymonda@ieee.org).

The NEC-2 simulation of the near field response of the cantilever tip-surface system involves several major computational tasks:

- ✚ Generation of the structure geometry input cards.

⇒ Define the shapes, positions (center coordinates), and angular orientations of the surface patches for a sphere sitting on a flat ground:

- a) Parameters of the initial 20 surface patches (SP cards):

shape	x	y	z	elevation	azimuth	area
arbitrary	0.13795	0.13795	1.98079	78.75	45	0.11957
arbitrary	0.51328	0.21261	1.83147	56.25	22.5	0.17025
arbitrary	0.21261	0.51328	1.83147	56.25	67.5	0.17025
arbitrary	0.80314	0.2152	1.55557	33.75	15	0.16987
arbitrary	0.58794	0.58794	1.55557	33.75	45	0.16987
arbitrary	0.2152	0.80314	1.55557	33.75	75	0.16987
arbitrary	0.96194	0.19134	1.19509	11.25	11.25	0.15028
arbitrary	0.81549	0.5449	1.19509	11.25	33.75	0.15028
arbitrary	0.5449	0.81549	1.19509	11.25	56.25	0.15028
arbitrary	0.19134	0.96194	1.19509	11.25	78.75	0.15028
arbitrary	0.13795	0.13795	0.01921	-78.75	45	0.11957
arbitrary	0.51328	0.21261	0.16853	-56.25	22.5	0.17025
arbitrary	0.21261	0.51328	0.16853	-56.25	67.5	0.17025
arbitrary	0.80314	0.2152	0.44443	-33.75	15	0.16987
arbitrary	0.58794	0.58794	0.44443	-33.75	45	0.16987
arbitrary	0.2152	0.80314	0.44443	-33.75	75	0.16987
arbitrary	0.96194	0.19134	0.80491	-11.25	11.25	0.15028
arbitrary	0.81549	0.5449	0.80491	-11.25	33.75	0.15028
arbitrary	0.5449	0.81549	0.80491	-11.25	56.25	0.15028
arbitrary	0.19134	0.96194	0.80491	-11.25	78.75	0.15028

b) Mirror reflections in the XZ and YZ coordinate planes (GX card);

c) Scale structure dimensions (GS card) ;

d) End geometry input (GE card).

⇒ Calculate the geometry parameters for the spheres at the various distances, z (nm) from the surface: 0.05, 0.1, 0.2, 0.3, 0.4, 0.5, 0.6, 0.7, 0.8, 0.9, 1, 1.2, 1.4, 1.6, 1.8, 2, 2.5, 3, 4, 5, 7, 10, 20, 30, 50, 70, 100, 200, and 700.

⇒ Fill out all geometry cards according to the procedure described above.

✚ Specification of the frequency sets: 1800 cm^{-1} (or 1750 cm^{-1}) to 1900 cm^{-1} with a step of 1 cm^{-1} near the critical points and $2\text{-}5 \text{ cm}^{-1}$ away from the resonance.

✚ Computation of the real and imaginary terms of the dielectric function of the lossy ground.

⇒ Specify the roughness parameter (rms or equivalent radius of curvature) of the gold substrate: bulk (very smooth surface), 0.4 nm, 0.3 nm, 0.2 nm, 0.1 nm.

- ⇒ Compute the dielectric function of the substrate as a function of frequency.
- ⇒ Specify the values of the high frequency limit of the dielectric constant of the sample (iron carbonyl), ϵ_∞ : 1.0, 1.5, 1.8, 1.9, 2.0, 2.1, 2.2, 2.4, and 3.0.
- ⇒ Simulate the infrared extinction (transmission experiment) spectra of iron carbonyl with the specified values of ϵ_∞ and find the fit parameters for the vibrational oscillators (454 cm^{-1} , 600 cm^{-1} , 675 cm^{-1} , 1826 cm^{-1} , 2012 cm^{-1} , 2018 cm^{-1} , 2086 cm^{-1}).
- ⇒ Generate the ground parameters (GN cards) for each frequency from 1800 cm^{-1} to 1900 cm^{-1} : ground-type flag (finite ground, reflection-coefficient approximation or Sommerfeld/Norton method), number of wires in the ground screen (0), real and imaginary parts of the dielectric function (the imaginary part is converted to conductivity). Alternatively, in the wires model, the substrate properties can be specified in the additional ground (GD) card (should not be used with patches).
- ✚ Generation of the excitation cards: source type (incident plane wave, linear polarization); number of the elevation and azimuth angles; maximum relative admittance matrix asymmetry for network connections (no action); elevation (70°, 75°, or 80°), azimuth (0), and polarization angle (0 for p-polarized wave).
- ✚ Specification of the radiation pattern sampling parameters, and the program execution (RP cards): space-wave fields are computed (normal mode, far-field pattern), number of field points (elevation and azimuth), output format (power gain: vertical, horizontal, and total; no normalized gain; no averaging), radial distance from the origin (1 m).
 - ⇒ Before program execution, the data-card deck has to be arranged in the following order: CM (comment cards), CE (end of comments), SP, GX, GS, GE, EX, GN, FR, RP, and NX (next structure card).
- ✚ Saving and reading the NEC output.

- ⇒ All card decks need to have the same number of comment cards in order to enable the output file for easy reading with macros.
- ⇒ The output file can be opened with Microsoft Excel (Fixed width; File origin: 437; manually set field widths).
- ⇒ A macro is generated for transferring the data into convenient Excel data tables and elimination of the data links.

✚ Output data manipulation: the Microsoft Excel data tables are transferred into Matlab environment and converted into matrices.

- ⇒ The rows and columns of the multi-dimensional matrices are interpolated to desired accuracy by the piecewise cubic Hermite interpolation polynomial function, `pchip()`.

✚ Fourier integration of the interpolated data matrices for the relevant wavelengths.

- ⇒ Set the integration interval boundaries: 0.025 nm, 0.075 nm, 0.15 nm, 0.25 nm, 0.35 nm, 0.45 nm, 0.55 nm, 0.65 nm, 0.75 nm, 0.85 nm, 0.95 nm, 1.1 nm, 1.3 nm, 1.5 nm, 1.7 nm, 1.9 nm, 2.2 nm, 2.75 nm, 3.5 nm, 4.5 nm, 6 nm, 8 nm, 14 nm, 25 nm, 40 nm, 60 nm, 80 nm, 150 nm, 300 nm, 700 nm.

- ⇒ Set the reference gold surface (enter the data file name).

- ⇒ Set the fudge factors:

- a) Background noise (0.2);
- b) Substrate reflectivity due to surface roughness correction;
- c) The effective set point of the cantilever oscillation (see Chapter 10, Equation 22).

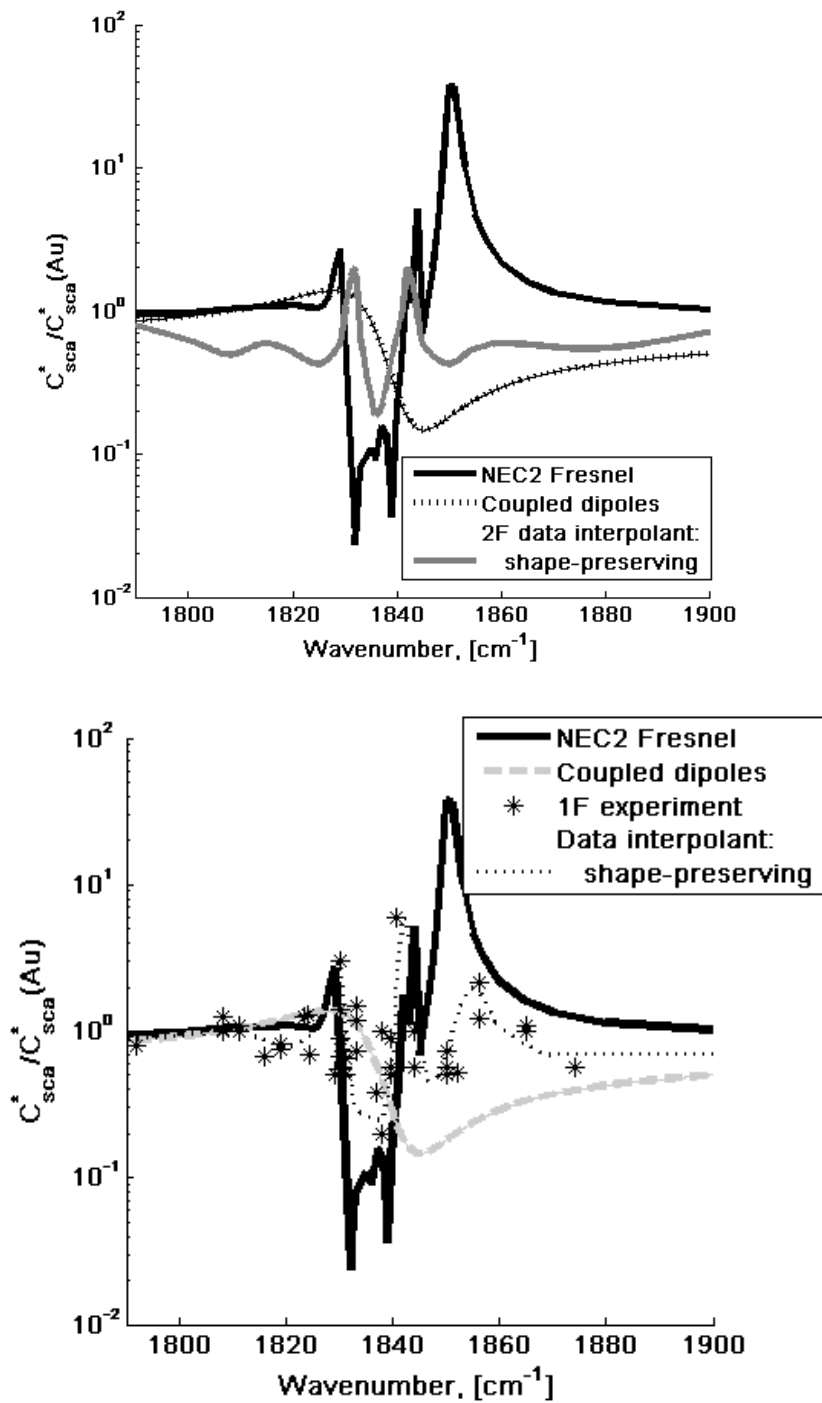
- ⇒ Set parameters of the instrument function (bandwidth).

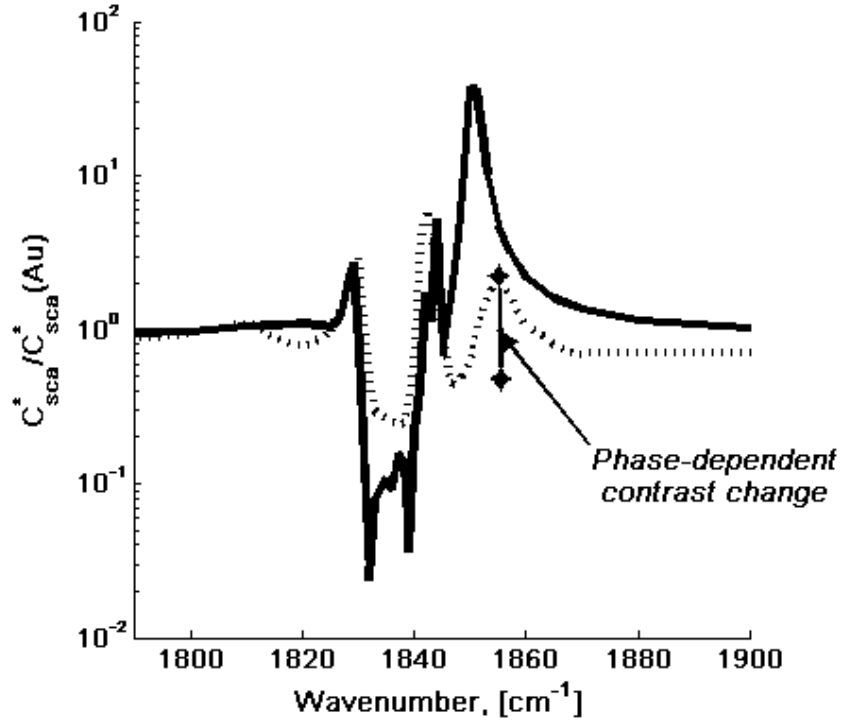
- ⇒ Enter the $\text{Fe}_2(\text{CO})_9$ (NEC-2 output data) Matlab file names for each value of ϵ_∞ .

⇒ Run the Matlab routine for simulation of the lock-in amplifier output.

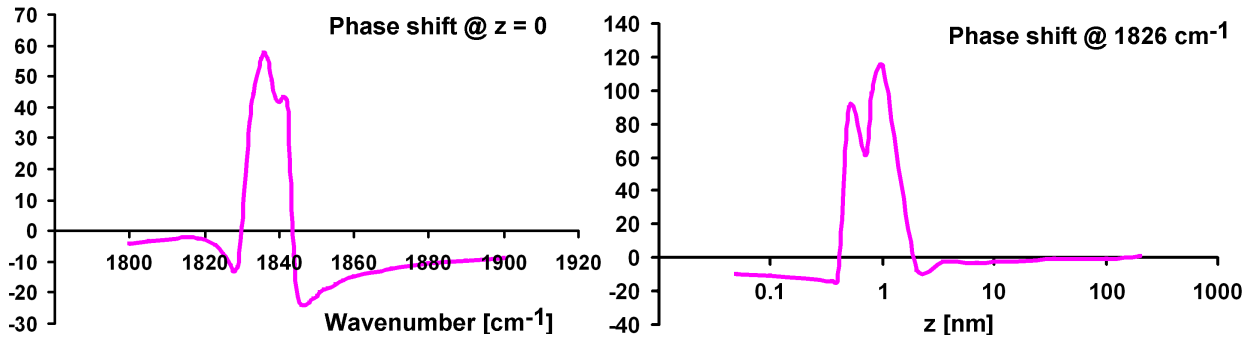
✚ Plots of the fitting curves against the experimental data as a function of frequency.

a) Two-point ($z = 0$ and the far field) estimate.

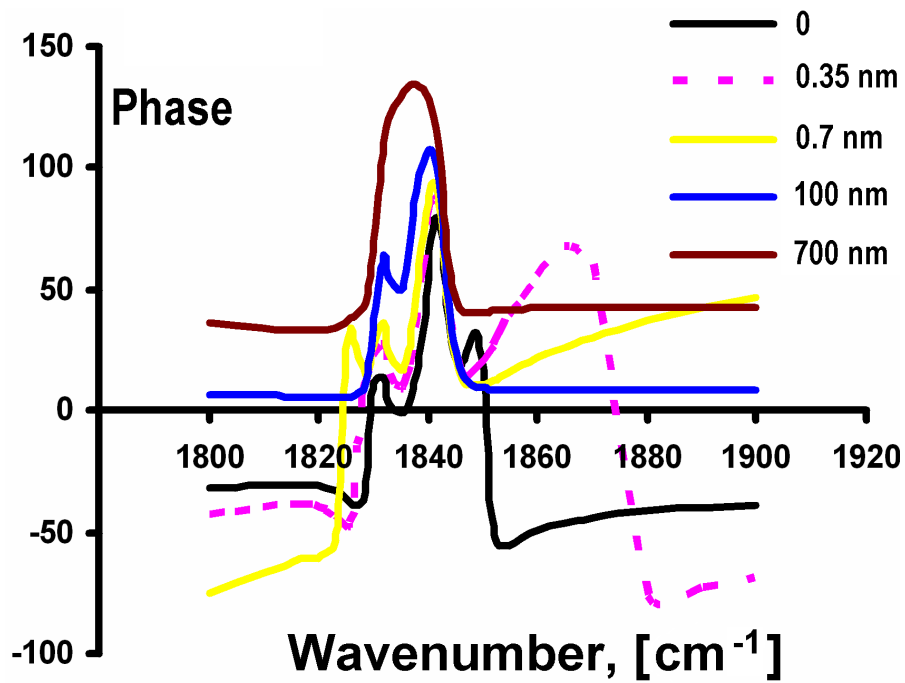




b) Phase shift versus gold surface (compare to Figure 51).

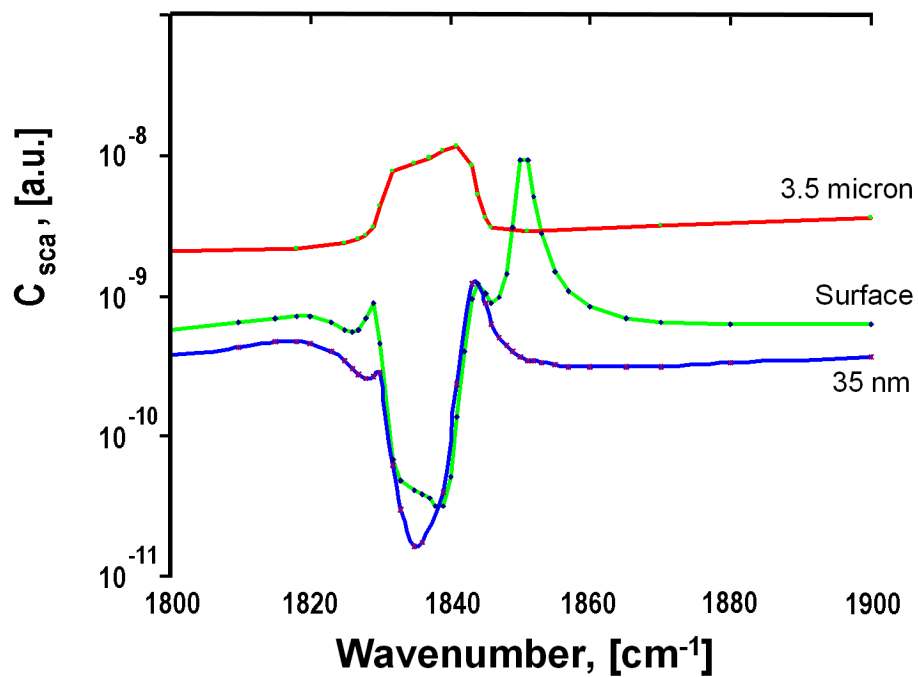


The wavelength dependence of the phase shift computed by the NEC-2 is similar to that predicted by the (static) coupled dipoles model, but the distance dependence anomaly at around $z \sim 1$ nm can be an artifact of the geometrical model. Similar to the amplitude of the back-scattered signal (Figure 59), the wavelength dependence of the phase also changes significantly between $z = 0$ and $z = 2$ nm. There are no significant changes in the amplitude or the phase between $z = 2$ nm and $z = 100$ nm. However, the changes resume at $z > 100$ nm, albeit at a much slower rate.

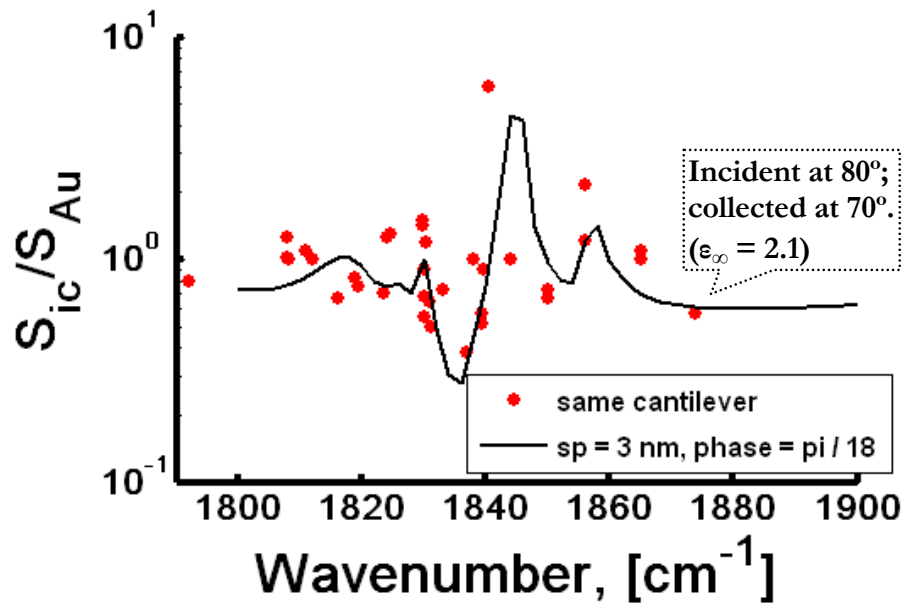


c) Integration over the path of the cantilever tip.

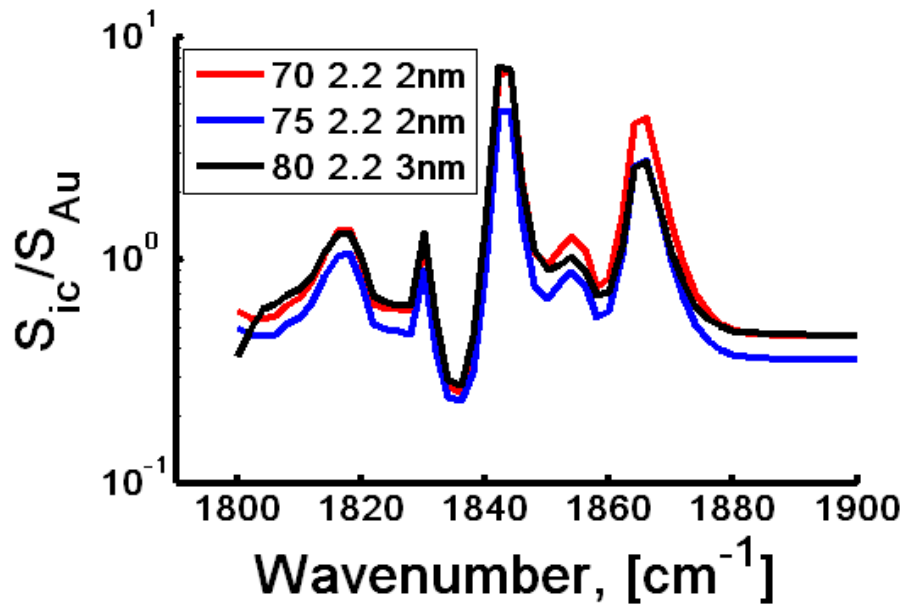
$\text{Fe}_2(\text{CO})_9$ scattering vs. tip-surface distance



Small changes to grid have some small effect on the fitting lines (compare to plots in Chapter 10), which indicates that finer grid could improve the accuracy of the fit.



The spectral pattern of the NEC-2 simulated near-field signal does not change significantly with the simultaneous changes in the angles of incidence and collection, within $\pm 5^\circ$.



However, changing just one of these angles does affect the signal. It means that more accurate modeling should be based on integration over the incidence and collection cones of the focused beam.

Possible beam misalignments can be accounted for by adjusting the weight coefficients of the plane wave segments; these coefficients should be corrected for the phase shifts as well.

